Europium Oxide as a Perfect Electron Spin Filter

by

Tiffany S. Santos

S.B., Materials Science and Engineering,
Massachusetts Institute of Technology, 2002

Submitted to the Department of Materials Science and Engineering
in partial fulfillment of the requirements for the degree of

Doctor of Philosophy of Materials Science and Engineering

at the

MASSACHUSETTS INSTITUTE OF TECHNOLOGY

June 2007

Author .....
Department of Materials Science and Engineering
May 17, 2007

Certified by .....
Dr. Jagadeesh Moodera
Senior Research Scientist and Group Leader
Thesis Supervisor

Certified by .....
Prof. Caroline Ross
Professor of Materials Science and Engineering
Thesis Supervisor

Accepted by .....
Prof. Samuel Allen
Chairman, Departmental Committee on Graduate Students

Europium Oxide as a Perfect Electron Spin Filter

by

Tiffany S. Santos

Submitted to the Department of Materials Science and Engineering
on May 17, 2007, in partial fulfillment of the
requirements for the degree of
Doctor of Philosophy of Materials Science and Engineering

Abstract

Essential to the emergence of spin-based electronics is a source of highly polarized electron spins. Conventional ferromagnets have at best a spin polarization P$\sim$50%. Europium monoxide is a novel material capable of generating a highly spin-polarized current when used as a tunnel barrier. EuO is both a Heisenberg ferromagnet (T_C=69 K) and a semiconductor. Exchange splitting of the conduction band creates different tunnel barrier heights for spin-up and spin-down electrons, thus filtering the spins during tunneling. High-quality EuO films at the monolayer level is necessary for efficient spin-filtering. Because non-ferromagnetic, insulating Eu_2O_3 forms more readily, growth of an ultra-thin, high-quality film is quite challenging, which restricted previous studies of EuO to bulk form. EuO films were grown by reactive thermal evaporation, and various thin film characterization techniques were employed to determine the structural, optical, and magnetic properties, even on the thickness scale needed for tunneling (<3 nm). The film properties closely matched those of bulk EuO, though the T_C for ultra-thin films was found to be reduced from bulk value, in agreement with theoretical prediction. Controlling the smoothness and chemical nature of the interfaces between EuO and metallic electrodes was found to be of critical importance, as proven by careful interfacial chemical and magnetic analysis at the monolayer level, using x-ray absorption spectroscopy, magnetic circular dichroism, and diffuse x-ray resonance scattering techniques. EuO was successfully prepared as the barrier in Al/2.5 nm EuO/Y tunnel junctions. By fitting the current-voltage characteristics of these junctions to tunneling theory, exchange splitting in an ultra-thin layer of EuO was quantitatively determined for the first time, and complete spin filtering yielded total spin polarization, P=100%. In an alternative approach, P was directly measured using the superconducting Al electrode as a spin detector. Spin-filtering in EuO barriers was also observed in magnetic tunnel junctions (MTJs), in which a ferromagnetic electrode was the spin detector. In Cu/EuO/Gd MTJs a tunnel magnetoresistance (TMR) of 280% was measured by changing the relative alignment of magnetization of EuO and Gd, which is the largest TMR measured using a spin-filter barrier. $Co/Al_2O_3/EuO/Y$ junctions, in which the Al_2O_3 barrier magnetically decoupled Co and EuO, also showed substantial TMR. Its matching band gap (1.1 eV) and compatibility with Si open up the novel possibility of using EuO to inject highly polarized spins into Si-based semiconductors.

Thesis Supervisor: Dr. Jagadeesh Moodera, Senior Research Scientist and Group Leader

Thesis Supervisor: Prof. Caroline Ross, Professor of Materials Science and Engineering

Acknowledgments

My heartfelt gratitude goes out to:

The thesis committee: Dr. Jagadeesh S. Moodera, Prof. Caroline Ross, Prof. Sam Allen and Prof. Francesco Stellacci, for their interest and guidance in this project, as well as in my academic and professional development.

A special thanks to Dr. Moodera, who has been my teacher on a daily basis, in the lab and in life. I cannot thank him enough for every opportunity and every challenge.

The scientists, postdocs and students that have been a part of the Moodera group during my time there, especially Prof. Markus Münzenberg, Prof. John Philip, Prof. Patrick LeClair, Dr. Andy Thomas, Joo Sang Lee, Dr. Taro Nagahama, Dr. I. Chaitanya Lekshmi, Dr. Guoxing Miao, Dr. Hyunja (Jenny) Shim, Dr. Marius Costache and Karthik Venkataraman. I have been lucky to work with and learn from these experts, and it truly has been a pleasure.

Dr. Ezana Negusse, an incredibly kind and hard-working collaborator and friend. There could not have been a more ideal and enjoyable partnership. Selam msakhi.

Prof. Yves Idzerda, for giving me the opportunity to work with Ezana, Joe and Marco.

Dr. Julie Borchers, Dr. Shannon Watson, Dr. Joe Dvorak, Dr. Marco Liberati and Dr. Biswarup Satpati, for applying their admirable expertise and energy toward this project.

My hosts who were very welcoming during my wonderful, productive visit to the CNRS/Thales lab: Prof. Agnès Barthélémy, Dr. Manuel Bibes and Prof. Pierre Seneor. A special thanks to Pierre for his assistance with all of the measurements and his thoughtful suggestions.

Prof. Don Heiman, for helping me set up optical experiments.

Dr. Geetha Berera, for teaching me how to be a materials scientist, and then teaching me how to teach others to be materials scientists.

Ana Ramos, a sharp collaborator and a good friend.

Dr. Bob O'Handley, for helpful discussions about magnetism and career options.

My father, Dr. Ted Santos (M.D.), who has given me the opportunity to pursue the best education at MIT, and has been loving and supportive the entire way. He has shown me to have strength through hardship and success through hard work. My work ethic stems from his example.

My mother, Jettie Sue Sweat, for her caring support and encouragement.

Alec Robertson, who has helped me maintain perspective and a work-life balance, which is quite rare at MIT.

Contents

List of Figures

Chapter 1

Introduction to Spin-Filter Tunneling and EuO

1.1 The Quest for Highly Spin-polarized Materials

The rise of spin-based devices is introducing non-volatility, reduced power consumption, faster data processing speed, additional functionalities and the potential for higher integration densities, compared to conventional, charge-based electronic devices. These spin-electronic (or spintronic) devices utilize not only the electron charge, but also the other inherent property of the electron, its *spin*. Spintronic devices available now include giant magnetoresistive (GMR) spin-valve read heads and tunnel magnetoresistive (TMR) read heads in hard disk drives, magnetic field sensors, and magnetoresistive random access memory (MRAM). Intense research activity in this field aims to incorporate spins into existing semiconductor technology. These future devices will write information in the electron spin orientation, spin-up or spin-down. The information in the spin can then be carried by the electron as it is transported through the device, and then read at an output terminal. The spin orientation survives over long distances in semiconductors—over 100 microns in GaAs [1]. This capability is attractive for making devices such as spin field-effect transistors (spin-FET), spin light emitting diodes (spin-LED), and ultimately a quantum computer, where a single electron spin would encode one bit of information. For a review of the field, see Refs. 2–4.

In order for spin to be utilized in semiconductor device technology, the following criteria are essential and present the foremost challenges: 1) generation and efficient injection of spin-polarized electrons into a semiconductor, 2) coherent transport of spins through the semiconductor, and finally 3) detection of the spin. The most successful way thus far of

injecting a highly spin-polarized current of electrons into a semiconductor is by illuminating the semiconductor with circularly-polarized photons, which have a spin that is imparted to the electrons via optical selection rules. Reading the spin by detecting the degree of circular polarization of light emitted from a LED structure in the device has also been successful. However, complete *electrical* spin-injection and detection, rather than by optical means, will make the most practical spintronic devices. Much about the mechanisms that cause spin relaxation, or loss of the spin information, in metals and semiconductors and their temperature dependences are known [4, 5]. A major obstacle on this front is engineering defect free materials in device structures with nanoscale dimensions, the length scale of coherent spin transport, in order to minimize the effects of spin-decoherence mechanisms.

This thesis focuses on the first criterion named above—generation and efficient injection of a highly spin-polarized current. The common approach to electrical spin injection is to use a ferromagnet (FM) or a ferromagnetic semiconductor as the source of spin polarized carriers for injection. The spin polarization of carriers from such materials originates from their unequal spin density of states. The problem with this approach is the conductivity mismatch encountered by the carriers at the interface between the FM and the semiconductor [6]. In the case of a FM/semiconductor contact, the conductivity mismatch is due to the very large spin-dependent conductivity in the FM (σ_{FM}) and the very small spin-independent conductivity in the semiconductor (σ_{SC}), such that the spin-injection coefficient $\propto \sigma_{\mathrm{SC}}/\sigma_{\mathrm{FM}} \ll 1$. The most promising solution to this mismatch problem is to tunnel through a thin barrier ($\sim$2 nm) sandwiched between the FM and the semiconductor [7, 8]. Even with carrier injection via tunneling, the strategy for high spin injection efficiency calls for a source of electrons that is highly spin-polarized. Conventional FMs show at best a spin-polarization (P) of $\sim$50%, for example $\mathrm{P_{Co}}$=45%, $\mathrm{P_{Fe}}$=44%, and $\mathrm{P_{CoFe}}$=51% [9], whereas it would be ideal to have an efficient spin injector with P=100%. One must turn to novel materials to find a potential candidate to fulfill this requirement. This thesis explores the potential of one such material, europium monoxide, that can efficiently filter electron spins to generate a highly polarized current of electrons for injection via tunneling.

1.2 A Brief Background of Spin-Polarized Tunneling

Spin-polarized tunneling is a rich field that has been active for nearly 40 years, resulting in tremendous progress to the understanding of fundamental physics and materials science, particularly on the following broad topics: band properties of superconductors and FMs,

interfacial density of states, surfaces, interfaces and proximity effects [10]. This brief section gives only the highlights that provide the foundation for this thesis work and put into perspective the contribution of this thesis work to the field.

Electron tunneling through a potential barrier is a quantum-mechanical phenomenon. When two metal electrodes are separated by a thin, insulating layer, there is a finite probability T(E) that an electron with energy E in one electrode will appear in an available state in the other electrode. The electron *tunnels* through the insulating layer, in which there are no states available. Using the Wentzel-Kramers-Brillouin (WKB) approximation, the tunneling probability is expressed as the following:

$$T(E) \approx T_0 \exp\left(-2d\sqrt{\frac{2m}{\hbar^2}(\Phi - E)}\right), \tag{1.1}$$

and the tunnel current density is

$$J = \frac{4\pi e}{\hbar} N_1(E)\, N_2(E - eV)\, T(E)\, [f(E) - f(E - eV)], \tag{1.2}$$

where d is the thickness of the barrier, m is the effective mass of the electron, Φ is the potential barrier, $N_{1,2}$ are the density of states (DOS) of the electrodes, $f(E)$ is the Fermi distribution function, and V is the voltage [11, 12]. Thus the tunnel current depends on the DOS of the electrodes and depends exponentially on the barrier height and barrier thickness, as will be discussed later.

In 1960 Ivar Giaever performed pioneering experiments showing that the tunnel current, between a metal and a superconductor (SC) through an Al_2O_3 barrier, is proportional to the DOS of the SC, which was a remarkable verification of Bardeen-Cooper-Schrieffer (BCS) theory [13, 14]. Later, Meservey and Tedrow *et al.* observed Zeeman splitting of the quasiparticle DOS of an Al superconducting thin film in a magnetic field, revealing the spin-up and spin-down DOS. Meservey and Tedrow proceeded to use the spin-split DOS of the Al superconductor as a spin detector for the the tunnel current from a ferromagnetic nickel electrode, demonstrating *spin-polarized* tunneling for the first time [15]. This experiment showed that spin is conserved in the tunneling process—a major, fundamental result. Meservey and Tedrow and colleagues extensively used this technique (referred to as the Meservey-Tedrow technique) to measure the tunneling spin polarization for the $3d$ FMs, their alloys and rare earths [10, 16, 17].

Building upon the work of Meservey and Tedrow, a Ph.D. student in L'Université de Rennes at the time, Michel Jullière, introduced a model for tunneling between two FMs in a FM/barrier/FM magnetic tunnel junction (MTJ) [18]. He related the change in junction

resistance, between parallel R_P and antiparallel R_{AP} alignment of the magnetizations of the two FMs, to the polarization of the two FMs ($P_{1,2}$), giving:

$$\frac{\Delta R}{R} = \frac{R_{AP} - R_P}{R_{AP}} = \frac{2P_1P_2}{1 + P_1P_2}. \tag{1.3}$$

Jullière also made the first reported magnetoresistance measurement in a Fe/a-Ge/Co junction, obtaining ~14% at 4.2 K [18].

Twenty years later, Moodera *et al.* [19] and Miyazaki *et al.* [20] independently showed significant tunnel magnetoresistance (TMR) in FM/Al_2O_3/FM junctions at room temperature. Because two clear resistance states (either R_P or R_{AP}) could be retained at zero magnetic field, corresponding to "0" and "1" bits, this discovery had great application potential and sparked tremendous activity in the field of spin-polarized tunneling that is still flourishing today. MTJs are now replacing giant magnetoresistance (GMR) spin valves in the read heads of hard disk drives. Another application made commercially available in 2006 is a non-volatile memory device, called magnetoresistive random access memory (MRAM), that employs an array of MTJs with Al_2O_3 barriers. The highest TMR value obtained for Al_2O_3 barriers at room temperature is ~70% [21]. In 2004 Yuasa *et al.* [22] and Parkin *et al.* [23] independently measured high TMR at room-temperature in lattice-matched Fe/MgO/Fe MTJs. High TMR in epitaxial Fe/MgO/Fe was predicted theoretically by Bulter *et al.* [24] and Mathon *et al.* [25] in 2001 and arises from the band symmetry of Fe and MgO, resulting in a much slower decay for majority states in the barrier than for minority states. For a review of MgO tunnel barriers, see Ref. 26. This phenomenon is sometimes referred to as "spin-filtering," which is different from the spin filter concept in this thesis. The highest TMR value reported for MTJs with MgO barriers continues to soar to new heights and is currently > 470% at room temperature and > 800% at 5 K [27].

Spin-polarized tunneling is an extremely interface-sensitive phenomenon, in which transport properties depend primarily on the density of states at the interface between the electrode and barrier [10]. For example, the tunneling spin polarization of the electrode is the polarization at the Fermi level at the electrode/barrier interface. Moodera *et al.* [28] showed that P reduced rapidly as just two monolayers of non-magnetic Au was inserted at the Al_2O_3/Fe interface in Al/Al_2O_3/Au/Fe junctions. As for MTJs, LeClair *et al.* [29, 30] observed an exponential decrease of TMR when a monolayer of Cu or Cr was inserted at the interface.

Spin-polarized tunneling is just as sensitive to defects in the barrier as to the interface. In practice, the tunnel barrier is only a few monolayers thick, sandwiched between the electrodes. On that scale, defects such as interfacial roughness, intermixing, non-stoichiometry

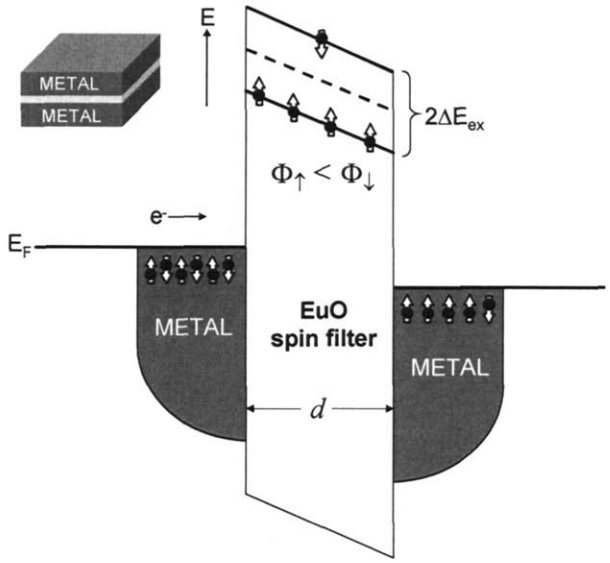

Figure 1-1: Schematic of the spin-filter effect. Electrons with randomly oriented spins tunnel from the nonmagnetic metal through the EuO spin-filter barrier. The ferromagnetic EuO conduction band is split into two spin-dependent levels, creating a higher barrier height for spin-down electrons and lower barrier height for spin-up electrons. Hence, the tunneling probability for spin-up electrons is much greater than for spin-down electrons.

or structural defects, are unavoidable. Such defects create states in the barrier, and tunnel junction conductance is a sum of all the contributions of these extra channels, giving a tunnel barrier height that could be quite different from that expected for a clean system. Importantly, these defects could scatter the spins, resulting in a loss of effective polarization, as they provide means for conduction through the barrier other than tunneling [31]. Meservey *et al.* [32, 33] showed very low barrier heights (few tens of meV, compared to ~2.0–2.5 eV for Al_2O_3) and complete loss of polarization for MTJs with semiconducting amorphous Si and Ge barriers, in which dangling bonds gave rise to defect states. As in all spin-polarized tunneling studies, defects play an important role in this investigation of EuO tunnel barriers, as well as in semiconducting organic barriers discussed in Appendix A.

1.3 Filtering Spins

Spin polarization of the tunnel current can be measured in a tunnel junction of the following structure: SC/insulator/FM, where Al is the SC and Al_2O_3 is the insulating tunnel barrier. Details of this measurement (Meservey-Tedrow technique) are given in the next chapter. P in this structure originates from the difference in the spin-up and spin-down electron density

of states at the Fermi level (E_F) in the FM:

$$P = \frac{N_{\uparrow,E_F} - N_{\downarrow,E_F}}{N_{\uparrow,E_F} + N_{\downarrow,E_F}}. \tag{1.4}$$

Instead of using a ferromagnetic metal as the source for spin-polarized electrons, as in the conventional Meservey-Tedrow method, this study utilizes a ferromagnetic *tunnel barrier* europium monoxide. EuO is a ferromagnetic semiconductor in which exchange splitting of the conduction band creates two different barrier heights for tunneling—a lower one for spin-up electrons ($\Phi_\uparrow$) and a higher one for spin-down electrons ($\Phi_\downarrow$), as shown in Figure 1-1. From Equation 1.2 for a given barrier thickness, the spin-up (spin-down) tunnel current density ($J_{\uparrow(\downarrow)}$) is exponentially dependent upon the corresponding barrier height $\Phi_{\uparrow(\downarrow)}$:

$$J_{\uparrow(\downarrow)} \propto \exp(-\sqrt{\Phi_{\uparrow(\downarrow)}}\, d), \tag{1.5}$$

Therefore, with even a modest difference in barrier heights, the tunneling probability for spin-up electrons is much greater than for spin-down electrons, resulting in spin polarization of the tunnel current:

$$P = \frac{J_\uparrow - J_\downarrow}{J_\uparrow + J_\downarrow} \tag{1.6}$$

However, the amount of exchange splitting ($2\Delta E_{ex}$=0.54 eV in bulk EuO) is far from modest. With this large exchange splitting, EuO essentially filters out completely the spin-down electrons, allowing only the spin-up electrons to tunnel. P could theoretically reach 100%.

The first demonstration of spin-filter tunneling was by Esaki *et al.* [34], using EuS and EuSe films, between 20 and 60 nm thick, sandwiched between either Al or Au electrodes. With this structure they observed tunneling across the potential barrier between the metal and the Eu chalcogenide spin filter. When measuring the temperature dependence of the I-V behavior of these junctions, a significant drop in voltage (measured with constant current) occurred below the T_C of both EuS and EuSe. This drop resulted from the lowering of the barrier height due to exchange splitting of the conduction band. P of the current was not quantified in this early tunneling experiment, as it was not realized that the tunnel current could be spin-polarized. Nevertheless, it showed evidence of what was later termed as spin-filter tunneling. A similar behavior of junction resistance for thin EuO barriers is described in Chapter 4. A few years after Esaki's work, Thompson *et al.* [35] also measured an increase in conductance at low temperatures due to conduction band splitting in a Schottky barrier structure made from a EuS single crystal and an indium metal contact. For a review of spin-filter tunneling, see Ref. 36.

High P resulting from the spin-filter effect was first quantified by Müller *et al.* [37], using the spin filter EuS. Field-emitted electrons from tungsten tips coated with EuS were found to have P=89±7% at low temperature. Similar work later confirmed that electrons tunnel from E_F of tungsten into the exchange-split EuS conduction band [38–40]. The high P of the emitted electrons resulted from the different potential barriers for spin-up and spin-down electrons at the W-EuS interface.

1.4 Advantage of Using EuO

The spin-filter effect has been studied extensively by Moodera *et al.* in thin tunnel barriers (1 nm to 4 nm thick) of EuS [41,42] and EuSe [43]. Ferromagnetic EuS barriers have shown P as high as 85%, even in zero applied magnetic field. On the other hand, EuSe is an *antiferromagnet* that becomes *ferromagnetic* in an applied magnetic field, when splitting of the conduction band occurs. Therefore, P for EuSe is field dependent: P=0 in zero field and increases with applied field, reaching nearly 100% at ~1 Tesla. EuS and EuSe have magnetic ordering temperatures of 16.6 K (Curie temperature) and 4.6 K (Néel temperature), respectively, and thus only filter spins at temperatures in the liquid helium temperature range. With a higher T_C=69.3 K and a greater $2\Delta E_{ex}$=0.54 eV (compared to 0.36 eV for EuS) [44], EuO holds promise to reach greater spin-filter efficiency at higher temperatures.

However, showing the spin-filter effect in EuO is a more challenging task than for EuS or EuSe. The difficulty lies in making a high quality, stoichiometric, ultra-thin EuO film. High quality ultra-thin films of EuS and EuSe are easily evaporated directly from a powder source of EuS and EuSe. While powder sources of the more stable non-magnetic Eu_2O_3 are readily available, EuO (the metastable oxide form) is not available, and therefore much more difficult to make as an ultra-thin film. Details of EuO film growth are given in the following chapter.

The europium chalcogenides are not the only candidates for spin-filter materials. Noticeable spin-filtering has been shown recently in the ferromagnetic perovskite $BiMnO_3$ [45], though only well below its T_C of 105 K. Ferrites have magnetic ordering temperatures well above room temperature and thus could potentially filter spins at room temperature. However, with their complex structure, the materials aspects are also a complicated issue in this case. Nevertheless, spin filtering has been observed in ferrimagnetic $NiFe_2O_4$ barriers [46], again only at low temperature. Very recently, a small, finite spin-filter efficiency has been observed for $CoFe_2O_4$ barriers at room temperature [47,48]. In these materials, the band structure that gives rise to the different spin-up and spin-down barrier heights is crucially dependent upon the atomic structure (specific chemical site occupancy) of these compounds.

Table 1.1: Spin Filter Materials

Material	Magnetic Behavior	T_C (K)	Moment (μ_B)	Structure a(nm)	E_g (eV)	$2\Delta E_{ex}$ (eV)	P(%)
EuO	FM	69.3	7.0	FCC, 0.514	1.12	0.54	29 [49]
EuS	FM	16.6	7.0	FCC, 0.596	1.65	0.36	86 [41,42]
EuSe	AFM	4.6	7.0	FCC, 0.619	1.80		100 [43]
$BiMnO_3$	FM	105	3.6	perovskite			22 [45]
$NiFe_2O_4$	ferri-M	850	2.0	spinel	1.2		22 [46]
$CoFe_2O_4$	ferri-M	796	3.0	spinel	0.57		[48]

Thus, chemically-ordered, epitaxial films are needed, which restricts the selection of electrode materials that can be used as well. Table 1.1 lists the known spin-filter tunnel barriers and their properties.

Though EuO cannot filter spins at room temperature, it provides a model for studies of spin-filter phenomena in other spin-filter materials. With its simple face-centered cubic (fcc), rocksalt crystal structure, negligible magnetic anisotropy, strong magnetic moment and large exchange splitting, near perfect spin filtering is shown for polycrystalline EuO in this study. Furthermore, its chemical compatibility and matching band gap with silicon (1.1 eV) make EuO an excellent candidate material for spin-injection into silicon.

1.5 Brief Overview of Past Work on EuO

There was much research activity focused on single crystals of the europium chalcogenides during the 1960s and 1970s. For an extensive review of this early work, see Refs. 44, 50–52. EuO was particularly attractive because in addition to being an ideal Heisenberg FM with a high magnetic moment and simple crystal structure, EuO was also semiconducting with interesting optical and electrical properties. One of the most remarkable electrical properties of EuO is the colossal magnetoresistance effect in single crystals of Eu-rich EuO, first discovered by Oliver *et al.* [53–55] during his Sc.D. thesis work in MIT. When cooled below T_C, the conductivity sharply rose by a remarkle 13 orders of magnitude [56], displaying an insulator-to-metal transition that is not present for stoichiometric EuO. Torrance *et al.* put forth the bound magnetic polaron model to explain this phenomenon, in which the two donor electrons are bound to the deep donor levels of an oxygen vacancy for $T<T_C$ and then released into the conduction band for $T>T_C$.

Another interesting effect was the increase in T_C by doping with rare earth metals Gd, La, and Ho [57–59]. These dopants are substitutional, replacing the Eu^{2+} ion with a trivalent ion, thus creating free electrons. T_C as high as ~160 K was found in a recent study of 4%

Gd-doped EuO thin films [60]. This increase in T_C has been attributed to an additional exchange interaction by the impurity electrons that stay in the vicinity of the donor and magnetically polarize neighboring Eu^{2+} spins [61]. Though raising the T_C is desireable in some cases, it is not relevant in this thesis because stoichiometric, defect-free EuO is needed as an insulating tunnel barrier. Furthermore, an extensive study by Schoenes and Wachter [62] on Gd-doped EuO showed that even though the T_C increased with doping, the amount of exchange splitting of the conduction band, $2\Delta E_{ex}$, was actually reduced. For example, for Gd-doped EuO with a free carrier concentration of $6x10^{20}$ cm^{-3} and T_C=115 K, $2\Delta E_{ex}$ dropped to 0.25 eV, less than half the bulk value.

Though the properties of EuO in bulk form are well studied, relatively little work has been done on thin films due to their instability. The most recent works include characterization of the conduction band edge for a 20 nm film using spin-resolved x-ray absorption spectroscopy, concluding that the exchange splitting is ~0.6 eV (measured with a resolution of 0.1 eV) and that doped charge carriers are nearly 100% spin polarized [63,64]. Another recent study demonstrated epitaxial growth of (001) EuO films, >65 nm thick, onto (001) silicon with a SrO buffer layer [65]. Growth and characterization of ultra-thin films were previously unknown until this thesis work.

1.6 Electronic Structure of Bulk EuO

The electronic structure and the magnitude of exchange splitting of the conduction band were first determined in optical studies by Wachter *et al.* [44,66,67]. The conduction band is formed by the $5d$ states at the lower edge and $6s$ states at higher energy (Figure 1-2, and the highest occupied energy levels of the valence band contain the p^6 states of oxygen. The energy gap between the conduction band and the valence band is 4.3 eV. The $4f$ states are located within this energy gap, and the optical band gap, $E_{g,opt}$=1.1 eV, is defined as the energy gap between these localized $4f$ states and the conduction band. The optical band gap is clearly observed in the absorption spectra for bulk crystalline EuO, shown in Figure 1-2, along with the absorption spectra of EuS and EuSe. The amount of exchange splitting of the conduction band was quantified by the red shift of the absorption edge (shift of the $5dt_{2g}$ band to lower energy) when cooled below the T_C [66]. The amount of the red shift corresponded to half of the exchange splitting = ΔE_{ex} = 0.27 eV; the spin-up states were lowered by ΔE_{ex} and the spin-down states were raised by ΔE_{ex} from the initial 1.1 eV optical band gap, as shown schematically in Figure 1-3. The crystal field splits the $5d$ density of states of the conduction band into two levels, the lower energy $5dt_{2g}$ states and

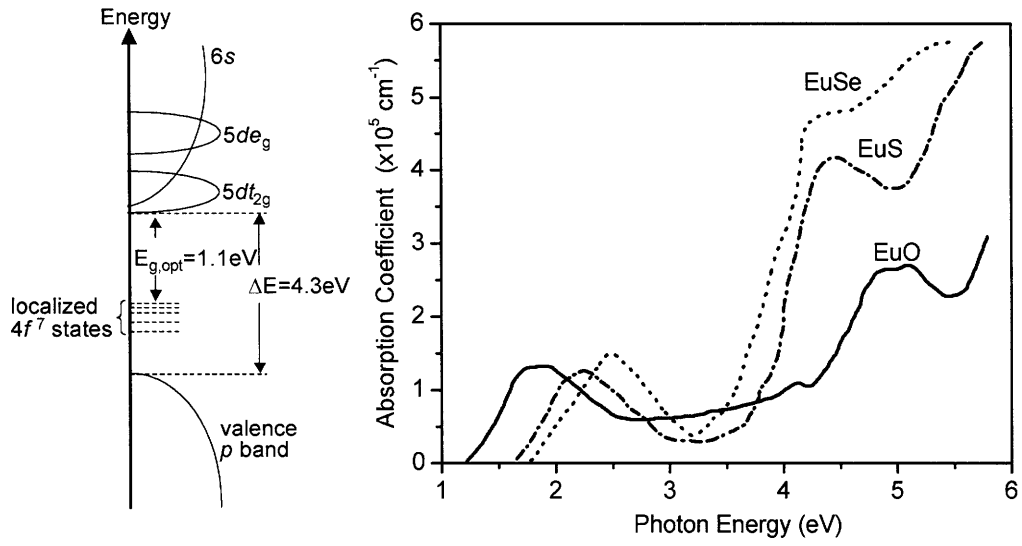

Figure 1-2: Left: Energy diagram of EuO [44, 50, 51]. Right: Absorption coefficient for bulk crystalline samples of the europium chalcogenides. Figure adapted from Ref. 67.

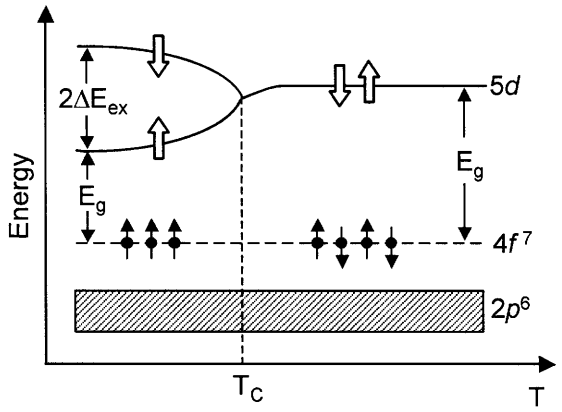

Figure 1-3: Schematic of the EuO band gap, as a function of temperature, showing exchange splitting of the conduction band edge for $T < T_C$. Figure adapted from Ref. 44.

the higher energy $5de_g$ states. The absorption peaks at ~2 eV and ~5 eV correspond to optical excitations from the $4f$ states into these levels, respectively.

1.7 Ferromagnetism in EuO

EuO is regarded as an ideal Heisenberg FM. The Heisenberg interaction is a direct exchange between neighboring spins resulting from the overlap of their atomic wavefunctions:

$$H = -2\sum J_{ij}\,\mathbf{S_i}\cdot\mathbf{S_j}, \tag{1.7}$$

where J_{ij} is the exchange constant (positive for ferromagnets and negative for antiferromagnets) and $\mathbf{S_{ij}}$ are the neighboring spins. EuO has a large saturation moment[1] $\mu_B g J = 7.0\,\mu_B$, which has been closely matched experimentally in bulk single-crystals and thin films, including the films in this study (see Chapter 3). Band structure calculations [70–72] predict a moment between 6.8 and 7 μ_B. The magnetic moment originates from the seven unpaired spins in the $4f$ levels of the Eu^{2+} ion. These f electrons are highly localized with negligible direct overlap of the $4f$ wavefunctions between neighboring Eu atoms in the EuO compound, which prevents any direct exchange interaction. Therefore, an indirect exchange mechanism must be at play.

The metallic ferromagnet gadolinium also has a large saturation moment=7 μ_B originating from the $4f^7$ levels. Ferromagnetism arises in this case from an indirect exchange, called Rudderman-Kittel-Kasuya-Yosida (RKKY) interaction, between the localized f electrons and the $5d$ and $6s$ conduction electrons. However, because EuO is a semiconductor, there are no carriers to mediate the ferromagnetic exchange between neighboring Eu^{2+} ions, yet EuO is strongly ferromagnetic. For this reason the microscopic mechanism that gives rise to the ferromagnetic behavior has not been well understood. In fact, the existence of a ferromagnetic insulator was disputed until the discovery of $CrBr_3$ in 1960 [73] and EuO one year later [74]. Shown in Figure 1-4 are the atomic wavefunctions for Eu^{2+}, O^{2-} and S^{2-} in the EuO and EuS compounds [75]. There is negligible overlap of the $4f$ wavefunctions of neighboring Eu^{2-} ions in EuO and EuS, but there is enough overlap of the $5d$ wavefunctions, which form the conduction band.

Goodenough [76] and Kasuya [75] proposed a model to explain the ferromagnetic interaction in these compounds, wherein an indirect exchange mechanism with the overlapping $5d$ states mediates the ferromagnetism. In this mechanism the cation wavefunction plays the important role, and the p wavefunctions of the anion are unimportant. According to this model, a $4f$ electron is excited to the $5dt_{2g}$ conduction band, where it undergoes a $d-f$

[1] EuO has an effective (paramagnetic) moment $\mu_B g\sqrt{J(J+1)} = 7.9\,\mu_B$, which is the *magnitude* of the moment, whereas the saturation moment $\mu_B g J$ reached by a FM is the maximum value of the *projection* of the moment on the applied field direction [68,69]. For the Eu^{2+} ion, Landé factor g=2, orbital angular momentum quantum number L=0 and spin angular momentum quantum number S=7/2, so that total angular momentum $J = L + S = 7/2$.

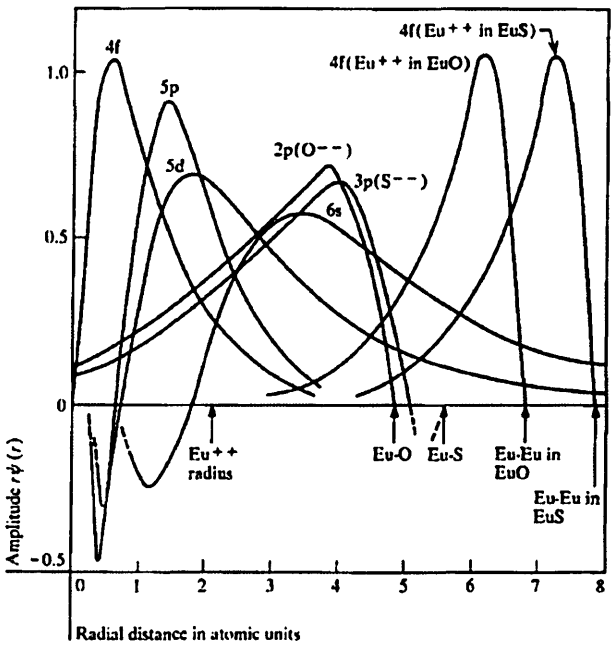

Figure 1-4: Atomic wavefunctions for Eu^{2+}, O^{2-} and S^{2-} in the EuO and EuS compounds, showing the overlap of the anion-cation and cation-cation functions. The arrows indicate the lattice distances between the neighboring atoms indicated. Figure from Ref. 75.

exchange at the nearest neighbor Eu site that polarizes the $4f$ spin, and then returns to its initial state. Thus, the $4f$ spins of neighboring Eu^{2+} ions experience an intra-atomic exchange interaction through this $d-f$ exchange. The ferromagnetic exchange constant J_1 can be expressed as:

$$J_1 = \frac{t^2 J_{fd}}{2S^2 U2}, \tag{1.8}$$

where J_{fd} is the intra-atomic exchange, U is the energy difference between the $4f^7$ and the $5dt_{2g}$ levels, which is equal to the optical band gap, and t is the transfer integral due to the inter-atomic overlap, which is proportional to the width of the $5dt_{2g}$ band. The value of J_1/k_B is $+0.606\pm0.008$ K, where k_B is Boltzmann constant.

The relation in 1.8 describes the trend observed across the EuX chalcogenides, where X is O, S, Se, and Te. J_1, and hence the ferromagnetic moment, is strongest in EuO, which has the smallest band gap (thus smallest U) and largest $5dt_{2g}$ band width (thus largest t). There is also an antiferromagnetic exchange mechanism (J_2) at play in these compounds, in which the anion plays the important role, such as in Kramers-Anderson superexchange. J_2 is actually positive for EuO ($= +0.119\pm0.015$ K), but becomes more negative across the chalcogenides, so that EuSe and EuTe are antiferromagnetic.

1.7.1 Magnetism in Ultra-thin EuO: Theory

Schiller *et al.* [77, 78] calculated the electronic structure of a single-crystal EuO(100) film, down to a single monolayer, as a function of temperature and thickness. Their study was performed using a combination of the ferromagnetic Kondo-lattice model and first principles band structure calculations. They found that the T_C of thin EuO is strongly thickness dependent, starting with T_C =15 K for a single monolayer (n=1) to the bulk value at $\sim n$=25. Figure 1-5 shows the layer-dependent magnetizations found from their calculation, giving the temperature dependence of the magnetization for the surface layer and center layers as the number of monolayers n is varied. The magnetization of the center layer follows the familiar shape of a ferromagnetic Brillouin function, whereas the shape of the magnetization curve for the surface layer is suppressed. This can be qualitatively explained by the lower coordination number of the surface atoms (=8 for this fcc structure) compared to that of the atoms in the center of the film stack (=12 for bulk). The inset of Figure 1-5 shows the reduction of T_C with n.

The T_C for a FM is derived from molecular field theory [69], which is based on the exchange interaction between each nearest-neighbor pair, $J_{ij}\mathbf{S_i} \cdot \mathbf{S_j}$ (see Equation 1.7). Thus, as thickness decreases such that surface atoms comprise a large fraction of the film, the T_C reduces due to the fewer number of nearest-neighbor interactions of the surface atoms. Because EuO films at the monolayer level were successfully made for the first time in this study, this thesis work gives the first experimental confirmation of Schiller *et al.*'s calculation, showing a reduction in T_C with thickness, described in Chapter 3. If the T_C is reduced for ultra-thin EuO, is the exchange splitting $2\Delta E_{ex}$ also reduced from the bulk value? This question is addressed in a tunneling experiment described in Chapter 4.

1.8 Organization of this Thesis

The aim of this thesis work was to explore the spin-filtering properties and demonstrate high spin-filter efficiency in EuO tunnel barriers. Not only did this involve fabrication of tunneling devices and measurement of P, but also total characterization and control of the barrier layer down to the atomic level, even pushing the limits of several state of the art characterization techniques. In order to achieve this, first of all high-quality EuO films had to be prepared on the thickness scale of 2–4 nm needed for tunneling. Herein were the real materials science and engineering challenges of this thesis project that accompanied the physics-rich aspects of spin-polarized tunneling. This thesis describes in detail how ultra-thin films were successfully prepared and incorporated into tunnel junction structures

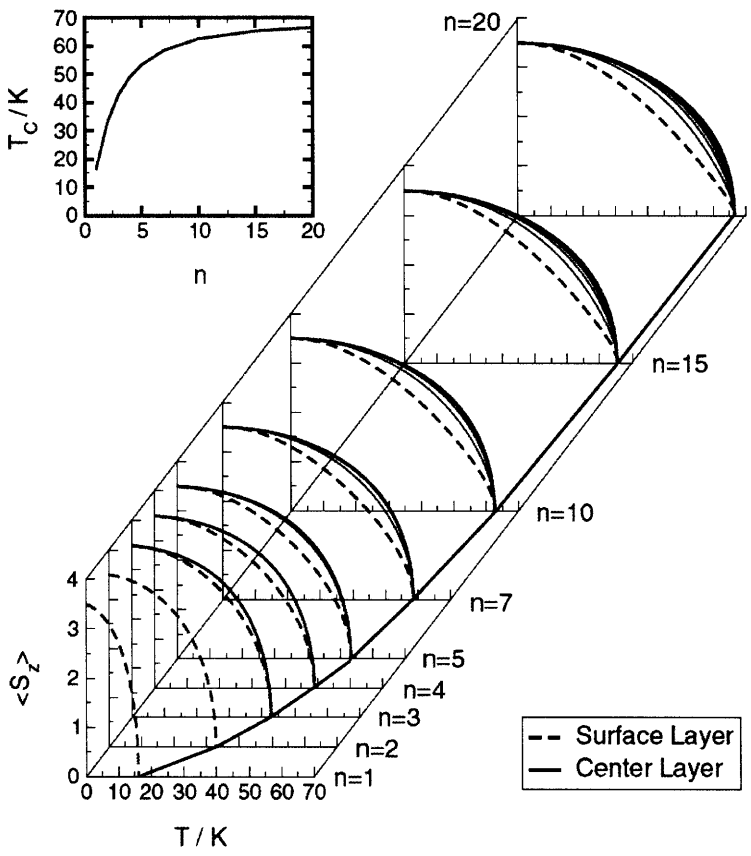

Figure 1-5: Layer-dependent and temperature-dependent magnetizations calculated for single crystal EuO(100) films, from Ref. 77. The inset shows T_C as a function of number of monolayers. The T_C for monolayer-level EuO is reduced from bulk value, down to ~15 K for a single monolayer (n=1).

that show a high degree of spin polarization. Film growth and experimental techniques are detailed in Chapter 2. The properties of the films and interfaces, shown in Chapter 3, were characterized at the monolayer level, using film characterization tools available at MIT and highly specialized techniques through collaborative, complementary efforts. The tunneling transport measurements were performed in the advisor's laboratory in the Francis Bitter Magnet Laboratory (FBML). Efficient spin filtering in EuO was successfully observed via two methods: by using a superconductor as the spin detector, described in Chapter 4, and by using a FM as the spin detector, described in Chapter 5. The significance of this work and future possibilities are discussed in Chapter 6. Finally, the results of a fruitful "side project" are given in Appendix A, in which spin-polarized tunneling through an organic semiconductor tunnel barrier was demonstrated for the first time.

Chapter 2

Experimental Methods

Before carrying out any tunneling experiments, the major challenge of the project had to be overcome. That is, a high-quality, ultra-thin film of EuO had to be prepared as a tunnel barrier. Various film characterization techniques were used to determine the quality of the film, including its structural, optical, magnetic and chemical properties. Once tunnel junctions with EuO barriers were successfully made, spin transport measurements could be performed. This chapter details the film deposition procedure, techniques used to characterize the films and interfaces, and the principles and experimental setup of the tunneling measurements.

2.1 Film Deposition

2.1.1 The Film Deposition Chamber

The EuO thin films and devices were fabricated at FBML using a custom-built, thin film vacuum deposition system. A schematic of the system, equipped with a diffusion pump, is shown in Figure 2-1. The base pressure of this high-vacuum chamber is $6x10^{-8}$ Torr. The system has five resistively heated, thermal evaporation sources, all mounted on a rotating platform, and a three-hearth, electron-beam evaporation source. Only one material can be evaporated at a time, and the material to be deposited is positioned directly beneath the substrate, at a distance of about 40 cm. An oscillating quartz crystal is used to monitor the film thickness *in situ*. The system has an interchangeable shadow mask system, which can hold up to six masks. The mask to be used is positioned directly beneath the substrate and then raised to be in contact with the substrate. The shadow masks are made out of beryllium-copper alloy sheets and are fabricated in the FBML by photolithography processes. The substrate is mounted onto a copper substrate holder, which can be cooled by a liquid-nitrogen flow, if needed.

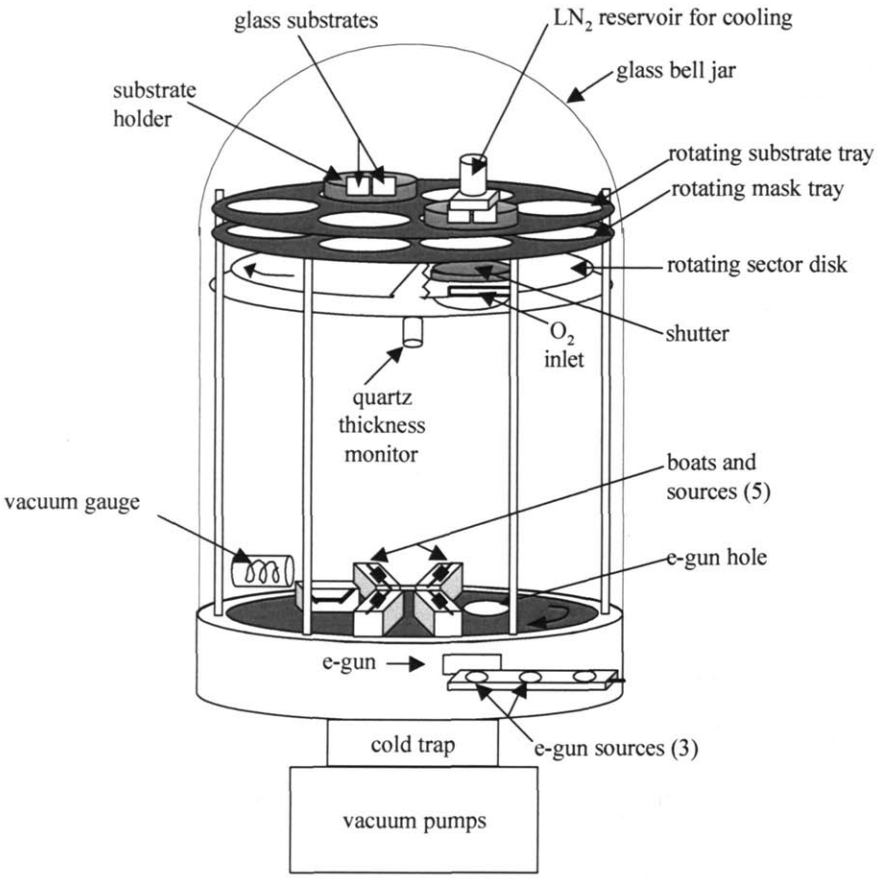

Figure 2-1: Schematic of the thin film evaporation chamber used for EuO deposition and tunnel junction fabrication. Five resistively heated sources and 3 electron-beam sources are placed at the bottom of the chamber. The substrate and shadow masks are located at the top. The substrate can be cooled by a liquid-nitrogen reservoir. An oscillating quartz crystal monitors the thickness.

2.1.2 Reactive Thermal Evaporation

EuO films were deposited by thermal reactive evaporation of an Eu metal source (99.99% pure) in the presence of a steady oxygen gas flow. The Eu metal was evaporated from a resistively heated tungsten boat. With a heat of formation ΔH_f= -1730 kJ/mol for Eu_2O_3 compared to ΔH_f= -608 kJ/mol for EuO, Eu readily oxidized to form the more stable compound Eu_2O_3 [79]. Therefore, careful control of the Eu evaporation rate and oxygen flow was crucial to forming the desired EuO stoichiometry. If the Eu evaporation rate was too high, then Eu-rich EuO was formed, which is not insulating so that tunneling was not

observed. If the Eu evaporation rate was too slow, then Eu_2O_3 was formed, which did not filter spins. The rate of film deposition was between 0.8 nm/minute and 1.0 nm/minute.

As can be seen in Figure 2-1, the thickness monitor, oxygen inlet and substrate are at different locations in the chamber. Because the thickness monitor is closer to Eu metal source than the substrate, and the oxygen inlet is closer to the substrate than the thickness monitor, more Eu-rich EuO is deposited on the thickness monitor, relative to the substrate, during the thermal reactive evaporation process. One must also consider that the thickness monitor operates at a higher temperature than the substrate (even though the monitor is water-cooled), which promotes the formation of Eu_2O_3. Because both Eu-rich EuO and Eu_2O_3 have a smaller density than stoichiometric EuO (density of Eu metal ρ_{Eu}=5.24 g/cm^3, $\rho_{Eu_2O_3}$=7.40 g/cm^3, and ρ_{EuO}=8.21 g/cm^3), this results in a thicker EuO film at the substrate compared to the nominal thickness detected by the monitor by up to 15%.

Various substrate materials were used. Films for property characterization were prepared on either Si(100) or Si/SiO_2 (thermally grown SiO_2 on Si, purchased from a vendor) wafer pieces. Films for optical transmission measurement were grown on either quartz or sapphire, since these materials have high transmission throughout the measured range of wavelengths. Tunnel junctions were grown on glass, as described below.

2.1.3 Tunnel Junction Fabrication

The tunnel junctions were prepared on Corning 7059 borosilicate glass substrates and patterned by shadow masks. The entire device structure was grown *in situ* by evaporation (either thermal or electron-beam). Aluminum superconducting electrodes, used in the Meservey-Tedrow technique of measuring P (described in Section 2.3.1), were typically ~4 nm thick and deposited onto liquid-nitrogen cooled substrates. After warming the substrate back to room temperature, the EuO barrier and top electrode were deposited, followed by a thick Al_2O_3 film over the entire junction structure for protection. In a given run, 72 junctions (Figure 2-2) were prepared *in situ*, with a junction area of 200x200 μm^2.

2.2 Film Characterization Techniques

This section briefly describes the techniques and equipment setup used to measure the film properties. The principles of these standard characterization techniques are not discussed in detail here, as they can be easily found in the reference literature.

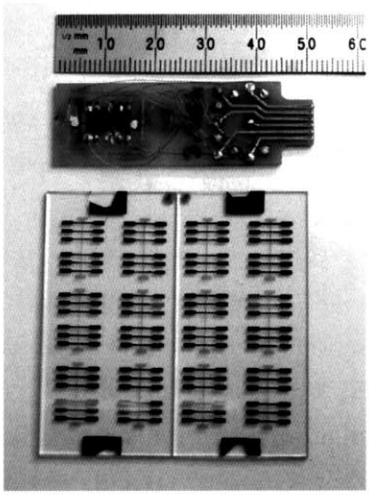

Figure 2-2: Photograph of the tunnel junctions, as prepared on glass substrates using shadow masks. A total of 72 junctions are prepared in a single run. The intersection of any vertical, metallic strip with any horizontal strip forms the tunnel junction, with an EuO barrier sandwiched between these two electrodes. At the top is a single set of six junctions with electrical connections to leads on a card, which can be plugged into a probe for measurement.

2.2.1 Structure

The crystal structure of the EuO films was determined by powder x-ray diffraction (XRD) [80]. The crystal structure of bulk EuO—face-centered cubic (rocksalt) with a lattice constant of 0.514 nm—was expected. A Rigaku powder diffractometer in glancing angle mode with a thin film attachment was used, located in the Center for Materials Science and Engineering (CMSE) in MIT. Thicker EuO films >10 nm were needed for XRD measurement, in order to get enough intensity for proper identification. In glancing angle mode, the angle of the incident x-ray beam (relative to the sample surface) is fixed at a small angle, which increases the x-ray path length through the EuO film and decreases the penetration through the substrate. Thus, the signal intensity from the substrate is minimized, while the EuO signal is increased. The XRD spectra were analyzed with Jade software, where a reference spectrum for EuO could be found. The EuO lattice and crystalline grains were studied using high-resolution transmission electron microscopy (TEM), in collaboration with Dr. Biswarup Satpati, located at the Institute of Physics, Bhubaneswar in India (and currently at the Paul Drude Institute for Solid State Electronics in Berlin, Germany).

2.2.2 Optical Transmission Measurements

Optical transmission T_L was measured using a Varian Cary UV-Vis-IR spectrophotometer, located in the CMSE. From the transmission spectra, the absorption coefficient α was calculated using the relation $T_L = \exp(-\alpha d)$, where d is film thickness. The α for the films was compared to α for bulk EuO (Figure 1-2).

2.2.3 SQUID Magnetometer

Magnetic behavior of the films were measured using a superconducting quantum interference device, known as a SQUID magnetometer, located in the CMSE. The SQUID measures magnetization of the sample as a function of temperature (4 K to 400 K range) and applied magnetic field (±70,000 Oe range), with a sensitivity down to 10^{-6} EMU (electromagnetic units). With such a large saturation moment, 7 μ_B per Eu^{2+} ion, an EuO film sample with area ~4 mm by 8 mm and thickness down to 1 nm could be measured by the SQUID. Because the SQUID measures M for the entire sample, including substrate and seed layers and capping layers, the linear M(H) behavior of the paramagnetic or diamagnetic layers was measured out to a few Tesla (1 Tesla = 10,000 Oe) and then subtrated from the measured M(H) in order to extract the ferromagnetic behavior of the EuO.

2.2.4 X-ray Absorption Spectroscopy and Magnetic Circular Dichroism

Further characterization of the magnetic properties as well as chemical analysis of the films was done by various x-ray techniques. X-ray Absorption Spectroscopy (XAS) and X-ray Resonant Scattering (XRS) measurements were conducted at beamline U4B at the National Synchrotron Light Source in Brookhaven National Laboratory (BNL) by Ezana Negusse and Dr. Joe Dvorak. X-ray Magnetic Circular Dichroism (XMCD) measurements were conducted at the soft x-ray undulator beamline 4.0.2 at the Advanced Light Source (ALS) at Lawrence Berkeley National Laboratory by Johnathon Holroyd, Dr. Marco Liberati and Dr. Elke Arenholz. All of these x-ray investigations were done in collaboration with Prof. Yves Idzerda's group of the Physics Department in Montana State University. The x-ray analysis was done by Ezana Negusse, as a major part of his Ph.D. thesis work [81].

These x-ray characterization techniques were ideal for this study because they are non-destructive, element-specific, and interface sensitive. Element specificity allowed analysis of the EuO, even though it was buried beneath various capping layers, by measuring at the Eu absorption edge. Because there is a finite energy separation between absorption peaks for

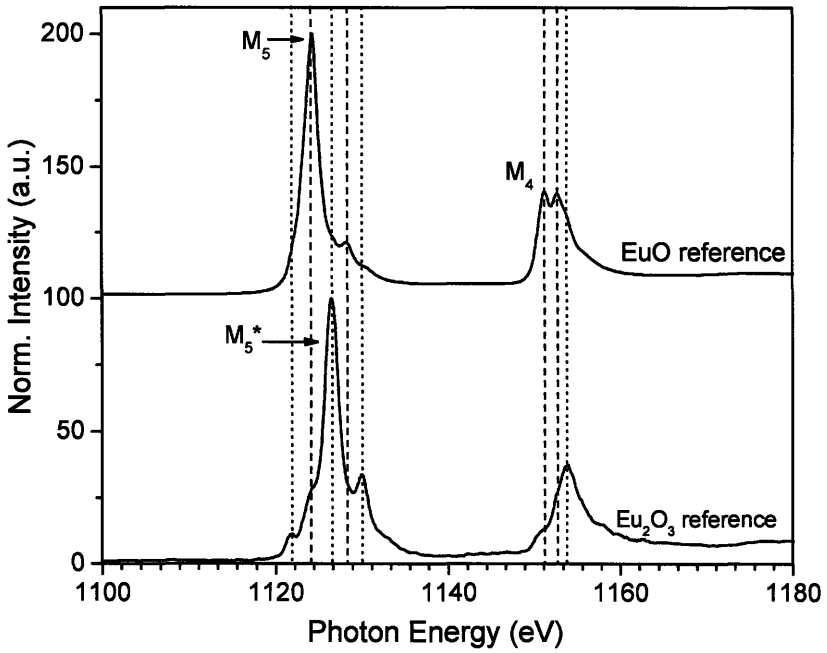

Figure 2-3: X-ray absorption spectroscopy for the reference EuO and Eu_2O_3 films. The M_5 peak and the doublet M_4 peaks are characteristic of EuO. The M_5* peak, at slightly higher energy than the M_5, and the single M_4 peak are characteristic of Eu_2O_3. The dashed vertical lines mark the features that are characteristic of EuO, and the dotted lines mark those of Eu_2O_3.

Eu^{2+} and Eu^{3+}, the fractional amounts of EuO and Eu_2O_3 in the films could be extracted by deconvolving the XAS spectra. Figure 2-3 shows the reference XAS spectra used for EuO and Eu_2O_3, both from film samples made at the FBML. These reference spectra were validated against the characteristic Eu^{2+} and Eu^{3+} XAS spectra at the $3d_{5/2}$ (M_5) and $3d_{3/2}$ (M_4) edges of europium spectra given in Ref. 82, and they each have <5% of the other oxide and <10% pure Eu metal. The analyses of the XAS spectra for all the films were done using these reference spectra. The M_5 and M_5* peaks are characteristic of EuO and Eu_2O_3, respectively, as detailed in Figure 2-3. In addition, by varying the incident angle of the x-ray beam to the sample surface, the penetration depth of the x-rays into the sample thickness was varied, giving chemical analysis as a function of film thickness. Thus, the location of any Eu_2O_3 present in the film, either uniformly throughout the bulk of the film or concentrated at the interface, was probed by collecting XAS spectra as a function of incident angle.

As described above, XAS analysis provides *chemical* information about the film. In order to obtain *magnetic* information, XMCD analysis is needed [83]. The XMCD signal is simply $(I^+-I^-)/(I^++I^-)$ x 100, where $I^+(I^-)$ is the XAS intensity for when the angular momentum (or spin) of the incident, circularly-polarized light is parallel(anti-parallel) to

the film magnetization. This provides magnetic information because the circularly-polarized light excites a different number of spin-up and spin-down electrons at the M_5 and M_4 edges, depending on the relative alignment of photon spin and sample magnetization.

In comparison to measuring the magnetic properties of the films using the SQUID magnetometer, the XMCD technique has the added advantage of giving chemical information as well as magnetic information. The SQUID magnetometer measures the magnetic moment from the entire sample, including substrate, seed layer and protection layer. For this reason, no ferromagnetic materials other than EuO can be present in the sample, to ensure that any ferromagnetic behavior clearly comes from the EuO, and preventing contamination is critical. However, in the XMCD technique, the magnetic properties can be examined for a particular layer in a multilayer sample, simply by collecting the XMCD only at the absorption edge of that particular element. Furthermore, XMCD can confirm that the ferromagnetism comes only from EuO, and that there is no contribution from Eu_2O_3, as expected since Eu_2O_3 is weakly paramagnetic.

The XRS technique was used to determine the perpendicular and in-plane roughness at a particular interface of these multilayer films [84], which involves making specular and off-specular (diffuse) resonant scattering measurements. Perpendicular roughness is the same as root-mean-square (RMS) roughness, and in-plane roughness is given as the lateral peak-to-peak correlation length between roughness peaks. Roughness at the interfaces in multilayer thin film devices is caused by chemical reactions and inter-diffusion between the layers, as well as the film deposition parameters and substrate surface preparation. Minimizing interfacial roughness is critical for optimum performance of tunnel junction devices for numerous reasons: roughness disrupts coherent spin transport during the tunneling process, causes coupling of the magnetic layers, affects the coercivity of the magnetic films, and can lead to an electrical short of the tunneling device. XRS is a useful and powerful technique because it is an element-specific, non-destructive method for quantifying the roughness of specific, buried interfaces in a device. Because the measurement setup at BNL did not have the capability to cool the samples below the T_C of EuO, magnetic roughness could be not studied by using the x-ray resonant magnetic scattering technique (XRMS). The XRS study of the EuO films is a main component of Ezana Negusse's thesis work. Refer to his thesis [81] for details of the XRS results, as they are not described in this thesis.

The measurements were done in total electron yield (TEY) mode [85] with a photon energy resolution of 0.4 eV. In TEY mode the number of electrons emitted from the sample surface (and hence the rate of absorption) is found by measuring the current from the sample to the ground. Thus, for the samples prepared for x-ray analysis, the total thickness of the capping layers above the EuO had to be kept less than $\sim$8 nm. At the energy of the M_5

and M_4 edges of Eu, the x-rays can penetrate deep into the sample, through the capping layer. However, in TEY mode the absorption intensity comes from the number of electrons that escape from the surface sample, and the probability of escape decays exponentially with depth into the film. For example, films prepared with a capping layer >12 nm thick did not yield any x-ray signal because the electrons could not escape through such a thick capping layer.

2.3 Tunneling Measurement

2.3.1 Superconducting Tunneling Spectroscopy

The spin polarization of the tunnel current through an EuO tunnel barrier was directly measured by using the Meservey-Tedrow technique developed in the FBML in 1970 [10, 15, 86]. In these measurements, P of the tunneling electrons was detected by a superconducting aluminum electrode. Essential to this technique is the dramatic increase of the orbital parallel critical field of superconducting Al films, from about 0.01 T for bulk Al to 5 T for the ~4 nm films used in this measurement, in addition to an increase in the superconducting transition temperature T_{SC}, from 1.18 K for bulk Al to ~2.6 K for a 4 nm film. Furthermore, conservation of spin in the tunneling process is key to the observation of spin polarization.

Figure 2-4 shows the quasiparticle (DOS) of the Al electrode, with the superconducting energy gap centered at the Fermi level. When a magnetic field is applied (H>0) parallel to the plane of the film as in Figure 2-4b, Zeeman splitting of the superconducting quasiparticle DOS occurs with magnitude $2\mu_B$H; the quasiparticle states with magnetic moments parallel to the magnetic field are lowered in energy by $-\mu_B$H, and those that are antiparallel are raised by $+\mu_B$H. Here, μ_B is the electron magnetic moment, or the Bohr magneton. Thus, in the presence of H, the DOS is spin-dependent, allowing the superconducting Al to act as the spin detector. This special property of the SC has led this technique to be extensively used for measuring P of the tunnel current from a FM through an insulating tunnel barrier, such as the 3*d* FMs and an Al_2O_3 or MgO barrier [16, 23]. Aluminum is the SC used for this measurement because it has low spin-orbit scattering, and thus long spin lifetime, and a high critical field ~5 T. Furthermore, ultra-thin films of Al can be easily and reproducibly prepared. Another advantage is that a clean, surface oxide acts as a good tunnel barrier.

The conductance (dI/dV) measurement for a SC/insulator/metal tunnel junction as a function of bias is shown in Figure 2-4c for H>0. The superconducting energy gap, where dI/dV→0, is centered at zero bias. The measured conductance is a superposition of the spin-up and spin-down conductance. For P=0, the number of spin-up electrons and spin-

down electrons in the tunnel current is equal, giving rise to equal spin-up and spin-down conductance and a symmetric dI/dV curve. However, when the 'metal' electrode is replaced by a ferromagnetic metal, so that P≠0, shown in Figure 2-4d for the example P=50%, the spin-up conductance is greater than the spin-down conductance, and the dI/dV curve is *asymmetric*. The four conductance peaks are labelled σ_{1-4}, and P is given by:

$$P \approx \frac{(\sigma_4 - \sigma_2) - (\sigma_1 - \sigma_3)}{(\sigma_4 - \sigma_2) + (\sigma_1 - \sigma_3)}. \tag{2.1}$$

.

An accurate determination of P from the conductance curve requires well-resolved conductance peaks. For this reason, the conductance measurement was performed at T=0.45 K, well below the critical temperature of the Al superconducting electrode (~2.6K). The sample was cooled to 0.45 K in a ^{3}He refrigerator located in the FBML. A schematic of the ^{3}He refrigerator and cryostat is shown in Figure 2-5. The sample was attached to a probe with electrical connections and placed inside the ^{3}He refrigerator, which was then evacuated of air and filled with ^{3}He gas. The refrigerator was centered in a superconducting solenoid with an axial field up to 8 T, operating in persistent mode. The cryostat comprised of an outer liquid-nitrogen jacket and an inner liquid ^{4}He bath surrounding the ^{3}He refrigerator. By reducing the vapor pressure above the ^{4}He bath, the temperature of the ^{4}He bath lowered to 1.4 K, and the ^{3}He gas condensed into a liquid in the sample space. When the ^{3}He bath was then pumped, the temperature lowered to 0.4–0.5 K, thus cooling the sample. The sample probe was equipped with a gear system with which the sample could be tilted, in order to precisely align the Al superconducting film parallel to the applied field, so that orbital screening current was minimal.

Dynamic conductance was a two terminal measurement, in which a small ac voltage (~20μV) was superimposed onto the dc bias voltage across the junction. The change in ac current through the junction was measured by detecting with a lock-in amplifier the ac voltage across a series resistor (R_S). The circuit for dI/dV measurement is shown in the inset of Figure 2-5.

Using a superconducting spin detector, with its spin-split DOS, is by far the most unambiguous method of measuring P of the tunnel current because of the long coherence length of SCs (~50 nm for ultra-thin Al films). A ferromagnetic spin detector can also be used to measure P, as in a MTJ where P of one FM is known, which has the advantage that the measurement can be performed at room temperature in a small-applied magnetic field. However, because of the very short coherence length of ferromagnetic metals (<1 nm), the

quality of the metal interface with the tunnel barrier must be well-controlled down to a monolayer, in order to obtain reproducible results.

2.3.2 Magnetoresistance Measurements

Measurements of tunnel magnetoresistance in MTJs with EuO barriers was also done in this study to observe spin filtering. Either a 2-terminal or 4-terminal configuration was used to measure resistance, by applying a fixed voltage and measuring current. A two-terminal measurement was used only when the junction resistance was much greater than the lead resistances. The samples were cooled in a cryostat equipped with a magnet for sweeping the field in the plane of the film.

Two different structures of MTJs were investigated. The first structure had the EuO barrier in direct contact with the ferromagnetic Gd electrode: Cr/Cu/EuO/Gd (films listed in the order deposited). This structure and the measurements are described in Section 5.1. These junctions were made in the FBML and taken to Unité Mixte de Physique CNRS/Thales in Palaiseau, France for TMR measurements. This study was done in collaboration with Prof. Pierre Seneor and Prof. Agnès Barthélémy at the host laboratory and Dr. Manuel Bibes at the Institut d'Electronique Fondamentale, CNRS, Université Paris-Sud. The host laboratory had an ideal measurement setup for measuring high resistance junctions (in the GΩ range, with current in the pA range) at low temperature, with minimal noise.

The second structure had the EuO barrier separated from the ferromagnetic Co electrode by an ultra-thin Al_2O_3 layer: CoO/Co/Al_2O_3/EuO/Y/Al. This structure and the measurements are described in Section 5.2. These junctions had a resistance of a few MΩs at most and were measured in the FBML.

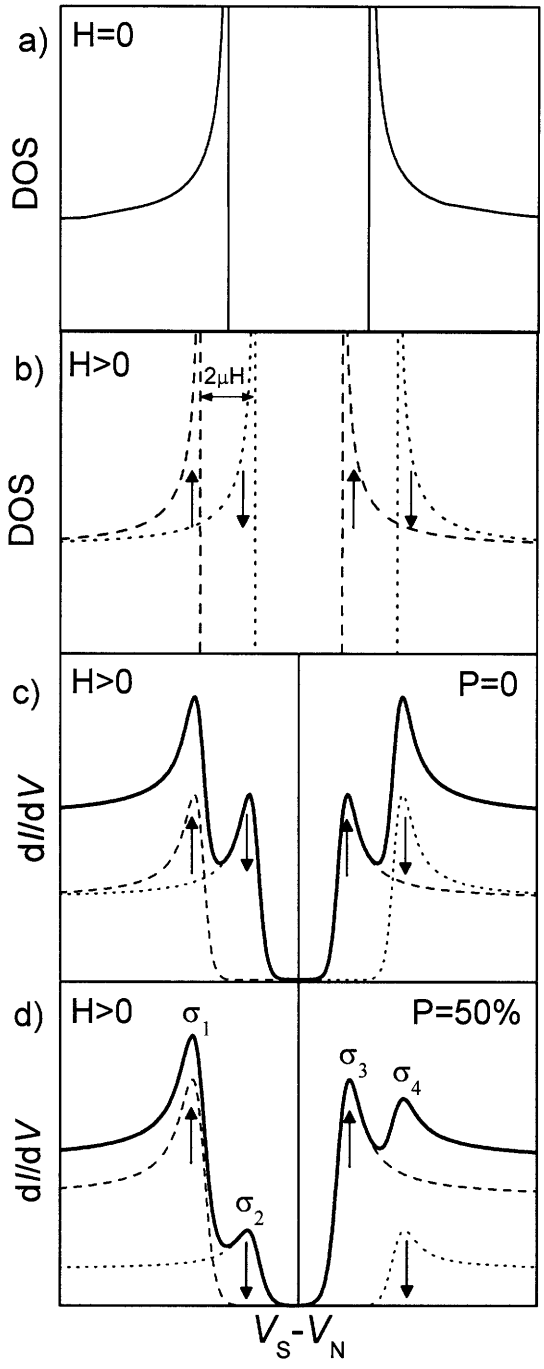

Figure 2-4: a) Superconducting Al quasiparticle DOS at T$\ll$T$_{SC}$ and zero applied magnetic field. b) Al quasiparticle DOS in applied field H. The magnitude of the Zeeman splitting is $2\mu_B$H. c) Tunnel conductance (dI/dV) of a junction (H>0) with zero spin polarization (non-magnetic counter-electrode). d) Conductance of a junction with P = 50%. P comes from the FM counterelectrode or due to spin-filtering.

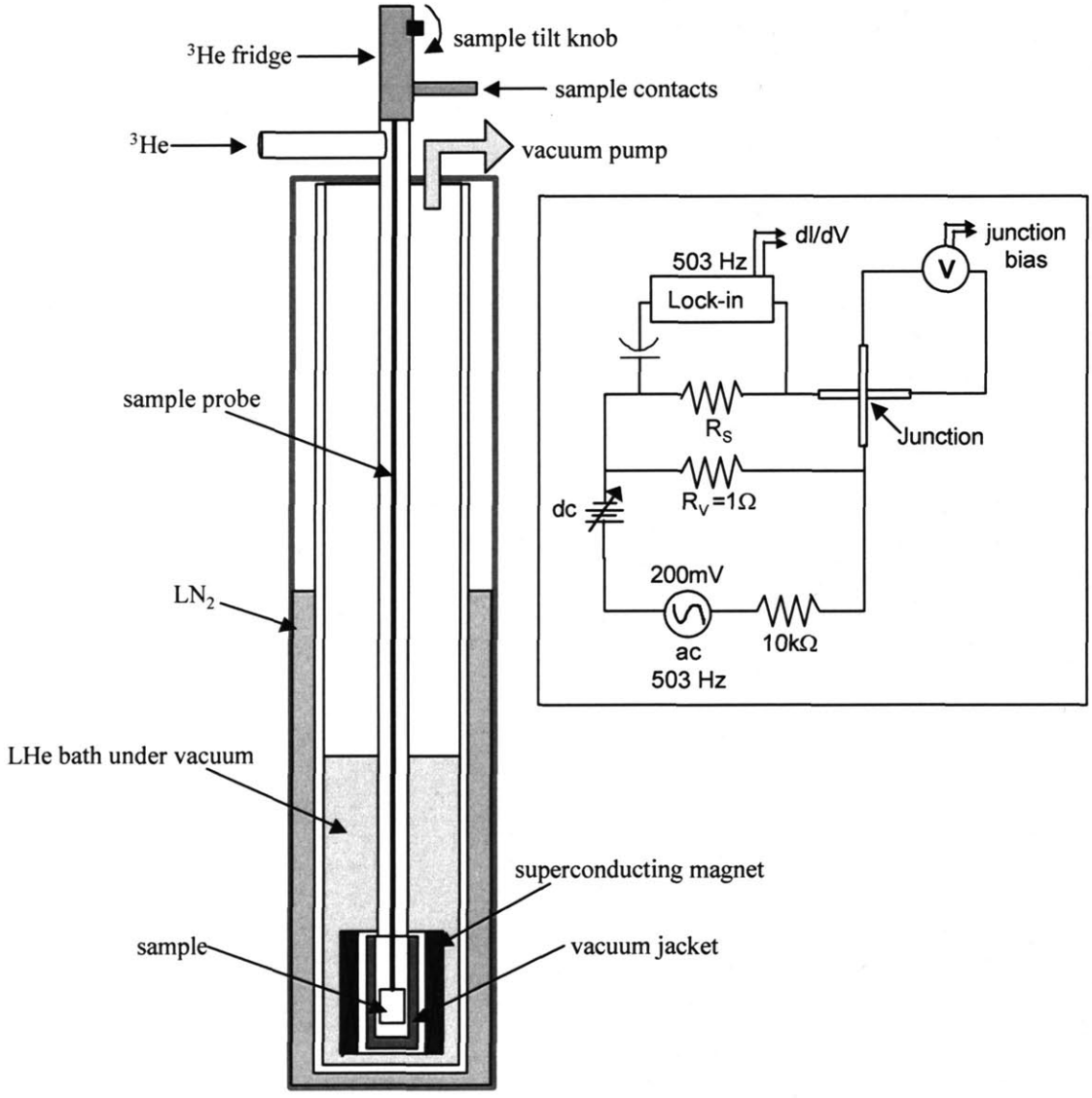

Figure 2-5: Custom-built ^{3}He refrigerator for cooling the sample to 0.45 K. Inset shows the electrical circuit used for measuring dynamic conductance dI/dV versus V for a tunnel junction. R_V acts as a voltage source for both the dc bias and the 20 μV ac bias. To reach higher bias, R_V can be increased to 10 Ω or 100 Ω, which gives a larger excitation voltage and signal.

Chapter 3

Properties of EuO Films at the Monolayer Level

In previous studies of EuO, only samples of EuO in bulk form had been used—either single-crystals or thick films (refer to Section 1.5). This chapter displays the properties of EuO thin films, ranging from bulk-like behavior for thicker films down to ultra-thin EuO just 1 nm thick, determined using the state-of-the-art characterization techniques described in the previous chapter. The interaction of EuO with various interface materials is discussed, emphasizing the importance of careful selection of interface materials on EuO film quality. Since this is the first time that EuO films <6 nm have been successfully prepared, this project allowed characterization of EuO on a new scale, requiring a solid understanding of thin film and surface magnetism and capabilities of the characterization techniques. The chapter concludes with a comparison of one of the first EuO films made in this study to one of the last, illustrating the drastic improvement in film quality accomplished during this project.

3.1 Structure

X-ray diffraction in glancing angle mode for a 15 nm EuO/15 nm Al_2O_3 film grown on Si (100) is shown in Figure 3-1, along with the XRD spectrum for a 15 nm Al_2O_3 film on Si (100) made simultaneously for reference. EuO has a fcc rocksalt crystal structure, shown in the inset of Figure 3-1, with a lattice constant a=0.514 nm. The (111), (200), and (220) peaks of EuO are clearly observed, matching those of the EuO powder reference obtained from the Jade analysis software. This XRD spectrum shows that the film is polycrystalline.

The polycrystalline structure is also seen in the high-resolution TEM image of a 3 nm EuO/2 nm Y/4 nm Al film grown on Si(100), shown in Figure 3-2. The surface of this Si

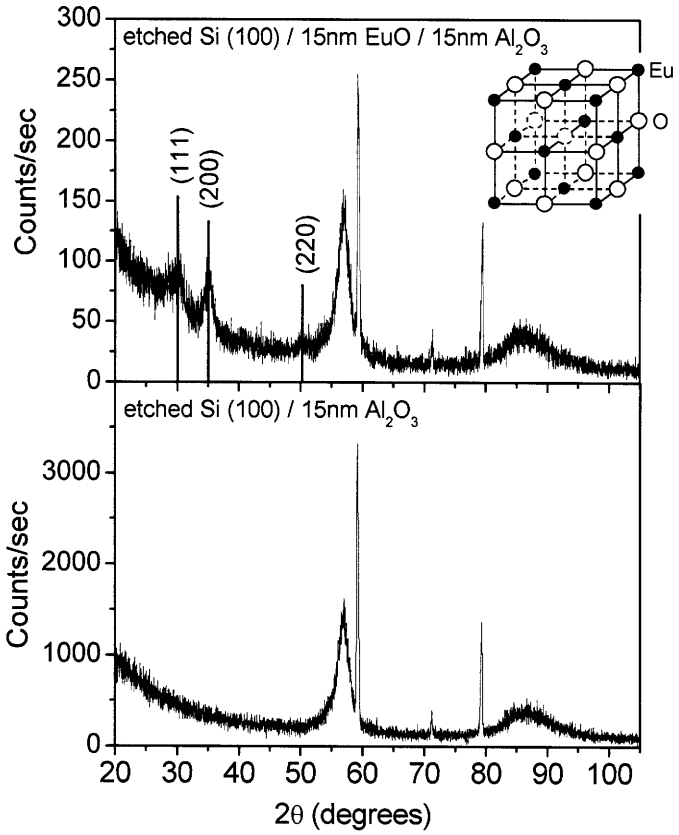

Figure 3-1: XRD spectra of 15 nm EuO/15 nm Al_2O_3 on a Si(100) substrate (top) along with a stardard of 15 nm Al_2O_3 on a Si(100) substrate (bottom), measured in glancing angle mode with θ=5°. XRD peaks for EuO are identified in the top spectrum. The inset is a schematic of a unit cell of the face-centered cubic, rocksalt crystal structure of EuO.

(100) substrate was prepared by a quick dip in dilute hydrofluoric acid (HF) to remove the native SiO_2 layer before immediately loading into the vacuum chamber. As seen in the image, the Si/EuO interface is not atomically smooth. This is likely due to silicon oxide formation in the base pressure of the deposition chamber, before film deposition. This silicon oxide then competes with EuO for oxygen. Nevertheless, EuO grown on Si consistently showed excellent magnetic and chemical properties, measured by SQUID magnetometer and XAS (described below). EuO grown directly on the native oxide of the Si substrate, without the HF cleaning prior to loading into the vacuum, showed significantly poorer properties, i.e. magnetic moment $< 1\ \mu_B$.

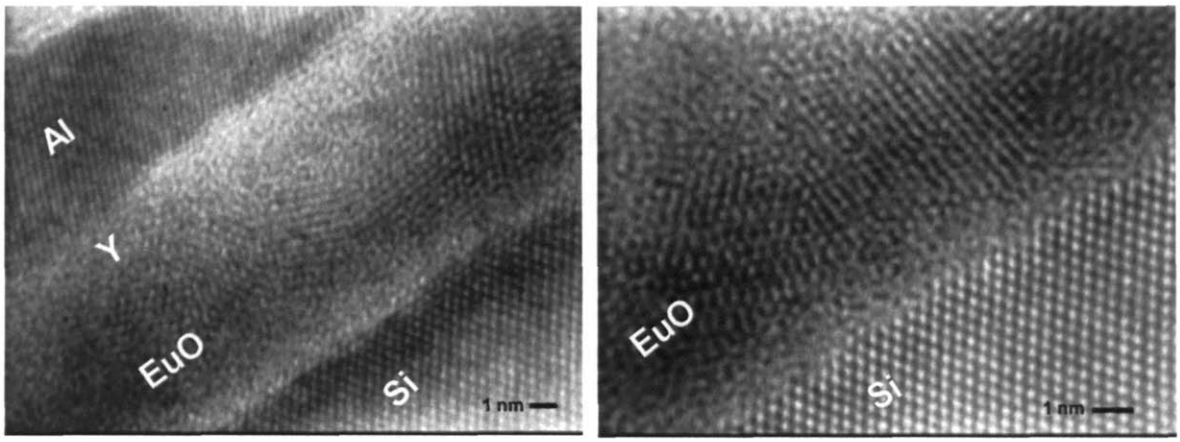

Figure 3-2: High resolution TEM images of a 3 nm EuO/2 nm Y/4 nm Al film grown on Si(100). Both images are of the same film, but in different regions and with different magnetifications.

3.2 Optical Properties

Optical absorption, shown in Figure 3-3, for 15 nm and 25 nm EuO films grown on quartz substrates closely resembles the absorption spectrum of an EuO crystal, replotted from Figure 1-2 for reference. The absorption edge at 1.1 eV corresponds to the expected optical band gap at room temperature. The film spectra also show the peak in absorption at ~2 eV, corresponding to the peak in the $5dt_{2g}$ DOS. The slightly higher value of the absorption coefficient for these two films relative to that of the bulk may be due to the fact that only transmission, and not reflectance of the films, was used to calculate the absorption coefficient. With a high-frequency dielectric constant = 4.3 [44], a small reflectance can be expected, which would lower the absorption coefficient.

3.3 Magnetic Properties

Typical magnetic properties of EuO films measured by the SQUID magnetometer are shown in Figure 3-4 for a 15 nm film. Magnetization M versus applied magnetic field H was measured at 5 K. M(H) shows strong ferromagnetic behavior, with a saturation magnetic moment per Eu^{2+} ion M_S=7.3 μ_B. Remanent magnetization M_r=6.3 μ_B (the magnetization remaining at H=0 after saturation) and coercive field H_C=55 Oe (field at which M=0 when switching to align with H) for this film. As shown in the temperature dependence of M, measured with H=50 Oe, the observed T_C closely matches the value of bulk EuO, 69 K. This is the typical magnetic behavior of "thick" EuO films, showing bulk-like properties. In

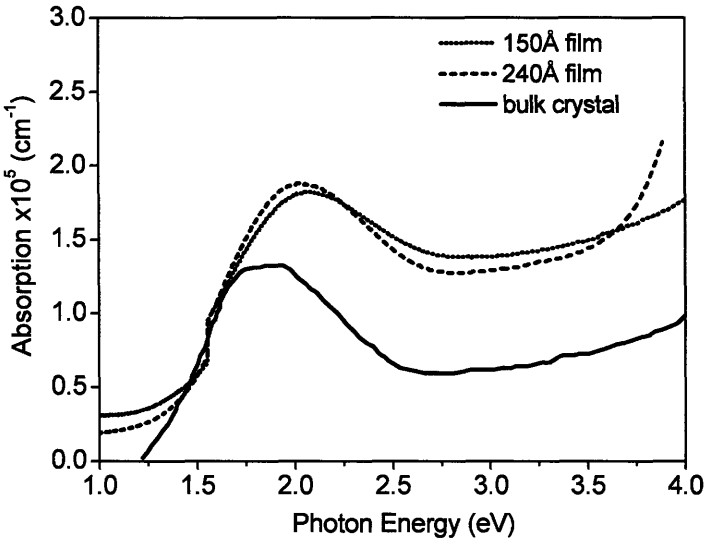

Figure 3-3: Absorption coefficient as a function of photon energy for two EuO films grown on quartz substrates with Al_2O_3 protection layer. These spectra follow that of bulk EuO, replotted from Figure 1-2.

their calculations Schiller *et al.* [78] found that EuO films show bulk-like properties for $\geq$25 monolayers, which is $\sim$6.5 nm. The magnetic properties of films $\leq$6 nm are discussed in Section 3.4.1.

3.4 Chemical Analysis and Interface Studies

In the XAS study of the EuO films, the capping layer material was found to effect the amount of Eu_2O_3 present in the film. Figure 3-5 shows the XAS spectra at the M_5 and M_5^* edges for ultra-thin EuO films capped with Y, Ag and Al. When compared to the EuO and Eu_2O_3 reference spectra at the bottom of the figure, it is clear that the EuO film capped with Y has no Eu_2O_3 peak, whereas the film capped with Ag has a large Eu_2O_3 peak. Thus, the Y layer best prevented further oxidation of the EuO film. When decomposing these XAS spectra into relative amounts of EuO and Eu_2O_3, the fraction of Eu_2O_3 present in the films with Y, Al and Ag capping layers was <5%, 28% and 41%, respectively. This result is in agreement with the tunneling spin-polarization measurement described in the next chapter, where the EuO tunnel barrier with a Y electrode had a higher spin-filter efficiency than EuO with a Ag electrode.

Y was used as the top electrode material for most samples in this study because it was found to minimize the presence of Eu_2O_3 at the top EuO interface. Eu_2O_3 likely formed while

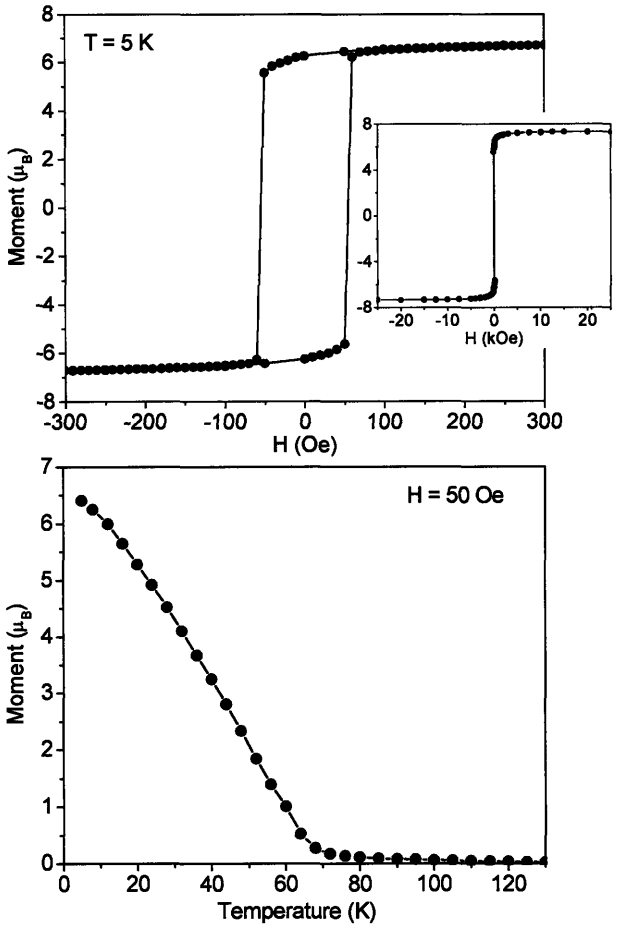

Figure 3-4: M(H) (top) and M(T) (bottom) for a 15 nm EuO film measured using the SQUID magnetometer. The M(H) curve is plotted for a small H range, so that the coercive field H_C=55 Oe and M_r=6.3 μ_B can been seen. The inset is the same M(H) in a larger field range, showing saturation giving M_S=7.3 μ_B. The T_C for this "thick," bulk-like film matches that of bulk EuO, 69 K.

the top EuO interface was exposed for a short time to the residual oxygen pressure in the chamber as the next source material was heated for evaporation. Because Y_2O_3 also readily forms (ΔH_f = -1760 kJ/mol [79]), Y likely pulled some oxygen away from Eu_2O_3, leaving a purer EuO phase. Thus, the interface between EuO and Y is not expected to be atomically smooth, which is the case in Figure 3-2, since there may be some Y_2O_3 present. Among all materials tested as the capping layer, EuO films capped with Y always had the best magnetic properties and superior chemical analysis by XAS, showing a negligible amount of the Eu_2O_3 phase, if any.

As mentioned above, formation of Eu_2O_3 at the top EuO interface was suspected to occur before deposition of the next layer. In order to determine if the Eu_2O_3 present in

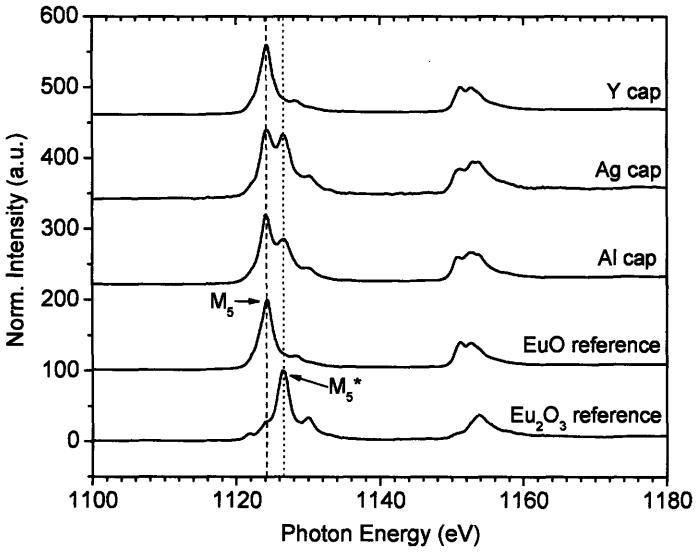

Figure 3-5: XAS spectra of the M_5 and M_5* edges for EuO films with three different capping layers—Y, Ag and Al, compared with the reference spectra of EuO and Eu_2O_3. Y is the best capping layer material for preventing further oxidation of EuO to form Eu_2O_3.

the film was mainly concentrated at the top interface, an angle-dependent XAS study was conducted on an 8 nm EuO film capped with Al, shown in Figure 3-6. At low incident beam angle, which is the angle between the incident x-rays and the plane of the film, the beam penetrates only the top portion of the sample. For the lowest angles, the M_5* peak is dominant, signifying that more Eu_2O_3 than EuO is present at the top interface. When increasing the incident beam angle, the x-rays penetrate deeper into the sample and the M_5 peak emerges, signifying that less Eu_2O_3 is present deeper into the film. The inset illustrates this change in relative concentration as the incident angle is varied, confirming that Eu_2O_3 forms at the top interface.

3.4.1 Wedge structures

The ideal way to study the film properties as a function of thickness was to make a wedge film, so that there was no variance in the deposition conditions. EuO wedge films were made in "opening shutter" mode, which means that the shutter was opened step-wise in a controlled manner during deposition to form the wedge steps, so that the top interface of all steps was identical.

Since the wedge steps were clearly visible on the substrate, the substrate could be cut so that each step was measured individually in the SQUID magnetometer. M(T) for two wedge samples, with EuO thickness 1 nm–6 nm in steps of 1 nm, is shown in Figure 3-7.

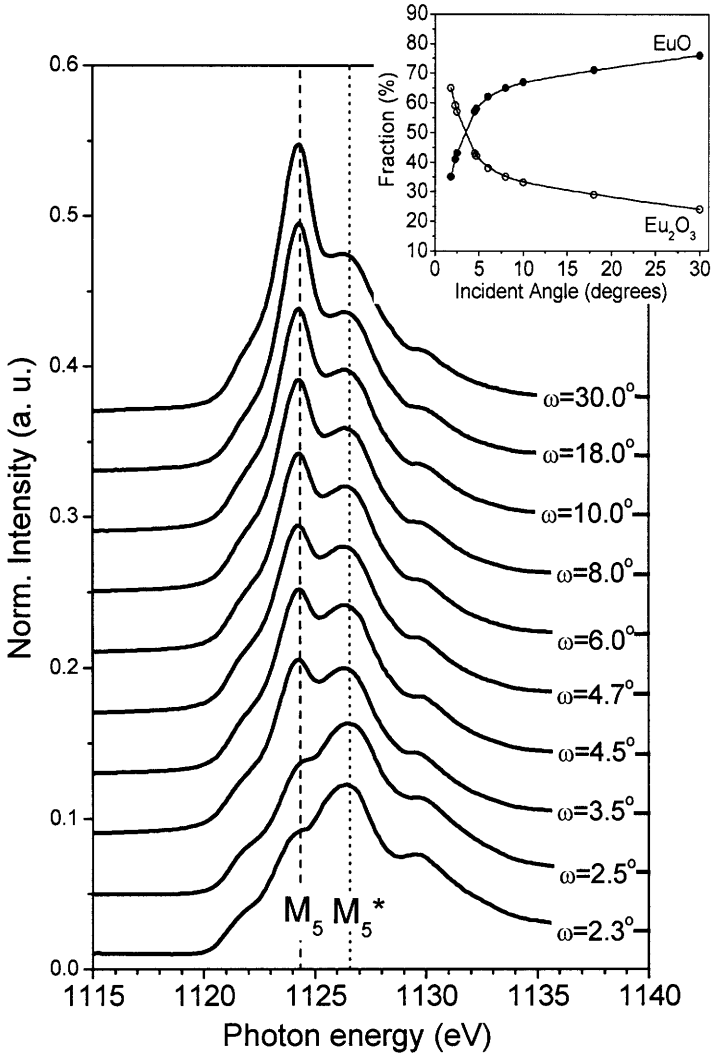

Figure 3-6: Angle dependence (angle ω of the incident x-rays to the sample surface) of the XAS spectra for an 8nm EuO film capped with Al. Larger ω probes deeper into the film and smaller ω probes the top interface. Larger M_5^* peak for smaller ω indicates that Eu_2O_3 is concentrated at the top EuO-electrode interface. The inset shows the relative fraction of EuO and Eu_2O_3 as a function of incident angle.

These samples have the following stucture: $Si/SiO_2//2$ nm Cr/9 nm Cu/1 nm—6 nm EuO wedge, with two different capping layers for comparison: 2 nm Y/8 nm Al and just 8 nm Al. Both wedges nicely show a clear trend of T_C reducing with film thickness. This trend was expected according to the calculations by Schiller *et al.* [77, 78] for ultra-thin EuO, as described in Section 1.7.1.

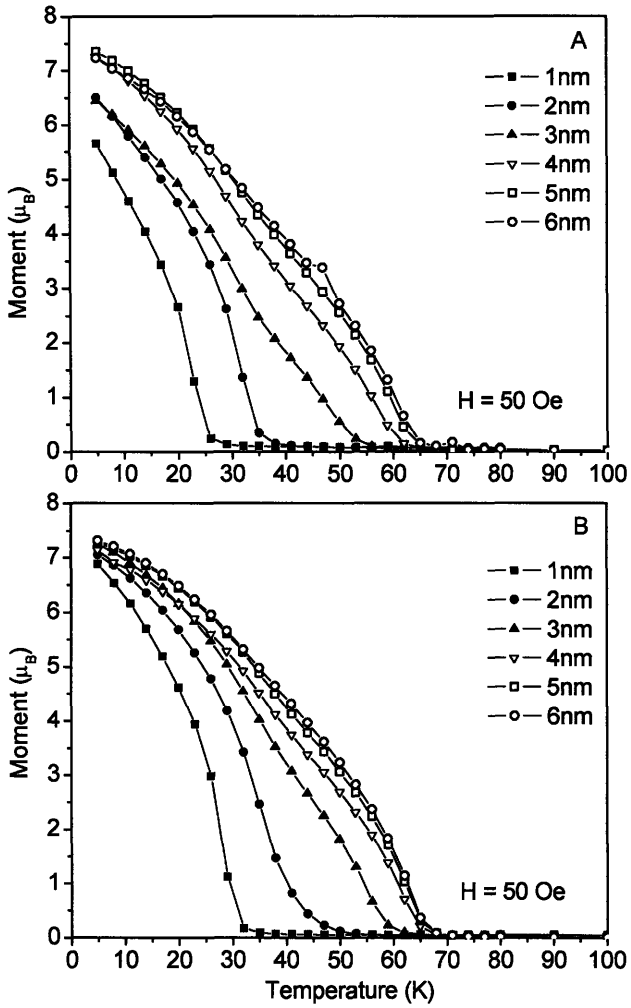

Figure 3-7: M(T) for ultra-thin EuO films deposited into a wedge structure, with thickness ranging from 1nm to 6nm, in steps of 1nm, measured at 5K in a field of 50 Oe. a) Wedge with 8nm Al capping layer, b) same wedge film with 2 nm Y/8nm Al capping layer. T_C clearly reduces with film thickness.

T_C as a function of thickness for these wedge films is compared with the theoretical calculation in Figure 3-8. The experimental data follows the trend given by the theory. However, the experimental T_C values are overall reduced from the theoretical values. The theoretical calculation was performed for free-floating, single-crystal EuO(100) films that are not interacting with any materials at the interface, which is physically unrealistic. The films in this study are polycrystalline, with properties that depend greatly on the interfacial materials. This must be taken into account, along with the possibility of having a small amount of Eu_2O_3, when comparing this experimental result with theory. Nevertheless, this

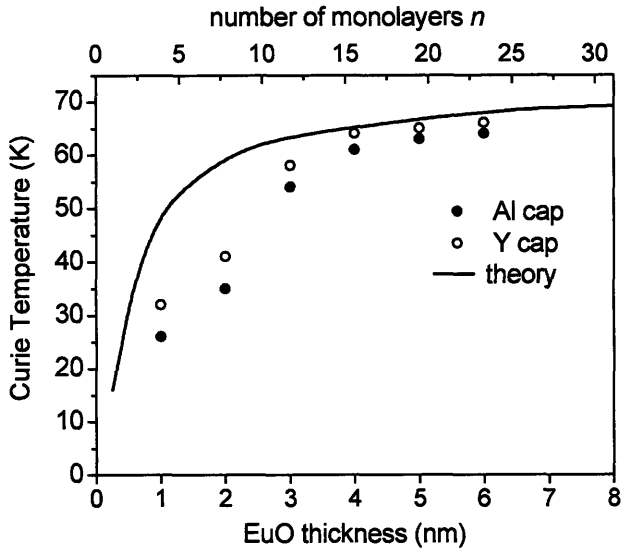

Figure 3-8: T_C as a function of film thickness for the wedge films, compared with the T_C calculation of Schiller *et al.* These wedge films are the same as those in Figure 3-7. The theoretical curve is replotted from Figure 1-5.

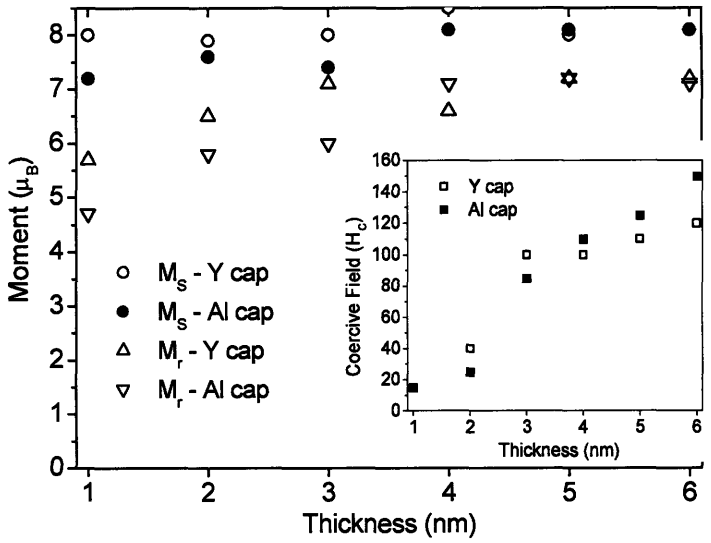

Figure 3-9: Saturation and remanent magnetizations for all wedge steps 1 nm—6 nm and both capping layers, 8 nm Al and 2 nm Y/8 nm Al. The inset shows the decrease in coercivity with film thickness. This is the same wedge sample as in Figures 3-7 and 3-8. M_S and M_r values are subject to up to 15% error (see text).

is the first experimental confirmation of this calculation. It may be noted that the Curie temperatures of the EuO wedge steps capped with Y are overall greater than those for Al, which again confirms that Y is the better capping layer material.

The magnetic properties—M_S, M_r and H_C—collected from the M(H) loops of the wedge steps are summarized in Figure 3-9. M_S stays above 7 μ_B for all steps, including the 1 nm step.[1] Thus, the moment for these ultra-thin films nearly matches the bulk value and does not vary with thickness. However, M_r is smaller for the thinner films. This reduction in M_r is likely due the higher surface to volume ratio for the thinner films, so that for the thinner films, there are more surface atoms that are not fully coordinated with neighboring moments and thus their exchange interaction is weaker. This is the same reason for the reduction in T_C, as described in Section 1.7.1. M_S remains constant with thickness, as the Eu^{2+} moments can align easily in the high magnetic field. Whereas, due to the weaker exchange interaction, M_r decreases with thickness since it is harder for the surface moments to stay aligned in the absence of the applied field.

The lower coordination number of the Eu^{2+} surface ions leads to smaller M_r for the thinner films, as described above, as well as lower H_C for the thinner films, as shown in the inset of Figure 3-9. The momentum of the electrons of the surface atoms is confined to the plane of the film, since they have a greatly reduced probability of traveling outside the material. The electron velocity in the surface plane produces an angular momentum vector that is perpendicular to the surface plane. Thus the moments at the surface have some component perpendicular to the surface plane. When the applied field is reduced, these surface moments are the first to misalign with the field. Because the field applies a torque to align the moment parallel to the field direction,[2] less field is needed to switch the direction of magnetization, resulting in lower H_C for the thinner films [68].

XAS and MCD analysis was conducted for this same EuO wedge capped with Y, shown in Figures 3-10 and 3-11, respectively. The fraction of EuO determined from XAS is as much as 93%. Note that the fit of these XAS curves using the reference spectra (Figure 2-3) actually resulted in 98% EuO and 2% Eu_2O_3, but the reference spectra themselves were found to have <5% of the other oxide. The fraction of EuO is high for all wedge steps (shown in the inset of Figure 3-10) and does not vary much with thickness, similar to the magnetic moment for all steps (recall Figure 3-9). One peculiar observation in the XAS spectra is that the 6 nm wedge step does not have the highest intensity, as would be expected. This may be explained by a saturation effect of the TEY mode [88] or by self-absorption processes for the thicker film, which cause a reduction in signal from the value that accurately reflects the rate of absorption.

[1]The values of M_S and M_r are subject to being too high by up to 15%. As previously described in Section 2.1.2, the thickness of the film may be up to 15% higher than the nominal thickness, subjecting M_S and M_r to this error as well. The expected saturation moment for bulk EuO is 7 μ_B (see Section 1.7.)

[2]Torque $\boldsymbol{\tau} = \mathbf{m} \times \mathbf{H}$, where $\mathbf{m}$ is the moment and $\mathbf{H}$ is the field, in CGS units. $\boldsymbol{\tau} = \mu_0 \mathbf{m} \times \mathbf{H}$ in MKS units [87].

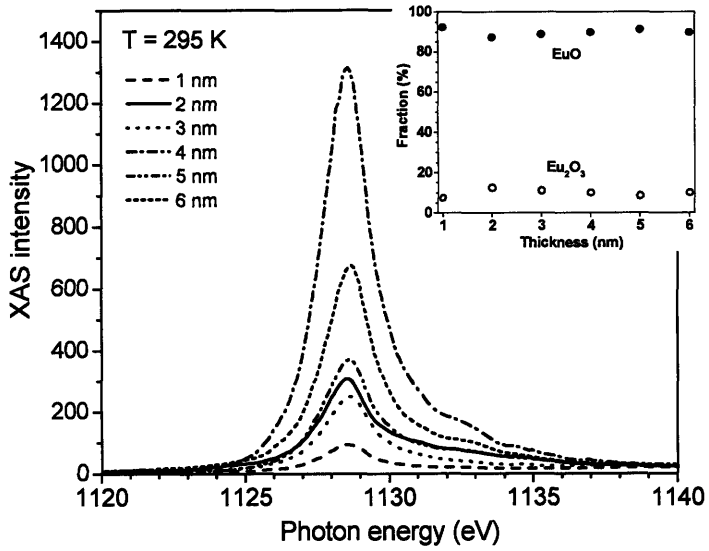

Figure 3-10: XAS at the M_5 edge for an EuO wedge film with the structure $Si/SiO_2//2$ nm Cr/9 nm Cu/1 nm–6 nm EuO wedge/2 nm Y/8 nm Al (same wedge as in Figure 3-7b.) The M_5 peak for EuO is clearly dominate in the spectra. The inset shows the fraction of EuO and Eu_2O_3 found from decomposing the XAS spectra against the EuO and Eu_2O_3 references.

The MCD measurement was taken at 18 K, which is the lowest temperature obtainable by the measurement setup at ALS, and MCD is displayed by all wedge steps.[3] A higher MCD signal would be expected at a lower temperature, in accordance with the M(T) data in Figure 3-7. Shown in Figure 3-11 is the difference intensity I^+-I^-, rather than the MCD signal (refer to Section 2.2.4). A suggested approach for reducing the saturation effect in the XMCD analysis is to carry out the spectra corrections (including a correction for incomplete polarization of the incident light and a correction for the angle of incident light) using the difference spectra, rather than the XMCD spectra [88]. The resulting difference spectra shows the trend of increasing signal with thickness (Figure 3-11b), as expected from the M(T) behavior and simply because a larger signal is expected from thicker films, except for the 1 nm step which is unclear at this time. Figure 3-11c shows that the normalized difference spectra for all thicknesses are coincident, confirming that the magnetic signal comes completely from EuO, with no contribution from Eu_2O_3, as expected.

An angle-dependent XAS measurement was also carried out on the 1 nm step of the wedge capped with Al, shown in Figure 3-12. Though the fraction of Eu_2O_3 is higher when the x-rays probe the top interface of the film, overall the fraction of EuO remains high

[3]The MCD technique can be used to determine the spin and orbital magnetic moments by applying the sum rules [83,89]. However, a clean MCD spectra at both the M_5 and M_4 edges is needed for this calculation, and the full spectra was not collected for these samples.

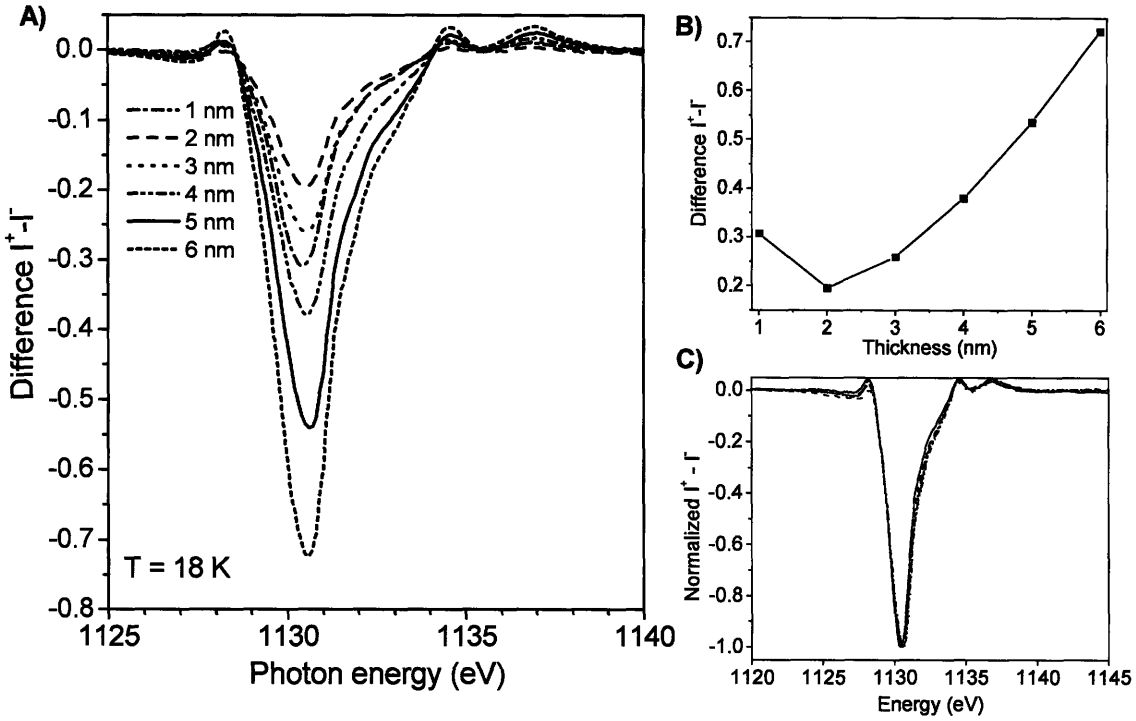

Figure 3-11: A) Difference spectra I^+-I^- at the M_5 edge, which corresponds to Eu^{2+}, measured at 18 K for an EuO wedge film with the structure Si/SiO_2//2 nm Cr/9 nm Cu/1 nm–6 nm EuO wedge/2 nm Y/8 nm Al (same wedge as in Figures 3-7b and 3-10). B) The inset shows the I^+-I^- intensity as a function of film thickness. C) The plot of normalized I^+-I^- signal for Eu^{2+} is coincident for all thicknesses, clearly showing that the magnetic contribution comes entirely from EuO (zero MCD from Eu_2O_3).

throughout the film depth. This measurement was done so that it could be compared with the previously described angle-dependent XAS measurement for the 8 nm EuO film capped with Al (Figure 3-6). Most notably, the EuO quality in this 1 nm film is markedly improved over the 8 nm film sample. This large difference in film quality is not be interpreted as an effect of the film thickness. Rather, because the 8 nm film was made toward the beginning of this Ph.D. project and the 1 nm film was made much later, this comparison elucidates the optimization of film preparation parameters to improve ultra-thin EuO quality over the duration of the project.

Cu was selected as the bottom electrode material in this wedge structure and in the MTJs (described in Section 5.1) because its lattice matches[4] that of EuO, and Cu is not as sensitive to oxygen as EuO. The Cr seed layer beneath the Cu was absolutely necessary for

[4]Cu has an FCC structure with a lattice constant a_{Cu}=0.361 nm, so that $\sqrt{2}a_{Cu}$ = 2 × Cu nearest neighbor distance $\approx a_{EuO}$.

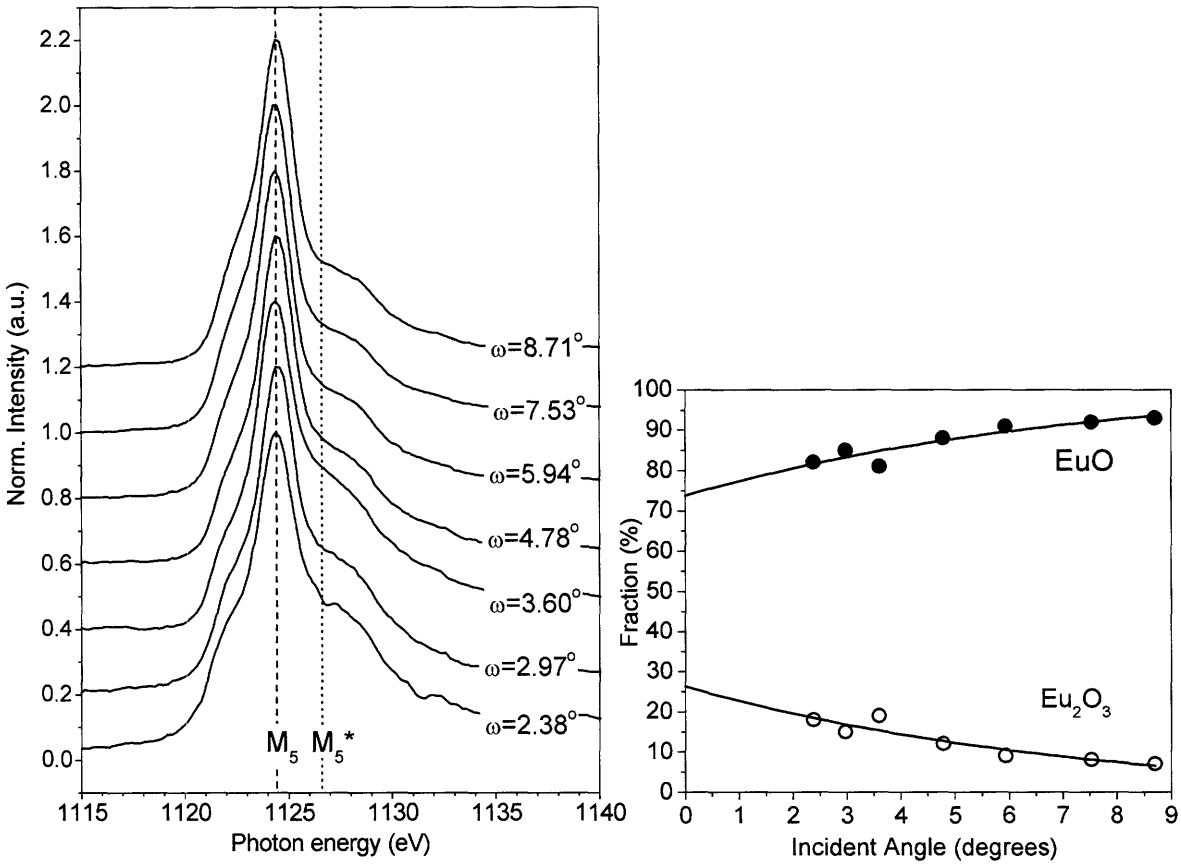

Figure 3-12: Left: Angle-dependent XAS spectra for a 1 nm EuO film capped with Al, showing a high fraction of EuO throughout the depth of the film. This sample is the 1 nm step of the wedge sample shown in Figures 3-7 and 3-9. Right: Relative fraction of EuO and Eu_2O_3 as a function of incident angle ω.

growth of a smooth Cu film and good quality EuO. In fact, if a Cr layer was not used, poor quality EuO on Cu resulted, with a moment <0.5 μ_B.

Chapter 4

Spin-Polarized Tunneling through EuO Barriers

In the previous chapter, the structural, optical, chemical and magnetic characterization showed that high quality EuO films were grown. However, due to its sensitivity to barrier and interface quality, spin-polarized tunneling is the best method to determine if a uniform, high-quality film at the monolayer level with clean interfaces was prepared successfully. The first half of this chapter shows the results of a direct measurement of spin polarization of the tunnel current through an EuO barrier, using a superconducting Al electrode as the spin detector. The principles of this technique were described in Section 2.3.1. The second half of this chapter explains how exchange splitting in an EuO tunnel barrier was observed and quantitatively determined, by using tunneling theory to describe the transport behavior.

4.1 Direct Polarization Measurement with a Superconducting Spin Detector

The tunnel junctions described in this section had an Al superconducting bottom electrode, EuO barrier and either a Y or Ag top electrode. The junctions were cooled to 0.45 K in a ^{3}He cryostat, and their I-V characteristics were measured using the Meservey-Tedrow technique, as described in Section 2.3.1. The tunneling dynamic conductance dI/dV versus bias voltage is shown in Figure 4-1a for a 4.5 nm Al/4.5 nm EuO/25 nm Ag junction. The superconducting transition temperature of the 4.5 nm Al was 2.2 K. Tunnel conductance was measured prior to applying a magnetic field (the initial H=0 curve). The superconducting energy gap of Al centered at V=0 was clearly observed. Then when a field H_{appl}=0.27 T was applied in the plane of the film, a large Zeeman splitting of the Al quasiparticle DOS was

observed. The magnitude of this splitting ($=2\mu_B H_0$) corresponds to a total effective field of H_0=3.50 T, even though H_{appl}=0.27 T. This enhanced Zeeman splitting is a consequence of a SC in direct contact with a ferromagnetic insulator and will be discussed in the next section. A polarization of $9 \pm 4\%$ was determined from the conductance curve, as the asymmetry indicated that the tunnel current was spin-polarized. As the electrodes were not FMs (and thus not a source for polarized spins), the measured P demonstrates that spin filtering was occurring in the EuO barrier. After reducing the applied field back to zero (H_{appl}=0 curve), the conductance continued to display Zeeman splitting. Furthermore, asymmetry of this curve shows that P remained even at zero field. This is due to the remanent magnetization state of EuO and the SC/FMI proximity effect (described in the next section). Although higher P was expected, this is a clear demonstration of spin filtering in an ultrathin EuO barrier.

A larger P was obtained when a Y top electrode was used, as shown in Figure 4-1(b) for a 4.2 nm Al/1.4 nm EuO/5 nm Y/10 nm Al junction. Conductance was measured initially in zero field and then at H_{appl}=0.10 T. Enhanced Zeeman splitting was observed for this junction as well, corresponding to a large effective field of H_0=3.90 T, when the applied field was only 0.10 T. A polarization of $29 \pm 4\%$ was determined from the spin-split, asymmetric conductance curve at H_{appl}=0.10 T. This higher P for EuO with a Y electrode than with Ag is in agreement with the XAS study discussed in Chapter 3, which confirmed that Y is a better capping layer than Ag for preserving the EuO stoichiometry.

The EuO barrier thickness for the junction in Figure 4-1a is 4.5 nm—thicker than that of the junction in Figure 4-1b, 1.4 nm. However, the junction area for the former is larger than the area of the latter. These junctions were made using different shadow masks. One difficulty of measuring junctions with semiconducting barriers is that the junction resistance rises greatly when lowering the temperature (discussed in Section 4.2). The dI/dV measurement of junctions with resistance >100 kΩ tends to be noisy. Using a larger area junction allows one to investigate thicker barriers, still maintaining a junction resistance of a few tens of kΩ or lower. A few different barrier thicknesses are made in a single run, and the thickness that falls within a manageable resistance range is the one measured.

4.1.1 Superconductor/Ferromagnetic Insulator Exchange Interaction

As mentioned in the previous section for the Al/EuO/Ag junction, an enhanced Zeeman splitting of the Al superconducting DOS was observed, corresponding to a total effective field of H_0=3.50 T, when the applied field was only 0.27 T (Figure 4-1a). The Zeeman

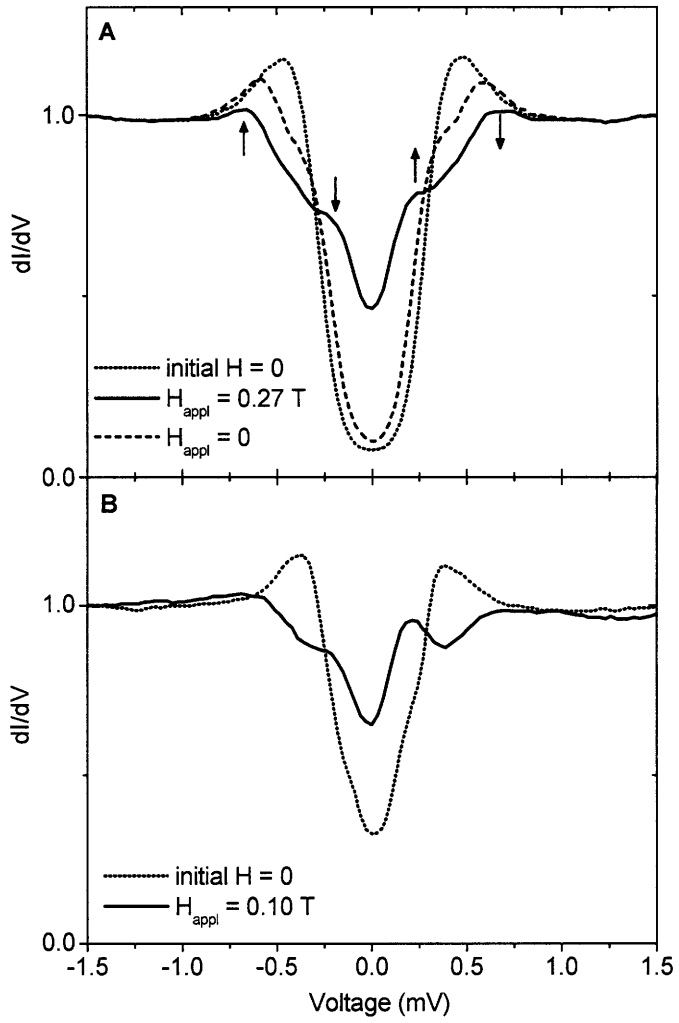

Figure 4-1: Tunnel conductance dI/dV as a function of applied voltage across junctions with an EuO tunnel barrier, measured at 0.45 K. a) dI/dV for 4.5 nm Al/4.5nm EuO/25 nm Ag junction, showing P=9±4%. b) dI/dV for 4.2 nm Al/1.4 nm EuO/5 nm Y/10 nm Al junction, showing P=29 ± 4%. The arrows mark the spin-up and spin-down conductance peaks, corresponding to the Zeeman-split, spin-up and spin-down DOS of the Al superconductor. Asymmetry of the conductance peaks indicate spin polarization of the tunnel current.

splitting was enhanced by the internal exchange field $H^*=H_0-H_{appl}=3.23$ T, produced by the ferromagnetically ordered Eu^{2+} ions acting on the conduction electrons in the Al by a proximity interaction at the EuO/Al interface [90, 91]. This enhanced Zeeman splitting is a clear indication that ferromagnetic EuO was present at the interface with Al.

Similarly for the Al/EuO/Y junction (Figure 4-1b), the amount of Zeeman splitting in the $H_{appl}=0.10$ T curve corresponds to a total effective field of $H_0=3.90$ T. Thus, there is

an even larger internal exchange field (H*=3.80 T) in this junction with a Y top electrode, compared to the junction with a Ag top electrode. Again, this is attributed to the better quality of EuO (having less Eu_2O_3 present) with the Y electrode. This is remarkable, given that only 1.4 nm of EuO is present in this case, showing the high quality of EuO down to this thickness range. In fact, because of such a high internal field in the EuO barrier, the Al was driven into normal state by an applied field of just 0.14 T, whereas the critical field for Al in contact with a non-magnetic Al_2O_3 barrier is ~5 T.

Zeeman splitting induced by the internal exchange field was observed in the final H_{appl}=0 curve for the Al/EuO/Ag junction (Figure 4-1a) but not in the initial zero field curve. This can be explained as due to the randomly magnetized, multidomain structure of the EuO film. Initially, at zero field, $L \ll \xi$, where L is the domain size and ξ is the superconducting coherence length. The domains were randomly oriented prior to applying the field, and the Al quasiparticles saw a net exchange field of zero over an area ξ^2. In the saturation condition (nearly single domain state) where $L \gg \xi$, a large exchange field resulted, leading to significantly enhanced Zeeman splitting. In the remanent magnetization state (H=0), a smaller internal exchange field still existed due to the remament magnetization of the EuO barrier, and splitting was still observed. However, for the Al/EuO/Y junction, careful observation shows Zeeman splitting and conductance asymmetry (polarization) in the pristine state, even *before* a field was applied (initial H=0 curve in Figure 4-1b). Since a larger portion of the barrier was EuO, with less Eu_2O_3 phase present as described earlier, the domains were larger and gave rise to a net average exchange field that induced Zeeman splitting in the Al. Notably, while P is a direct consequence of the spin-filter effect, enhanced Zeeman splitting is a separate consequence of the ferromagnetic ordering in EuO and an interfacial exchange interaction.

The enhanced Zeeman splitting of the Al superconducting DOS was also observed in all low temperature spin-polarized tunneling measurements with EuS and EuSe ferromagnetic tunnel barriers [42, 43, 91]. This phenomenon is unique to thin film ferromagnetic insulator/superconductor (FMI/SC) systems and is elegantly observed in these experiments. Sarma [92] and de Gennes [93] had predicted this phenomenon forty years ago as an exchange interaction between the ferromagnetically ordered ions in the FMI and the conduction electrons of the SC, which is analogous to a thin film superconductor in a uniform exchange field, shown schematically in Figure 4-2. Because the thickness d of the superconducting film is small, boundary scattering of the quasiparticles at the EuO/Al interface is dominant during conduction, during which they undergo an exchange interaction with the ordered Eu^{2+} ions. The resulting exchange field acts solely on the electron spins, and not on electron motion [92,93]. Thus it causes Zeeman splitting, which is a spin effect, and has a negligible

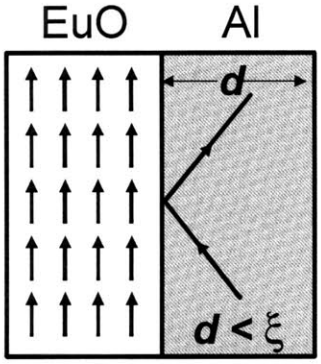

Figure 4-2: Schematic of the ferromagnetic insulator/superconductor exchange interaction at the EuO/Al interface. The Al quasiparticles scatter off the EuO/Al interface during conduction, where they experience an exchange interaction with the ferromagnetically ordered Eu^{2+} ions. This interaction causes Zeeman splitting of the Al superconductor, even in the absence of an applied field, as seen in Figure 4-1.

effect on orbital depairing in the SC. de Gennes predicted that the magnitude of the field is inversely proportional to d, for $d < \xi$. This FMI/SC interaction occurs only when the FMI and SC are in immediate proximity to each other. For example, the effect was lost when a thin layer of Al_2O_3 was inserted at the FMI/SC interface. This FMI/SC proximity effect was studied in detail with the Al/EuS system by Hao *et al.* [91]. Observation of the FMI/SC interaction in this study, along with the measured polarization, confirmed that the EuO barrier was strongly ferromagnetic.

4.1.2 Improving the Interface

The junctions described above produced a significant amount of polarization and clearly displayed spin filtering in the EuO barrier. However, this result was not reproducible over the several tens of junctions measured using the Meservey-Tedrow technique. Most of the junctions showed enhanced Zeeman splitting, signifying a ferromagnetic EuO barrier, but the conductance measurements were completely symmetric, indicating zero P. This may be attributed to spin scattering at the Al/EuO interface. It is possible that the EuO barrier was filtering the spins, but P was suppressed due to scattering at a defective Al/EuO interface. It may also be due to defects inside the barrier, which give rise to states in the barrier that enhance the tunneling probability for unpolarized spins.

It may be possible to find cause for the defective interface when taking a closer look at the junction fabrication process. After the thin Al electrode was deposited onto the liquid-nitrogen cooled substrate, the substrate was then warmed to room temperature. This

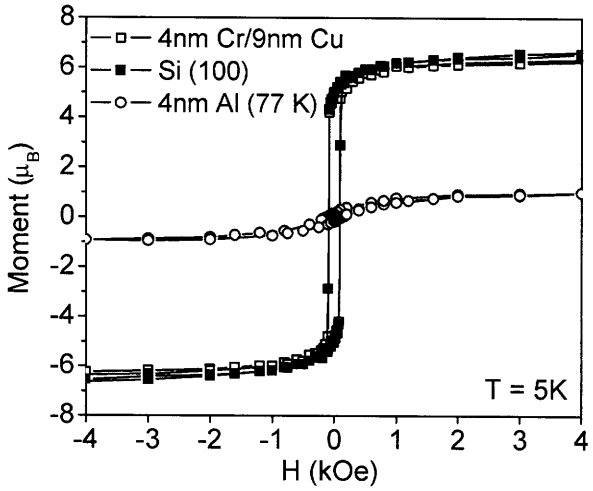

Figure 4-3: Comparison of M(H) loops for 3 nm EuO grown on HF-dipped Si(100), 4nm Cr/9 nm Cu, and Al underlayers. The Al layer was grown on a liquid-nitrogen cooled substrate, exactly as prepared for low temperature tunneling measurement. EuO grown on Al is clearly of poorer quality than the same EuO film grown on Si or Cu.

process took over one hour, during which time the Al surface could have adsorbed oxygen from the background pressure in the vacuum system. Furthermore, the Al surface was exposed to the oxygen flow as it was adjusted in preparation for the EuO deposition. EuO then competed with Al for oxygen (Al_2O_3 ΔH_f = -1676 kJ/mol [79]), so that the resulting interface was likely some mixture of AlO_x, Eu_2O_3 and EuO. A M(H) loop measured by the SQUID magnetometer, shown in Figure 4-3, confirmed the poor quality of the EuO barrier grown on Al, compared with EuO grown on Cu or HF-dipped Si, which do not react as readily with oxygen or moisture as does Al. Thus unfortunately, the EuO barriers grown on Al for spin-polarized tunneling measurement were somewhat of poorer quality, with a defective interface with Al.

One approach for avoiding this Al/EuO interface problem would be to grow the Al electrode on *top* of the EuO. However, this would present a different problem of having to cool the substrate to liquid-nitrogen temperture in preparation for the Al deposition—a process that takes over one hour, during which time the EuO barrier would be left unprotected. Instead, an interface engineering approach was taken, whereby 0.4 nm Mg was deposited on the Al electrode (after it was warmed up to room temperature), before EuO deposition. Mg metal is highly reactive with oxygen and MgO is a very stable oxide. Any adsorbed oxygen on the Al surface would react with Mg to form MgO, and would be less likely to give oxygen to EuO. The dI/dV measurement of such junctions prepared with this interfacial Mg layer, compared to junctions made at the same time without the Mg layer, is shown in Figure

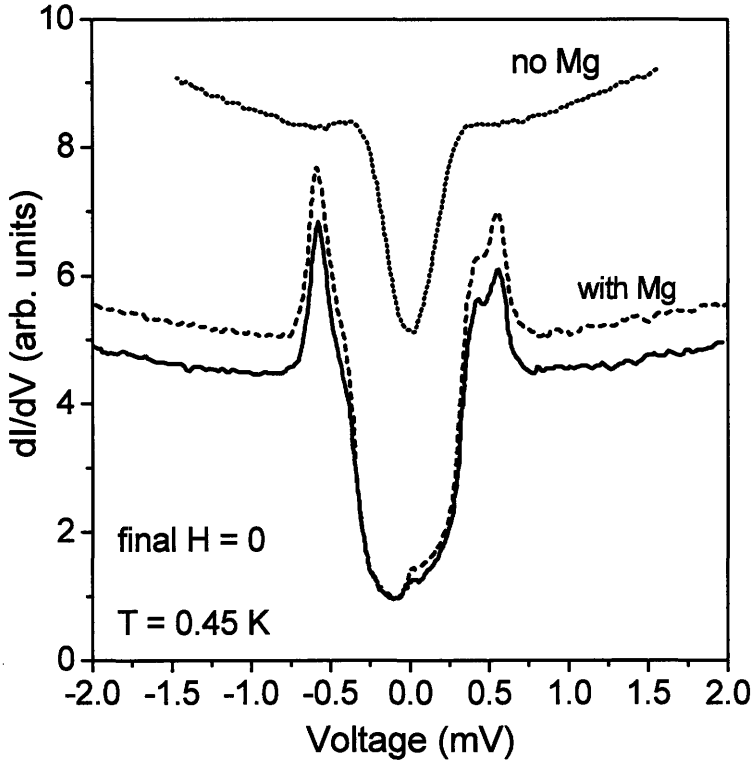

Figure 4-4: dI/dV of 3.6 nm Al/1.5 nm EuO/4.0 nm Y/8.0 nm Al junctions. The curves of the junctions with 0.4 nm Mg inserted at the Al/EuO interface show spin filtering, whereas the one without Mg does not. The measurement was done after applying a field, and then returning to zero field.

4-4, and a clear difference is observed. The junctions with the interfacial Mg layer display Zeeman splitting and P~30% at zero applied field, whereas the junctions without Mg show no Zeeman splitting and zero P. The junctions without Mg did not show P even when a field was applied to cause Zeeman splitting. Even though the interfacial Mg layer improved the EuO barrier and the interface, a higher P than the previous values (Figure 4-1) was not obtained. A possible explanation for this is discussed in the next section.

4.2 Quantifying Exchange Splitting and Polarization

Because the T_C for ultra-thin EuO films is reduced from bulk value, as discussed in Section 3.4.1, the question arises if there is a reduction in the amount of exchange splitting in the EuO conduction band as well. Exchange splitting $2\Delta E_{ex}$ in the europium chalcogenides in bulk form was quantified in optical measurements of the red shift of the absorption edge by ΔE_{ex} (discussed in Section 1.6). Through their optical experiments, Schoenes and Wachter [62]

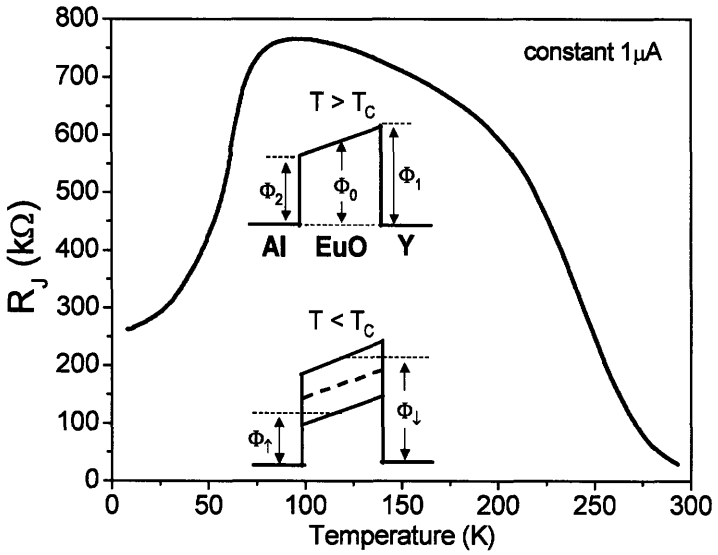

Figure 4-5: R_J(T) for a 3.6 nm Al/0.4 nm Mg/2.5 nm EuO/4.0 nm Y/8.0 nm Al tunnel junction, measured with a constant 1μA current, with the positive lead on the Y electrode. EuO barriers show a unique R_J(T) behavior, in which a R_J drops dramatically below T_C, due to exchange splitting in EuO and the resulting decrease in spin-up barrier height, shown in the inset.

described the exchange splitting of the conduction band due to magnetic order by:

$$H_{ex} = 2\Delta E_{ex} = -2\sum J_n(r - R_n)\,\mathbf{s}\cdot\mathbf{S_n}, \tag{4.1}$$

where $\mathbf{s}$ is the spin of a conduction electron, $\mathbf{S_n}$ are the spins of neighboring Eu^{2+} ions, and $J_n(r - R_n)$ is the distance-dependent exchange constant between electron and ion spins. Therefore, due to the large number of surface ions in ultra-thin EuO, with fewer nearest neighbors than bulk ions, one can expect to see a reduced ΔE_{ex}. Exchange splitting of ultra-thin EuO is quantitatively determined in this study by using a tunneling measurement.

Evidence of exchange splitting in EuO tunnel barriers was clearly observed on a regular basis while measuring tunnel junction resistance (R_J) as a function of temperature (T). For non-magnetic tunnel barriers, R_J increases by 10–20% when T decreases, due to a reduction in thermal excitations. For example, a junction with an Al_2O_3 barrier increases in R_J by a ~20% when cooling from room temperature to 4 K. However, an EuO barrier exhibits a unique R_J(T) behavior due to exchanging splitting of the conduction band for $T<T_C$. The R_J(T) measurement in Figure 4-5 is for an Al/2.5 nm EuO/Y junction, in which the electrodes Al and Y have a DOS that is not spin-polarized. As the junction is cooled from room temperature, R_J rises rapidly, which is typical of semiconductor tunnel barriers [32,33].

For T>T_C the barrier height is Φ_0 for both spin-up and spin-down electrons, as shown in the top inset of Figure 4-5. However, when the junction is cooled below T_C, R_J drops dramatically. This drop in R_J is caused by exchange splitting in EuO, which results in a lower barrier height for spin-up electrons ($\Phi_\uparrow$), such that $\Phi_\uparrow < \Phi_0$. Because of the exponential dependence of the tunnel current on barrier height (recall Equation 1.5), R_J decreases. As shown in the bottom inset of Figure 4-5 for T<T_C, $\Phi_\uparrow$ is lowered by an amount ΔE_{ex} from Φ_0, and $\Phi_\downarrow$ is raised by an amount ΔE_{ex} from Φ_0. This is the essence of the spin filter effect (described in Section 1.3) and results in a highly spin-polarized tunnel current.

The R_J(T) and the I-V curves at various T can be evaluated quantitatively to extract values for the initial barrier height Φ_0, $2\Delta E_{ex}$ ($=\Phi_\downarrow - \Phi_\uparrow$), and spin polarization of the tunnel current. A model by Brinkman, Dynes and Rowell (BDR) [11] describes the I-V behavior for the tunnel current through an insulating barrier between two electrodes, where the barrier potential has an asymmetric, trapezoidal shape, such as in Figure 4-5 inset. The trapezoidal shape of the barrier potential takes into account the different work functions of the metal electrodes, which give rise to different potentials Φ_1 and Φ_2 on either side of the barrier. The BDR relation is based on the WKB approximation and is widely used to extract the average barrier height $\bar{\Phi} = (\Phi_1 + \Phi_2)/2$, barrier asymmetry $\Delta\Phi = \Phi_2 - \Phi_1$ and barrier thickness d in nanometers and is given below:

$$J(V) = G_0 \left[V - \left(\frac{A_0 \Delta\Phi}{32\bar{\Phi}^{3/2}} \right) (eV)^2 + \left(\frac{3A_0^2}{128\bar{\Phi}} \right) (eV)^3 \right] \tag{4.2}$$

$$G_0 = \frac{e^2\sqrt{2m}}{(2\pi)^2\hbar^2} \left(\frac{\bar{\Phi}^{1/2}}{d} \right) \exp\left(-\frac{2d}{\hbar}\sqrt{2m\bar{\Phi}} \right), A_0 = \frac{4d}{3\hbar}\sqrt{2m}, \tag{4.3}$$

where J is the tunnel current density (current divided by junction area). J(V) is essentially a cubic function of V. This model is valid in a limited bias range—typically less than one-third of the barrier height [94]—because the model assumes that Φ is not a function of V, which is not the case as V approaches the barrier height [11].

Figure 4-5 shows R_J(T) measured with a constant 1 μA current applied, so that the voltage across the junction and thus the barrier profile is constantly changing with T. A more convenient way to observe the R_J(T) behavior is to make the measurement with a constant applied bias, such that the barrier profile stays the same as T changes and the effect of the exchange splitting below T_C can be more easily evaluated. Figure 4-6a shows R_J(T) for the same junction at different applied bias, with the bias defined with respect to

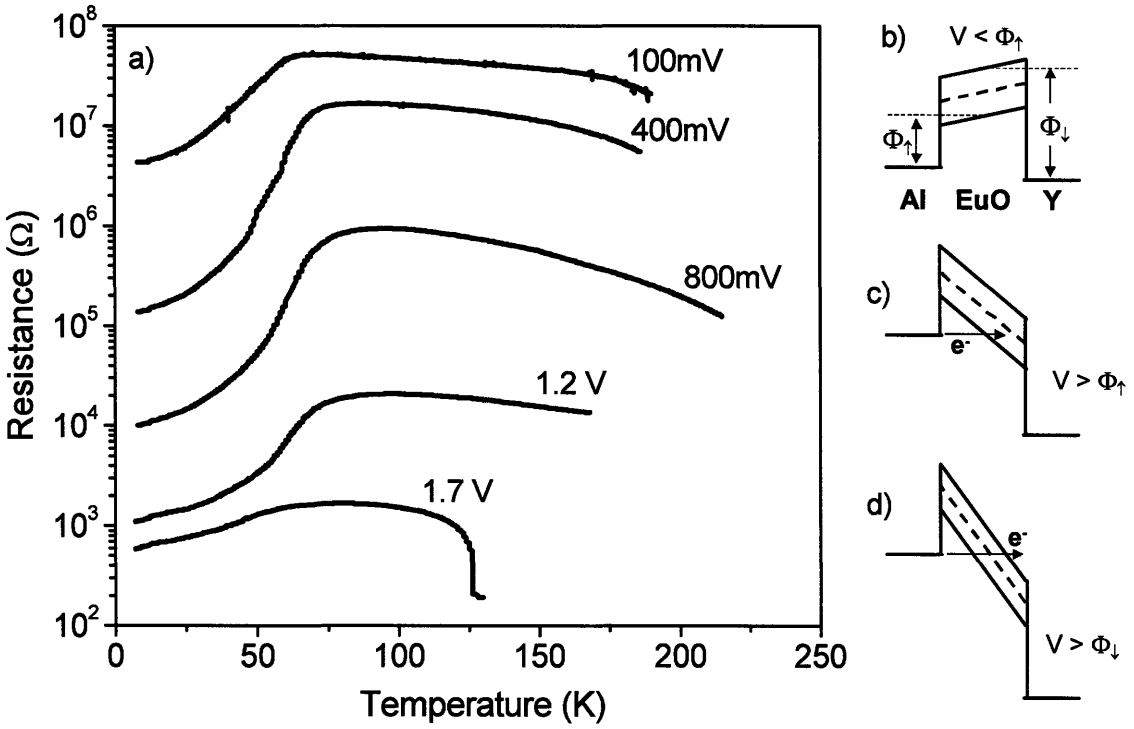

Figure 4-6: a) R_J vs T for a 3.6 nm Al/0.4 nm Mg/2.5 nm EuO/4.0 nm Y/8.0 nm Al junction (the same junction as in Figure 4-5, measured repeatedly with the different, applied voltages indicated. R_J decreases as T decreases below T_C of the EuO barrier. At very high applied bias 1.7 V, the junction breaks down during measurement at 125 K. b) Tunnel barrier profile for V< $\Phi_\uparrow$, where direct tunnling occurs. c) $\Phi_\uparrow$ <V< $\Phi_\downarrow$, where FN tunneling of spin-up electrons into the EuO conduction band occurs. d)$V > \Phi_\downarrow$, where FN tunneling into the EuO conduction band occurs for both spin-up and spin-down channels.

the Y top electrode.[1] R_J decreases below T_C for all biases. The magnitude of the resistance drop increases from the V=100 mV curve to the 400 mV curve, and notably at V=400 mV, R_J drops by *two orders of magnitude*! This is a singular R_J(T) behavior for a tunnel junction, that arises from the spin-filter tunnel barrier and is a clear indication that EuO is filtering spins. The magnitude of the resistance drop at 800 mV is slightly reduced from the one at 400 mV, and then greatly reduced for 1.2 V and 1.7 V, which are rather too high voltages to apply across the barrier. In fact, the sharp drop in R_J at 125 K for the 1.7 V curve is the breakdown point of the junction. Nevertheless, these high bias measurements also show a drop in R_J below T_C, and thus EuO is still filtering spins at these very high voltages.

[1] R_J(T) was measured with a negative applied bias as well, which showed a similar behavior to the positive bias measurements. However, do to asymmetry of the barrier, R_J was higher for negative bias and the measurement was more noisy. Thus, all of the measurements displayed here are with positive bias.

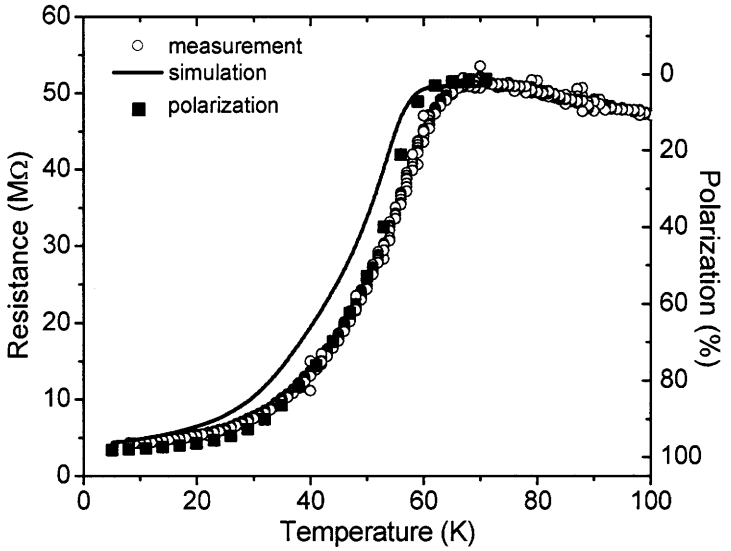

Figure 4-7: $R_J(T)$ measured with constant 100 mV applied bias (from Fig. 4-6a) and $R_J(T)$ simulated from the M(T) data of a 3nm EuO film. The simulation uses the BDR relation and assumes that $M(T) \propto 2\Delta E_{ex}(T)$. The corresponding P value (solid squares), determined from the BDR fit, is plotted on the right axis.

This clear evidence of spin filtering at high biases $\geq$100 mV is a significant result because it shows that EuO efficiently filters spins at finite bias, which is relevant for operating a spin device. This is in contrast to conventional magnetic tunnel junctions (without a spin filter), that show a decrease in magnetoresistance effect with increasing bias [9]. Thus, a device utilizing an EuO spin filter is not restricted to operating at very low biases, which makes it less susceptible to noise.

As mentioned above, the BDR relation is only valid at low voltages. Thus, only the $R_J(T)$ measurement for V=100 mV from Figure 4-6a was used to quantify Φ_0, $2\Delta E_{ex}$, and P, and is replotted in Figure 4-7 for clarity. The I-V curve at 98 K, for which there is no exchange splitting, was fit to Equation 4.2, yielding d=3.1 nm, $\bar{\Phi} = \Phi_0$=0.92 eV, and $\Delta\Phi$ =0.08 eV. Then, holding these values constant, the I-V curve at 6 K was fit to the BDR relation. At 6 K there are two different tunnel barrier heights $\Phi_\uparrow$ and $\Phi_\downarrow$ and thus two corresponding tunnel currents $J_\uparrow$ and $J_\downarrow$, respectively. Thus, the I-V curve was fit to the BDR relation by varying $2\Delta E_{ex}$ ($=\Phi_\downarrow - \Phi_\uparrow$) such that $J=J_\uparrow+J_\downarrow$, which yielded values $\Phi_\uparrow$=0.78 eV and $\Phi_\downarrow$=1.07 eV and $2\Delta E_{ex}$=0.29 eV.

In this way, the amount of exchange splitting for an ultra-thin layer of EuO was quantitatively determined for the first time via a tunneling measurement. The exchange splitting is reduced from its bulk value (=0.54 eV). Nevertheless, it is still quite sizable for this ultra-

thin tunnel barrier. In addition, this I-V fitting analysis supplied values for $J_\uparrow$ and $J_\downarrow$, and by simply using the equation $P=(J_\uparrow-J_\downarrow)/(J_\uparrow+J_\downarrow)$ (previously defined in Section 1.3) to calculate polarization, P was found to be 98%! Thus exchange splitting of 0.29 eV is enough to generate a nearly fully spin polarized current. P as a function of T is also shown in Figure 4-7, where P varies from zero before exchange splitting occurs and increases while $2\Delta E_{ex}$ increases until reaching 98% at $2\Delta E_{ex}$=0.29 eV.

Furthermore, a correlation was made between this $R_J(T)$ tunneling measurement and magnetization of the EuO film. The $R_J(T)$ curve was simulated from the M(T) behavior measured by the SQUID magnetometer for a 3 nm EuO film with a Y top electrode, shown in Figure 3-7. The simulated curve (shown in Figure 4-7) was generated by using the BDR relation and assuming that $2\Delta E_{ex}(T) \propto M(T)$. There is excellent agreement between the $R_J(T)$ tunneling measurement and the one simulated from the magnetization data.

While near complete P was already found from the drop in R_J below T_C for the V=100 mV curve, the $R_J(T)$ curves for V=400 mV and 800 mV in Figure 4-6a display a significantly larger drop in R_J below T_C. There is another tunneling phenomenon at play to account for this even larger drop in $R_J(T)$ for the V=400 mV and 800 mV curves, and also the smaller drop in $R_J(T)$ for the 1.2 V and 1.7 V curves at very high bias. The change in tunneling mechanisms for increasing applied bias is shown schematically in Figures 4-6(b–d). The BDR relation applies for small biases well below $\Phi_\uparrow$ shown in Figure 4-6b. However, for $\Phi_\uparrow < V < \Phi_\downarrow$ (Figure 4-6c), the electrons at the Fermi level in the Al electrode tunnel into the spin-up conduction band via Fowler-Nordheim (FN) tunneling[2] [95], whereas the spin-down electrons still tunnel through the barrier. Note that the effective barrier thickness is reduced for the spin-up channel as well. This is the bias regime where spin-filtering is most efficient, and a larger drop in R_J is produced. Since P=98% was deduced from the magnitude of the resistance decrease in $R_J(T)$ for V=100 mV, this larger decrease in the V=400 mV measurement implies complete spin polarization, P=100%. When even higher bias is applied such that $V > \Phi_\downarrow$ (Figure 4-6d), *both* spin-up and spin-down electrons undergo FN tunneling into the EuO conduction band, and P is suppressed. This describes the $R_J(T)$ behavior for V=1.2 V and 1.7 V, in which a smaller drop in R_J is observed. This is a qualitative explanation of the bias dependence of $R_J(T)$.[3] A quantitative model describing the $R_J(T)$ and I-V behavior for higher voltages, that takes into account the direct tunneling and FN tunneling regimes for both spin-up and spin-down electrons and $2\Delta E_{ex}(T)$, is needed to accurately determine the the barrier profile and P at higher bias.

[2] i.e., field emission, characterized by an exponential bias dependence

[3] A similar explanation describes the unique bias dependence of TMR in MTJs with EuS spin filter barriers [96, 97].

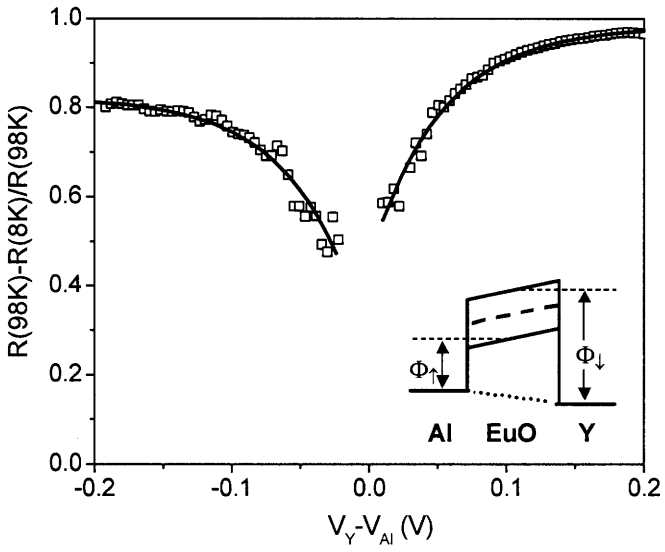

Figure 4-8: The decrease in $R_J(T)$ as a function of applied bias, for the same junction as in Figure 4-6. The lines show the trend, indicating that the amount of decrease in $R_J(T)$, which is proportional to P, is smaller at low bias. The inset is a schematic of low-level, defect states in the barrier that provide a spin-independent conduction path, thus reducing the spin-filter efficiency.

Finally, an insightful observation from this analysis was the variation in the magnitude of the resistance drop as a function of bias in the low bias regime, shown in Figure 4-8. The curve could not be completed for very low biases approaching zero because R_J at very low bias was too high for the measurement setup. Nevertheless, a trend of decreasing resistance drop for smaller voltages is clearly displayed. Because the amount of resistance drop is related to P, as described above, this trend is in agreement with the smaller P values obtained using the Meservey-Tedrow technique, which probes within only ± 2 mV of the Fermi level. Interestingly, the Meservey-Tedrow measurement in Figure 4-4 is for a 1.5 nm EuO barrier from the same sample set as the 2.5 nm EuO barrier in the $R_J(T)$ measurements (Figures 4-5 through 4-8). The $R_J(T)$ analysis using the BDR relation for this 1.5 nm EuO junction yields $2\Delta E_{ex}$=0.10 eV, Φ_0=0.35 eV and P=97% —thus the P deduced from this analysis is much greater than P directly measured using the superconducting spin detector at low bias.

When considering possible reasons for the difference in P found by the two approaches, it is important to note that the $R_J(T)$ measurement does not probe the spins, whereas the Meservey-Tedrow method directly probes the spins with a superconductor, thus any loss of spin information due to defect scattering is certainly reflected in the conductance measurement. The important information gained from the $R_J(T)$ measurement is the amount of exchange splitting; the $R_J(T)$ measurement clearly shows that exchange splitting is occur-

ring, which is the mechanism that gives rise to the spin-filter effect. The P value that is deduced from $J_\uparrow$ and $J_\downarrow$ as a consequence of the BDR fit, is the P value that is obtained for the amount of exchange splitting, but spin scattering is not taken into account. For example, the lower P found by direct measurement using the Meservey-Tedrow technique could be due to the presence of defect states in the barrier just above the Fermi level, shown schematically in the inset of Figure 4-8. Transport at low bias could be dominated by these defect states, which scatter the spins, but at high bias the effect of these low-level, defect states is minimal. Evidence for these low-level, defect states in the EuO barrier is given in the next chapter, which focuses on magnetic tunnel junctions with EuO barriers.

Chapter 5

Tunnel Magnetoresistance with EuO barriers

The previous chapter showed how a superconductor was used to directly determine the spin polarization of the tunnel current through EuO. This chapter describes how a *ferromagnet* was used as a spin detector to show spin-filtering in EuO, in a magnetic tunnel junction structure. The chapter begins with a description of the operating principle for conventional MTJs, and how this principle is extended to spin-filter MTJs. Then the results of two different spin-filter MTJ structures is described in detail—one in which Gd is the ferromagnetic spin detector, yielding high TMR, and other in which Co is the detector, showing an unexpected, negative TMR.

Conventional MTJs such as those used in MRAM and as read heads in hard drives comprise of two FMs separated by a non-magnetic insulator (NMI), such as Al_2O_3. The origin of TMR in these junctions is shown schematically in Figure 5-1. When the two ferromagnetic electrodes are magnetized parallel to each other, the majority (minority) spins easily tunnel from one electrode into the available majority (minority) states of the counter-electrode—this is the low resistance state (R_P). When the FMs are magnetized anti-parallel to each other, for the majority spin channel there are fewer empty majority states in the counter-electrode—this is the high resistance state (R_{AP}). TMR is the ratio $\Delta R/R=(R_{AP}-R_P)/R_P$. Jullière related $\Delta R/R$ to the spin polarization of the ferromagnetic electrodes (Equation 1.3), pointing out that higher P yields higher TMR.

In order to observe TMR, the two FMs must be magnetically uncoupled and have different coercive fields, so that they can reach both parallel and antiparallel alignment of magnetization as the magnetic field is swept during measurement. Ideally, the two FMs are decoupled by the insulating barrier so that they switch magnetization directions independently of each

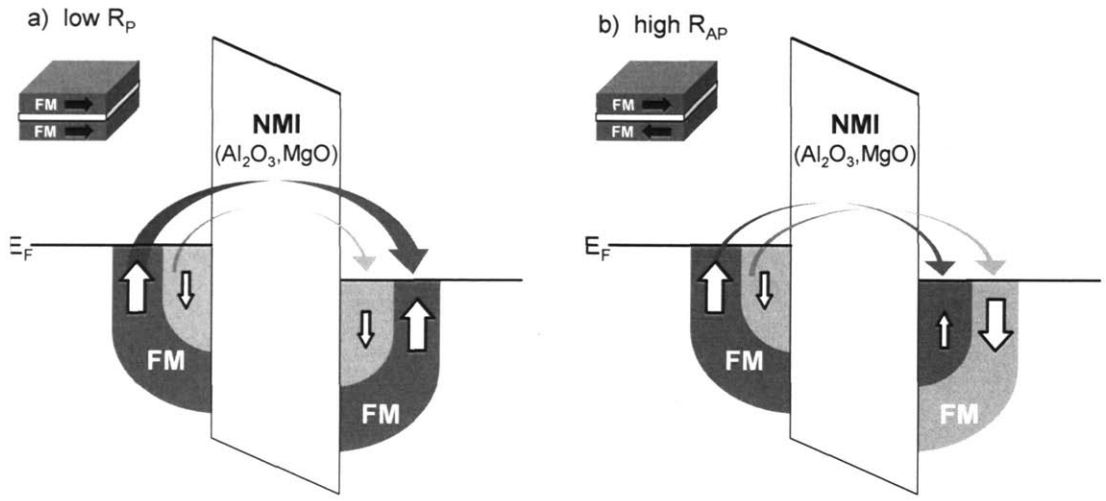

Figure 5-1: Schematic of the spin DOS for a conventional FM/insulator/FM magnetic tunnel junction, showing the origin of TMR=(R_{AP}-R_P)/R_P. The low resistance state (R_P) results when the two FMs are magnetized parallel to each other (a), and the high resistance state (R_{AP}) results when they are magnetized anti-parallel (b).

other and *complete* parallel and antiparallel alignment is reached. For a detailed review of MTJs, see Ref. 9.

The operating principle of a spin-filter MTJ is slightly different from conventional MTJs. The spin-filter MTJs in this study have a ferromagnetic EuO barrier sandwiched between a non-magnetic electrode and a ferromagnetic electrode, shown schematically in Figure 5-2. When EuO and the FM are magnetized parallel to each other, EuO filters the spin-up electrons, which tunnel easily into the spin-up DOS of the FM—this is the low resistance state. If the FM is reversed with respect to EuO, creating anti-parallel alignment of their magnetizations, EuO still filters the spin-up electrons, but there are fewer spin-up states available in the FM—this is the high resistance state. The TMR ratio is defined in the same manner as in conventional MTJs. To obtain large TMR, complete parallel and antiparallel alignment of the spin filter and the FM is also desired. The FM acts as the spin detector, so that if P of the FM is known (P_{FM}), Jullière's formula can be applied to determine the spin-filter efficiency of the barrier (P_{SF}):

$$\frac{\Delta R}{R} = \frac{R_{AP} - R_P}{R_P} = \frac{2P_{FM}P_{SF}}{1 - P_{FM}P_{SF}}. \tag{5.1}$$

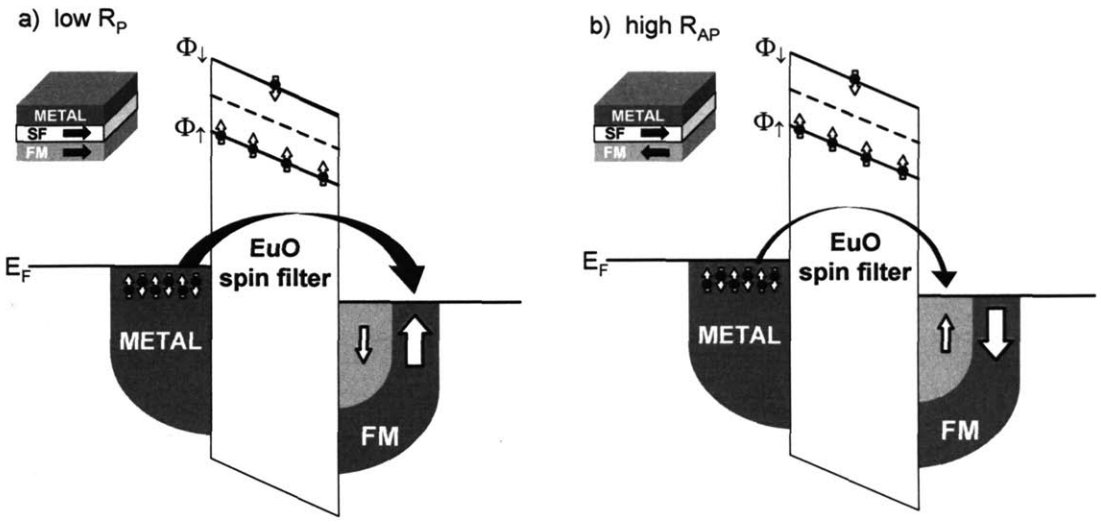

Figure 5-2: Schematic of the DOS for a metal/EuO/FM tunnel junction. The metal has an unpolarized DOS, and EuO filters the spins of the tunneling electrons. Low resistance (R_P) results when EuO and the FM are magnetized parallel (a), and high resistance (R_{AP}) results when they are aligned anti-parallel (b).

This approach has been used to illustrate spin filtering in other magnetic barriers (see references in Table 1 and Ref. 98). This chapter details the investigation of two MTJ structures with EuO spin filter barriers.

5.1 EuO barrier and Gd electrode: Large TMR

The first spin-filter MTJ structure studied was Cr/Cu/EuO/Gd (layers listed in the order deposited), in which a thin layer of Cr was a seed layer for the bottom Cu electrode and Gd was the ferromagnetic spin detector. Gd was selected as the ferromagnetic electrode primarily because the M(H) behavior for an EuO/Gd bilayer revealed that these two FMs switch at separate fields (discussed later), even though they are in contact with each other, as opposed to an EuO/Co bilayer that switches sharply at one coercive field. Furthermore, Gd is a low work function FM and thus can be used to reduce the Schottky barrier height at the FM/insulator/semiconductor interface in devices for spin-injection into a semiconductor [99].

LeClair *et al.* [100] measured high TMR>100% in Al/EuS/Gd MTJs at $T<T_C$ of EuS (=16 K), shown in Figure 5-3, which was the first display of TMR in a spin-filter MTJ. However, as seen in their magnetoresistance curve, the parallel and anti-parallel alignment states (low R_P and high R_{AP}, respectively) of the EuS and Gd were not stable, which was

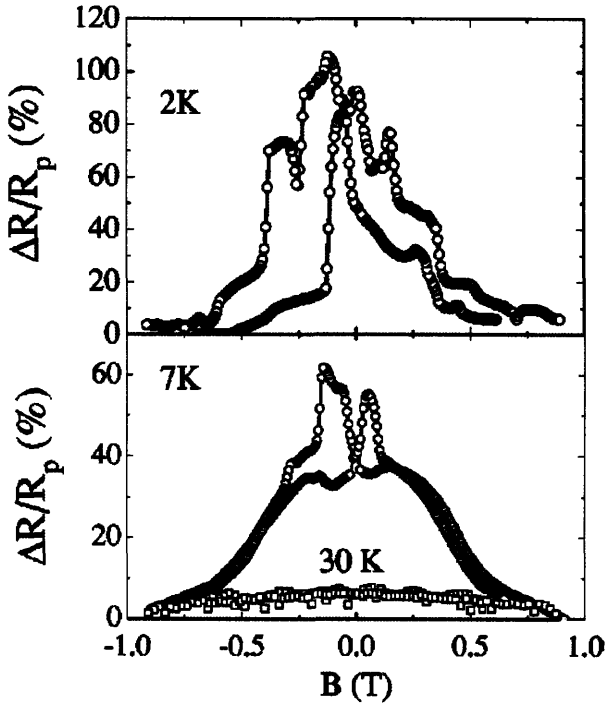

Figure 5-3: TMR for an Al/5 nm EuS/Gd tunnel junction of LeClair *et al.*, showing high TMR >100% at temperatures below the T_C of EuS. Figure from Ref. 100.

attributed to instabilities of the EuS magnetization. Later, anti-ferromagnetic coupling of EuS and Gd was shown in the PhD. thesis work of Coen Smits [101], and likely explains why this result was irreproducible in other junctions. Nevertheless, their study demonstrated the high TMR value that can be expected from a spin-filter MTJ with efficient spin filtering in the tunnel barrier.

In this study TMR was measured for a 1nm Cr/5 nm Cu/7.5 nm EuO/12 nm Gd/14 nm Al junction at low temperature with a small applied bias, shown in Figure 5-4. High TMR=280% was measured for this junction, indicating high spin-filter efficiency in EuO. The low resistance state corresponds to parallel alignment of EuO and Gd, and the high resistance state corresponds to anti-parallel alignment, as indicated by the arrows in the figure. This is the highest TMR value measured to date in a MTJ with a spin filter tunnel barrier. Applying Jullière's formula (Equation 5.1) with the optimistic assumption that the EuO spin filter efficiency is 100%, P of Gd (P_{Gd}) comes out as 58%. This P_{Gd} is higher than the 14% directly measured by Meservey *et al.* using the Meservey-Tedrow technique [17]. Given that Gd is a rare earth metal that also reacts readily with oxygen, it is probable that a higher value for Gd would be obtained if the Meservey-Tedrow measurement was

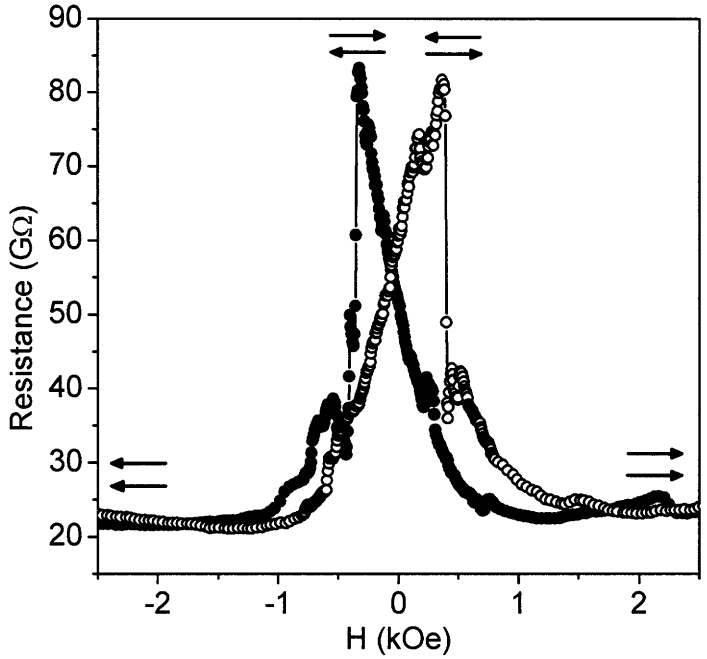

Figure 5-4: TMR=280% for a 1 nm Cr/5 nm Cu/7.5 nm EuO/12 nm Gd/14 nm Al junction, measured at 8 K with V = 40 mV. The closed circles are the measurement during decreasing H and the open circles are for increasing H.

repeated using cleaner, ultra-high vacuum conditions for sample preparation. LeClair *et al.* also deduced a high value for P_{Gd} from their TMR measurement.

The abrupt transition from the high resistance state to low resistance (Figure 5-4) is due to the abrupt magnetization reversal of EuO at its coercive field, whereas the more gradual transition at a lower field corresponds to the gradual switching of Gd. This is in agreement with the M(H) loop measured for comparison using the SQUID magnetometer with an identical multi-layer stack sample, shown in Figure 5-5. The M(H) loop in Figure 5-5a also displays the abrupt switching behavior that is typical of EuO and the more gradual switching behavior of Gd, which reaches saturation at a higher field. This M(H) loop is replotted in Figure 5-5b along with the minor loop (open circles) for the same sample. This minor loop reveals the magnetic behavior of the EuO layer, showing the coercivity and magnetization of the EuO, relative to the Gd layer. As observed from the TMR curve (Figure 5-4) and the M(H) loop, Gd has a small remanent magnetization and begins its gradual magnetization reserval before the abrupt reversal of EuO, and then continues its reversal after that of EuO. Thus, EuO and Gd reach parallel alignment at sufficiently high field, but they do not reach complete anti-parallel alignment. This is evident in the TMR curve because the anti-parallel resistance state has a peak shape, rather than a plateau, also

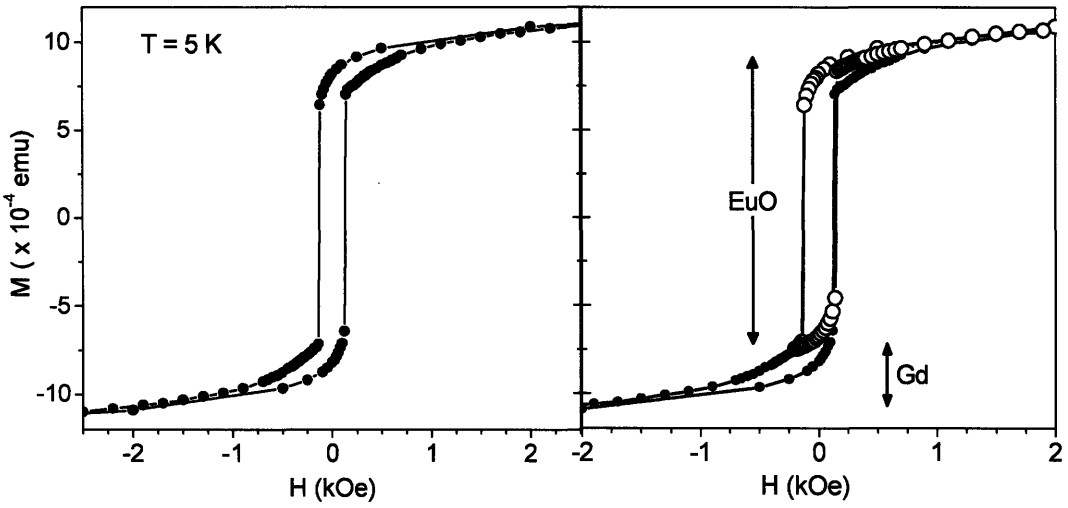

Figure 5-5: M(H) at 5K for a 1 nm Cr/5 nm Cu/7.5 nm EuO/12 nm Gd/14 nm Al structure. a) Full M(H) loop for the structure. EuO sharply switches at $\pm$130 Oe, and Gd continues to gradually switch at higher H. b) Full M(H) loop (closed circles) same as (a)) overlayed with the minor loop (open circles), showing the magnetic behavior of EuO.

showing partial magnetic coupling of the two layers. As mentioned earlier in this chapter, it is ideal for the two ferromagnets be magnetically uncoupled, so that complete anti-parallel alignment can be reached. It is likely that if the magnetizations of EuO and Gd were to switch independently of each other, even higher TMR would be observed.

High TMR was observed in only a couple junctions, among the 6 junctions with EuO and Gd measured in all, due to limited time with the high resistance measurement setup.[1] Furthermore, a well-defined TMR curve was not measured for a wide range of applied bias, due to unstable resistance values as the field was swept. This was likely caused by exchange coupling of EuO and Gd, similar to the EuS/Gd junctions of LeClair *et al.*, which is probable for any FMs in direct contact with each other. Another factor to consider is the formation of Gd_2O_3 at the EuO/Gd interface,[2] which is an anti-ferromagnet at tempertatures less than $\sim$4 K [102]. The magnetic coupling behavior at the interface is under investigation using the polarized neutron reflectivity technique (PNR), in collaboration with Dr. Shannon Watson and Dr. Julie Borchers at the National Institute of Standards and Technology in

[1]The junction resistance rose by several orders of magnitude upon cooling, starting at 3 kΩ at room temperature and rising to several GΩ at low temperature (Figure 5-4). Though countless junctions were made with thinner EuO on a Cu electrode to reduce the resistance, they were all shorted. Thus a thick 7.5 nm barrier was measured here.

[2]Gd_2O_3 has a high ΔH_f = -1825 kJ/mol [79].

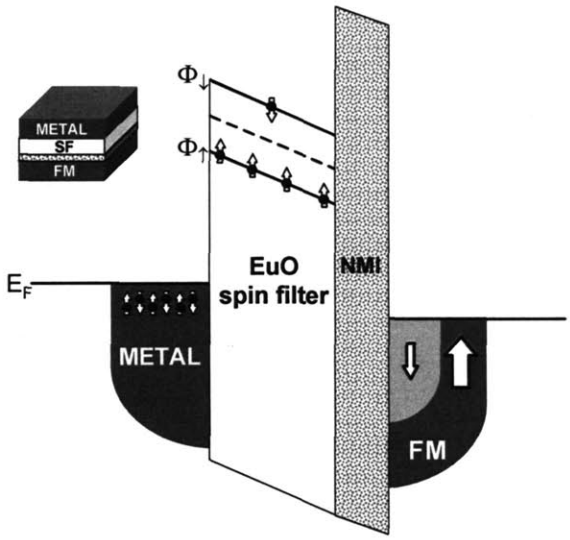

Figure 5-6: Schematic of a spin-filter MTJ with additional non-magnetic barrier, to magnetically separate EuO and the FM.

Gaithersburg, Maryland. PNR can determine the relative directions of magnetization for various buried layers in a multi-layer film sample, though these results are not yet available at the time of this thesis preparation.

Despite the complications with the Cu/EuO/Gd structure, the high TMR value manifested the high spin-filter efficiency of EuO. In an effort to avoid the complications with the Cu/EuO/Gd structure (i.e., exchange coupling, Gd_2O_3 formation, high, unstable resistance, uncertain P_{Gd}), an alternative MTJ stucture was investigated, whereby a thin, non-magnetic spacer layer was inserted between the EuO barrier and a Co spin detector, as described in the next section.

5.2 EuO barrier and Co electrode: Negative TMR

The second MTJ structure investigated was CoO/Co/Al_2O_3/EuO/Y/Al (layers listed in the order deposited). The Al_2O_3 layer was formed by depositing Al metal onto a liquid-nitrogen cooled substrate, and then oxidizing with an oxygen plasma after warming back up to room temperature. The Al_2O_3 was needed to magnetically decouple the Co and EuO ferromagnets. Otherwise, if the Co and EuO layers were in direct contact with each other, their magnetizations would switch together, yielding no TMR. The Al_2O_3 layer was an additional tunnel barrier, so it had to have the minimum thickness necessary to sufficiently

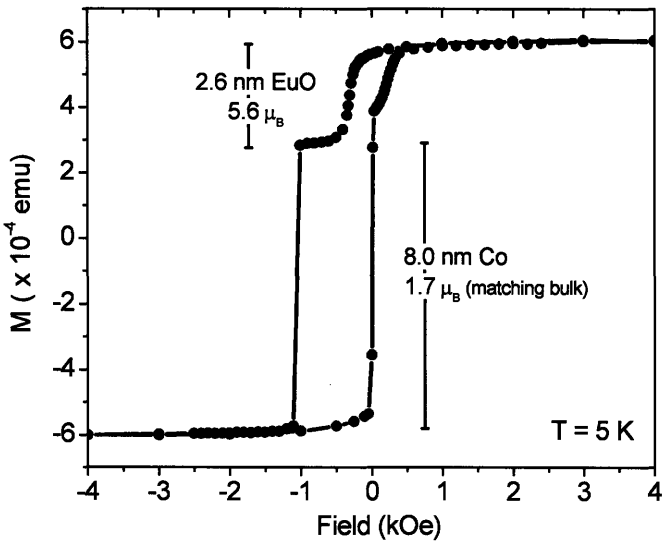

Figure 5-7: M(H) for a 1 nm CoO/8 nm Co/1 nm Al_2O_3/2.6 nm EuO/3.5 nm Y/12 nm Al film stack at 5 K. Separate switching of EuO and Co is clearly observed, with a region of anti-parallel alignment centered at ~-700 Oe. This M(H) agrees with the shape of the TMR curve in Fig. 5-8.

decouple the Co and EuO, and yet keep the junction resistance low. This structure is shown schematically in Figure 5-6.

Thin CoO was formed by depositing Co metal and then oxidizing with an oxygen plasma. CoO is an anti-ferromagnet (T_N=293 K), which can pin the magnetization direction of a FM by an intefacial effect called exchange bias [103]. This exchange-biased Co layer has a coercivity that is far removed from that of EuO, so that near complete anti-parallel alignment of EuO and Co is reached. The junctions were cooled from room temperature in a magnetic field H=3000 Oe, in order to set the CoO/Co exchange bias, which effectively shifted the M(H) loop of Co to -H values. The M(H) loop for a 1 nm CoO/8 nm Co/1 nm Al_2O_3/2.6 nm EuO/3.5 nm Y/12 nm Al film stack (identical to the MTJ structure) is displayed in Figure 5-7, showing clearly the shifted M(H) of Co due to the CoO pinning layer. The M(H) behavior of the 2.6 nm EuO is clearly distinguished from Co. M_S of EuO is high, yet reduced from the values in Figure 3-9, which is expected because EuO is grown on an oxide layer. The moment of the Co layer exactly matches that of bulk Co. There is a clear range of field in which the EuO and Co layers are aligned anti-parallel, centered at -700 Oe.

The M(H) behavior is in excellent agreement with the TMR measurements, shown in Figure 5-8 for a 1 nm CoO/8 nm Co/1 nm Al_2O_3/2.6 nm EuO/3.5 nm Y/12 nm Al junction. Figure 5-8a shows the change in R_J when the field is swept through a small range so that only the magnetization of the EuO barrier reverses and the Co layer remains pinned in the

same direction, as indicated by the arrows in the figure. At T=4.2 K and a bias of 5 mV applied relative to the Co electrode, TMR= -18%. The TMR measurement when the field is swept through a larger range, so that the Co layer also reverses, is shown in Figure 5-8b. The changes in resistance corresponding to the coercive fields of both Co and EuO are labeled for clarity, and TMR= -15% with V=20 mV. In contrast to the Cu/EuO/Gd junctions described in the previous section, a well-defined anti-parallel resistance state is observed in the TMR curve, and consisent, reproducible TMR was observed for every $CoO/Co/Al_2O_3/EuO/Y$ junction measured.

Contrary to expectation, surprisingly R_J versus H shows 'inverse' magnetoresistance, i.e., *negative* TMR, meaning that the resistance is higher in the parallel state (refer to Equation 5.1), which is not commonly observed in MTJs. Previous observations of negative TMR in MTJs, such as in epitaxial $LSMO/SrTiO_3$ or TiO_2/Co junctions [104, 105], are attributed to the dominant tunneling of the negatively polarized *d*-band electrons at the Fermi level in Co. However, this is in contrast to junctions with a Co/amorphous-$SrTiO_3$ interface [106] or a Co/Al_2O_3 interface [19], which consistently showed positive TMR.[3] The positive TMR for Co with Al_2O_3 tunnel barriers is thought to arise from the itinerant, positively-polarized *sp* electrons that dominate spin transport, rather than the localized *d* electrons [107–109]. In any case, the sign of the polarization depends on the bonding character of the FM/insulator interface.

The origin of the negative TMR in this study is not well understood at this time. Negative TMR is especially unexpected in this case because spin-filter MTJs with a similar structure—$Al/EuS/Al_2O_3/Co/CoO$—utilizing EuS barriers show *positive* TMR [96]. One can speculate that the origin lies at the Co/Al_2O_3 interface, rather than a reversal of spin-filter polarization in the EuO. It may be possible that the reactive nature of the EuO causes a different bonding configuration between the Co and Al_2O_3 compared to what is typically seen in MTJ structures of $Co/Al_2O_3/FM$ [110, 111]. The negative TMR presents a complication when trying to use Jullière's formula to determine the spin-filter efficiency of the EuO barrier, because the value of P_{Co} is in question. P_{Co} for a Co/Al_2O_3 interface is known to be in the range of +40 to 45% [9], but this does not appear to apply in the case of these spin-filter MTJs.

The bias dependence of TMR is shown in Figure 5-9, for both positive and negative voltage applied relative to the Co electrode. The bias dependence was measured by measuring the TMR at every applied bias indicated on the curve, and was also confirmed by calculating TMR from the I-V curves collected for both the parallel and anti-parallel resistance states:

[3]Positive TMR is consisently observed in $Co/Al_2O_3/FM$ junctions (FM=Ni, Fe, NiFe, CoFe) fabricated in the FBML, even when Al is over-oxidized such that a layer of CoO is formed at the Co/Al_2O_3 interface.

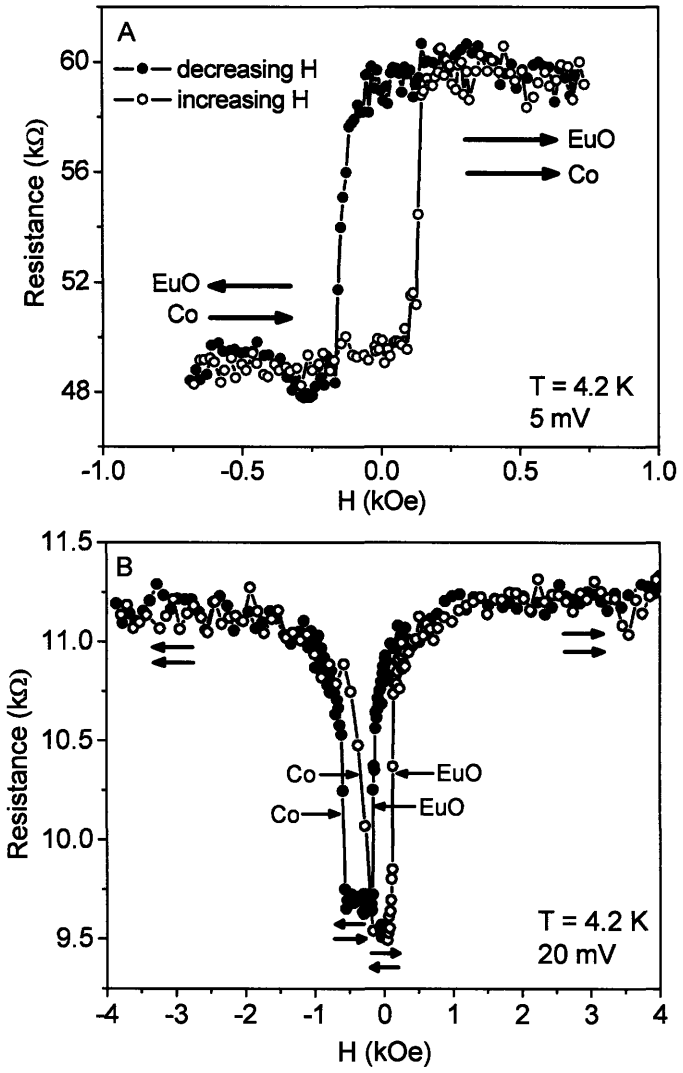

Figure 5-8: *Inverse* TMR=-18% of a 1 nm CoO/8 nm Co/1 nm Al_2O_3/2.6 nm EuO/3.5 nm Y/12 nm Al junction at 4.2K. a) 5mV bias; the field was swept between ±700 Oe, so that only the EuO layer switches at ~ ±200 Oe and the Co layer remains pinned by the CoO. R_J is higher for parallel alignment of Co and EuO and lower for anti-parallel alignment, giving rise to negative TMR. b) 20mV bias; the field was swept between ±4kOe, so that both the EuO and Co layers switch, which is labeled for clarity.

TMR=$\Delta I/I=(I_P-I_{AP})/I_{AP}$ for every V. The highest value of TMR observed was -25% for -5 mV bias. A decrease in TMR with increasing V is the typical behavior for even the best

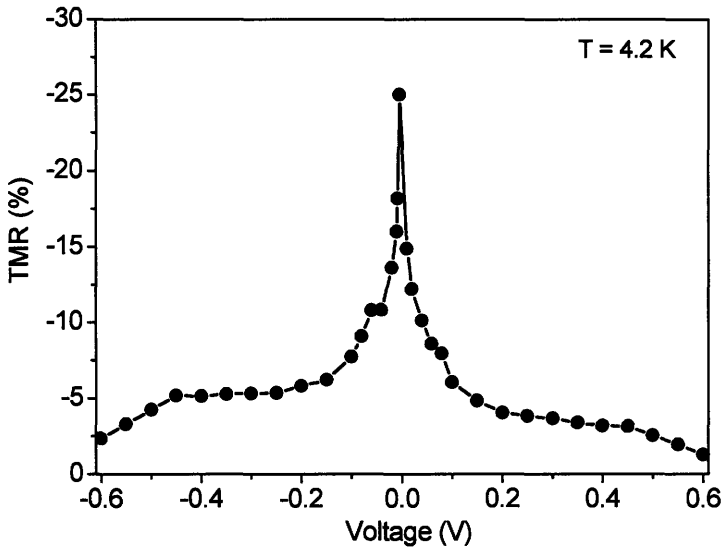

Figure 5-9: Bias dependence of TMR for a 1 nm CoO/8 nm Co/1 nm Al_2O_3/2.6 nm EuO/3.5 nm Y/12 nm Al junction at 4.2K, with voltage defined relative to the Co electrode.

quality MTJs, and is attributed to the excitation of magnons[4], phonons, and band effects at higher voltages [112–114]. However, the decrease in TMR at very low bias is particularly steep, from -25% at -5 mV down to -16% at -10 mV, which indicates the presence of defects that dominate spin transport at very low bias, at which the formerly mentioned effects are negligible. These defect states provide a spin-independent conduction path through the tunnel barrier, thus raising the total conductance and suppressing TMR. Furthermore, these defect states, likely created by non-stoichiometry and structural defects, act as sites for spin-flip scattering, which also suppresses TMR. Such a phenomenon was observed in MTJs with amorphous, semiconducting Si and Ge tunnel barriers [32, 33], previously mentioned at the end of Section 1.2. The bias dependence is not as steep at higher bias, and TMR of a few percent persists out to several hundred millivolts. Higher V could not be measured because R_J was approaching the lead resistance.

Junction resistance versus temperature at different applied voltages was also measured for these MTJs, shown in Figure 5-10, and the trend is similar to that in Figure 4-6. A large drop in R_J is observed below the T_C of EuO, and the magnitude of the drop increases with V up to 300 mV, and then is smaller for V=600 mV. However, in contrast to the junction in Figure 4-6, R_J of this MTJ is overall lower, thus allowing measurement of $R_J(T)$ at lower bias, down to 10 mV. Evidence of low-level, defect states in the barrier just above the Fermi

[4]Magnons are spin one quasiparticles, so that the excitation of a magnon in the collision with an electron flips the electron spin. This takes place at the FM/barrier interface. The probability of electron-magnon scattering increases with increasing bias.

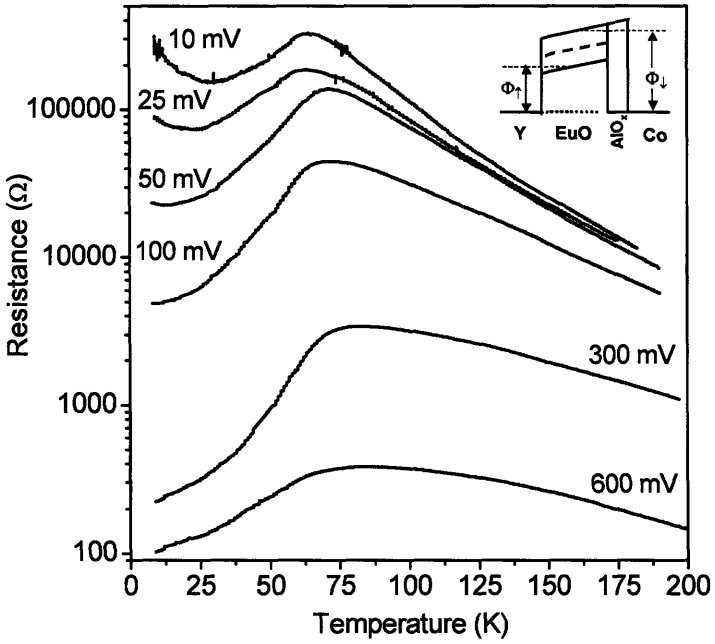

Figure 5-10: R_J for 1 nm CoO/8 nm Co/1 nm Al_2O_3/2.6 nm EuO/3.5 nm Y/12 nm Al measured at the different bias voltage indicated. A large decrease in R_J is observed below the T_C of EuO, as is characteristic of a junction with a spin-filter barrier. The inset is a schematic of low-level, defect states inside the tunnel barrier just above the Fermi level, which could give rise to the increase in R_J observed at low T for small bias V≤50 mV and the steep bias dependence of TMR.

level (shown schematically in the inset of Figure 5-10) is seen in the 10 mV curve, in which R_J rises again at lower T, after the decrease due to spin filtering. As the bias is raised, this rise in R_J at low T disappears, indicating that the small current channel provided by these low-level, defect states no longer dominates transport at higher bias. Evidence of defect states in this measurement of R_J(T) as a function of bias is consistent with the steep drop in the bias dependence of TMR at low bias (Figure 5-9). It is probable that a similar R_J(T) behavior would be observed for the junction in Figure 4-6 at low bias <100 mV, if R_J(T) was not too high to measure; the smaller decrease in R_J at lower bias (recall Figure 4-8) indicates that this is likely the case.

Regardless of the presence of defect states in the EuO barrier or the unknown origin of the negative TMR, the substantial TMR observed in this MTJ is clear evidence of spin-filtering in the EuO barrier.

Chapter 6

Conclusions

The following section reviews the major results and conclusions of this thesis project, by describing the impact of this work on the fields of magnetism, spin-polarized tunneling, and spintronics. Then a brief description of how an EuO spin filter can be used to inject polarized spins into a semiconductor is given. The last section proposes some ideas for future studies of EuO, which address the open questions that were raised by the results of this project.

6.1 Significance of this Thesis

The goal of this work was to explore the spin filtering properties of a magnetic semiconductor tunnel barrier. At the start of the project, with its large spin-splitting of the conduction band, EuO was poised to enter the field of spintronics as a material that could generate a 100% spin-polarized current. However, using EuO as a spin filter required growth of a continuous, stoichiometric EuO film just 1–3 nm thick. Due to the reactive nature of the compound, the level of control needed was down to the last atomic layer.

In this study high-quality, ultra-thin films of EuO were prepared for the first time, allowing the chacterization of this Heisenberg ferromagnet on a new scale. This fundamental study in magnetic materials substantially complements the large body of earlier work for bulk EuO. Stuctural, optical, and magnetic characterization of the films revealed a rocksalt crystal structure, an optical band gap of 1.1 eV, and a saturation magnetic moment 7 μ_B, matching that of bulk EuO. In agreement with theoretical prediction, the T_C is reduced from the bulk value of 69 K as the film thickness approaches the monolayer level, reaching 30 K for a 1 nm film. With the goal of determining the spin-filter efficiency of EuO as a barrier for spin-polarized tunneling, a phenomenon that is extremely sensitive to defects in the barrier and interfaces, careful selection of interface materials was found to be of critical importance. Through collaboration with another group at Montana State University and the facilities at

the national labs, chemical and magnetic characterization of the films and interfaces led to the optimization of tunneling structures that produced high spin-filter efficiency.

The amount of exchange splitting of the conduction band in ultra-thin films of EuO was quantitatively determined for the first time, in a tunneling experiment. To achieve this, temperature and bias dependence of junction resistance was studied below T_C, where the development of exchange splitting was followed and applied to tunneling theory. The uniqueness of this particular study was that EuO was seen to filter spins at finite bias, which is relevant for operating a spin-injection device.

The spin-polarized tunnel current generated by the EuO spin filter was quantitatively probed by two methods—using the Zeeman-split density of states of a superconductor as the spin detector, and by using a ferromagnet as the spin detector in a magnetic tunnel junction structure. Both methods were used in a non-conventional manner, in order to determine the spin polarization created by a ferromagnetic barrier, rather than by a ferromagnetic electrode. Because of the sensitivity of these techniques to barrier and interface quality, spin-polarized tunneling measurement was the ideal approach to assess the EuO film quality.

Direct measurement of spin polarization of the tunnel current from an unpolarized metal source through the EuO barrier gave a substantial value of ~30%. The higher value of polarization observed using a Y electrode compared with a Ag electrode was correlated with the interfacial chemical analysis by x-ray absorption spectroscopy, which showed that Eu_2O_3 was present in the EuO film capped with Ag, whereas the presence of Eu_2O_3 in the film capped with Y was minimal. Because these junctions did not have ferromagnetic electrodes, these experiments confirmed that spin-filtering in the EuO did indeed produce the spin-polarized current. Moreover, a superconductor/ferromagnetic insulator proximity effect was clearly observed in these junctions as well. Evidence of the strong exchange interaction of the ferromagnetically aligned Eu^{2+} ions at the interface with the superconductor, showed the good quality of the EuO and its interface with Al.

In a magnetic tunnel junction, tunnel magnetoresistance due to the relative change in orientation of the magnetizations of the EuO barrier and a ferromagnetic electrode, also showed that EuO produced a spin-polarized current. TMR of 280% was measured for Cu/EuO/Gd junctions, which is the largest TMR value measured in a magnetic tunnel junction using a spin filter barrier. To eliminate the exchange coupling of the EuO and Gd, another junction structure was investigated (CoO/Co/Al_2O_3/EuO/Y) in which a non-magnetic, insulating Al_2O_3 separated the EuO and Co ferromagnets. Inverse TMR up to -25% was consistently observed for this structure. The origin of the negative TMR is still an open question. Nevertheless, observation of TMR in both of these magnetic tunnel junction structures also clearly demonstrated spin filter properties of EuO.

Due to its simple crystal structure, negligible magnetic anisotropy, and large exchange splitting, EuO was a model system with which to study spin-filter tunneling phenomena (once the art of making high quality films was achieved). In addition, because the T_C of EuO is in the liquid helium and nitrogen temperature range, around which the temperature can be easily varied, exchange splitting of the barrier, which gives rise to spin filtering, could be carefully followed and determined quantitatively.

Spin-filter tunneling is gaining interest, especially with the possibility of filtering spins at room temperature using more complex, oxide spin filters. Furthermore, it may be possible to use a spin-filter barrier to efficiently inject a highly polarized current into a semiconductor, as will be described briefly in the next section. To the benefit of these efforts, this body of work demonstrates the properties of EuO thin films and spin-filter tunneling phenomena, and thus can be used as guide for future studies with other materials and structures.

6.2 Using a Spin Filter for Spin Injection

As mentioned in Chapter 1, using a spin-filter tunnel barrier to generate and inject a highly spin-polarized current is one of the most promising approaches to spin-injection. This section provides a brief glimpse of what may be possible when combining a semiconductor device and a spin filter.

Sugahara and Tanaka [115] recently proposed a spin-filter transistor (SFT) wherein a spin-polarized current is injected into a non-magnetic base by tunneling through a spin filter barrier, shown schematically in Figure 6-1. Their proposed SFT provides the theoretical basis for a spin-injection device utilizing an EuO spin filter as the source of spin-polarized electrons. The emitter, base and collector are non-magnetic, conductive materials. The emitter barrier filters the spins as they tunnel from the emitter into the base when an emitter-base bias is applied, allowing only spin-up electrons into the base, and the collector barrier acts as a spin-analyzer for the spin polarized transport through the base. The width of the base L must be less than the mean-free-path for spin-flip scattering. When the EuO barriers are magnetized parallel to each other, as in Figure 6-1a, the spin-up electrons injected into the base can tunnel through the collector barrier (lower barrier height for spin-up electrons), and a collector current will be detected. When the EuO barriers are magnetized in an antiparallel configuration, as in Figure 6-1b, the spin-up electrons injected into the base cannot tunnel across the collector barrier; the spin-up barrier height is too high, and hardly any collector current will be detected. In this way, the spin filter is also used as the spin detector. Thus, the output characteristics of the SFT depends on the magnetization configuration of the

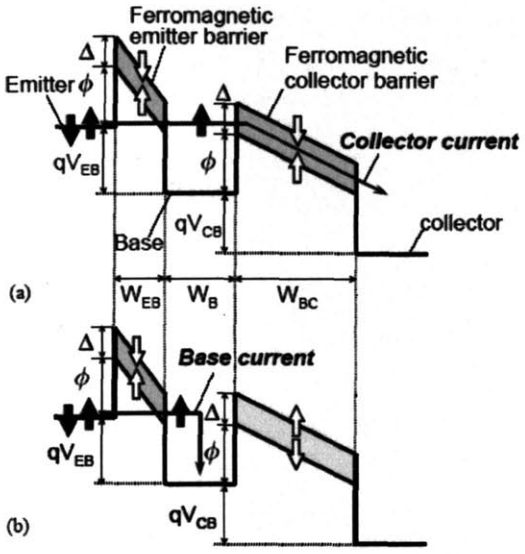

Figure 6-1: Schematic of the spin-filter transistor proposed by Sugahara and Tanaka. a) Parallel magnetic orientation of the emitter barrier and collector barrier, resulting in a high collector current. b) Antiparallel magnetic orientation, resulting in no collector current. Figure adapted from Ref. 115.

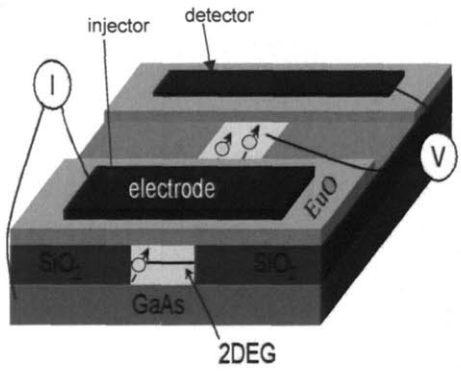

Figure 6-2: Basic structure of a spin injection device utilizing two EuO tunnel barriers, one for injection and the other for detection of the spin-polarized current. The contacts for measurement utilize a non-local geometry, similar to that employed by Jedema *et al.* [116].

emitter and collector tunnel barriers—the collector current for parallel configuration will be significantly higher than the collector current for antiparallel configuration.

A schematic of a lateral, spin transport device is shown in Figure 6-2. Transport of the injected spins in the semiconductor is confined to a channel, depicted in the figure

as a 2-dimensional electron gas (2DEG) in GaAs. The device is designed for non-local measurement, such that there is no *charge* current, only *spin* current, between the injection and detection terminals. The spins are injected into the 2DEG channel across the injector spin-filter junction, and voltage is read across the detector spin-filter junction. The injected spin current causes an imbalance of the electrochemical potentials for spin-up and spin-down electrons in the semiconductor channel. This imbalance is transported by diffusion in the channel to the detector. Thus, the spacing between the injector and detector along the channel must be smaller than the spin-coherence length. The effectiveness of this device design has been well demonstrated for spin-injection into non-magnetic metals [116, 117]. This is the only measurement geometry thus far yielding an unambiguous spin signal, free from spurious effects such as magnetoresistance of the component layers, local Hall effects, or anisotropic magnetoresistance.

The device in Figure 6-2 is not a transistor, because it does not have a gate terminal. However, demonstrating spin-injection, transport and detection in such a device is a major step toward realizing a spin field effect transistor (spin-FET), and has recently been accomplished by Lou *et al.* in GaAs at low temperature using a FM/semiconductor Schottky tunnel barrier (not a spin filter) [118]. They also successfully demonstrated the Hanle effect, which is the suppression of the detected signal by applying a transverse, applied magnetic field that induces spin precession and dephasing during transport in the channel. The gate in an actual spin-FET would function by allowing the spin current to flow in the channel or not. The voltage on the gate would create an effective, transverse magnetic field via the spin-orbit interaction in the semiconductor material, such that the spin precession induced, leading to parallel or antiparallel (or anything in between) alignment of the spins with the drain, is controlled by the gate voltage. Such a spin-FET was first proposed in 1990 by Datta and Das [119]. The EuO spin filter could be incorporated into the spin-FET as the source of highly polarized spins at the injector and as the spin-dependent tunnel barrier at the dectector—referred to as a SFT above. Because EuO is chemically compatible and has a matching band gap with silicon, and due to a recent, promising demonstration of spin-injection into silicon [120], one can envision a SFT using Si-based semiconductors as well.

6.3 Topics for Future Studies of EuO

As described in the previous section, an application of the EuO spin filter involves incorporating EuO into a spin transport device. Such an application is an ongoing research effort of the advisor's group in the FBML that will continue beyond this thesis work.

There is also interest in more fundamental studies of the EuO tunnel structures, that has arisen to address the open questions posed by the results of this thesis work. One such open question is the origin of the unexpected, negative TMR in the $Co/Al_2O_3/EuO/Y$ tunnel junction, described in Section 5.2. There are no tools that can single out and investigate the bonding that is occurring just within one monolayer at the interface between the materials in this structure, in order to pinpoint how the interface is controlling the sign of the polarization. Input from theorists, that could investigate how the bonding configuration at the interface gives rise to negative polarization, would be valuable in this effort. It would be interesting to replace Co in this junction structure with either Fe or permalloy, to try to measure higher, positive TMR, since Fe and permalloy would be expected to have P>+40% in such a structure.

Another fundamental study would be to investigate the spin structure at the EuO/Gd interface, using polarized neutron reflectivity. In the Cu/EuO/Gd junction structure, high TMR is observed, as described in Section 5.1, yet there is coupling of the EuO and Gd. PNR can distinguish the film magnetization relative to the applied field for various materials in the film stack. PNR analysis of EuO/Gd as a function of Gd thickness could reveal the spin structure at the interface relative to the bulk; for example, it could reveal if the EuO and Gd spins are coupled at the interface, and then the Gd spins are canted to form a spiral configuration through the bulk of the film, giving rise to the gradual switching behavior and lower moment that is observed for Gd in this study (Figure 5-5). Preliminary PNR measurements do indicate that for part of the film, some projection of the Gd moment is perpendicular to the applied field, signifying a canted spin configuration.

Appendix A

Room-Temperature TMR and Spin Polarized Tunneling Studies with an Organic Semiconductor Barrier

Abstract

Electron spin polarized tunneling is observed through an ultra-thin layer of the molecular organic semiconductor tris(8-hydroxyquinolinato)aluminum (Alq_3). Significant tunnel magnetoresistance (TMR) was measured in a $Co/Al_2O_3/Alq_3/NiFe$ magnetic tunnel junction at room temperature, which increased when cooled to low temperatures. Tunneling characteristics, such as the current-voltage behavior and temperature and bias dependence of the TMR, show the good quality of the organic tunnel barrier. Spin polarization of the tunnel current through the Alq_3 layer directly measured using superconducting Al as the spin detector, shows that minimizing formation of an interfacial dipole layer between the metal electrode and organic barrier significantly improves spin transport.

Introduction

There is considerable activity of late in the field of organic electronics both from the fundamental physics point of view as well as with the promise of developing cheaper and flexible devices, such as organic light emitting diodes (OLEDs) and organic transistors [121]. While these materials are exploited for their tunability of charge-carrier transport properties, their *spin* transport properties is a least explored area, especially for organic semiconductors (OSCs) which are pertinent for future spin-based electronics. Because OSCs are composed of mostly light elements (i.e. C, H, N, O) and thus have a weaker spin-orbit interaction compared to inorganic semiconductors, spin coherence lengths can be long in these materials. Recent observations of magnetoresistance (MR) effects in OSCs has opened up the potential of these materials for spin-conserved transport. In an organic spin valve study using Alq_3 as the spacer layer between ferromagnetic $La_{0.67}Sr_{0.33}MnO_3$ (LSMO) and Co electrodes, Xiong *et al.* [122] measured a giant inverse magnetoresistance (GMR) of 40% at 11 K, which reduced to zero by T>200 K. The thickness range of Alq_3 used in that study was from 130 nm to 260 nm, and a spin diffusion length of 45 nm was estimated at liquid helium temperatures. They also concluded that there was an ill-defined layer of ~100 nm of Alq_3 containing Co inclusions. Mermer *et al.* [123] showed room temperature MR of polyfluorene films and Alq_3 films several nanometers thick, sandwiched between *non*-ferromagnetic electrodes. Utilizing the Alq_3 molecule at the monolayer level, we demonstrate spin polarized tunneling through an OSC at room temperature and the effect of interfacial charge states on spin injection. This study opens up the possibility for many future investigations in this area, which is expected to be rich in physics as well as device potential.

The organic π-conjugated molecular semiconductor Alq_3 ($C_{27}H_{18}N_3O_3Al$), shown in Fig. A-1, is the most widely used electron transporting and light-emitting material in OLEDs. Alq_3 has been extensively studied for this application since it displayed high electroluminescence (EL) efficiency nearly two decades ago [125]. A band gap of 2.8 eV separates the highest occupied molecular orbital (HOMO) and the lowest unoccupied molecular orbital (LUMO). Typically, the film thickness of the Alq_3 layers in OLEDs and structures for MR studies is tens to hundreds of nanometers. In the present study, we have successfully fabricated Alq_3 films <2 nm thick as a tunnel barrier between two ferromagnetic electrodes. The resistance of this magnetic tunnel junction (MTJ) depends on the relative orientation of the magnetization of the two ferromagnetic electrodes; lower resistance for parallel alignment (R_P) and higher resistance for antiparallel alignment (R_{AP}) [18,19]. Tunnel magnetoresistance (TMR) is defined as $\Delta R/R = (R_{AP} - R_P)/R_P$, and has a positive value for our MTJs with Alq_3 barrier, even at room temperature. To further corroborate the positive TMR found in this

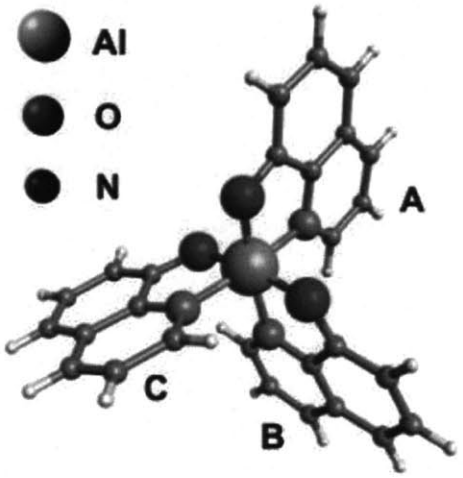

Figure A-1: Alq_3 molecule ($C_{27}H_{18}N_3O_3Al$), comprised of a central aluminum atom surrounded by three hydroxyquinoline ligands (A,B,C). The meridional isomer is shown. The molecule is clearly not planar. Figure from Ref. 124.

study, we also performed a direct measurement of the spin polarization (P) of the tunnel current from several ferromagnets through the Alq_3 barrier, by utilizing superconducting Al as the spin detector.

Tunnel Junction Preparation

Tunnel junctions were prepared *in situ* in a high vacuum deposition chamber with a base pressure of $6x10^{-8}$ Torr. The MTJs were deposited on glass substrates at room temperature having the following structure, listed in the order of deposition: 1 nm SiO/8 nm $Co/Al_2O_3/Alq_3$/10 nm $Ni_{80}Fe_{20}$. The Co and $Ni_{80}Fe_{20}$ (permalloy (Py)) ferromagnetic electrodes were patterned by shadow masks into a cross configuration. The Alq_3 tunnel barrier was grown by thermal evaporation from a Alq_3 powder source at a controlled deposition rate of ~0.3 nm/sec. Junctions with six different Alq_3 thicknesses, ranging from 1 nm to 4 nm, were prepared in a single run by using a rotating sector disk. A thin Al_2O_3 layer of ~0.6 nm at the interface between the Co electrode and the Alq_3 barrier was formed by depositing Al film and then oxidizing it by a short exposure (~2 sec) to oxygen plasma. Film thickness was monitored *in situ* by a quartz crystal oscillator, and the density of Alq_3 used was 1.5 g/cm^3 [126]. Tunnel junctions for direct spin polarization measurement were made in an identical manner having the following structure: 3.8 nm Al/Alq_3/8 nm Co or Fe or Py, with and without an ultrathin layer of Al_2O_3 at the Al/Alq_3 interface. The Al electrode was

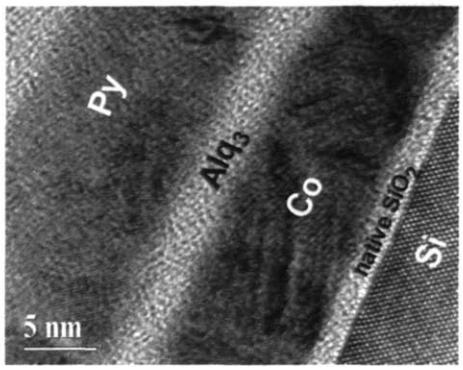

Figure A-2: HRTEM image of the Alq_3 tunnel barrier, which forms a continuous layer in this 8 nm Co/3nm Alq_3/10 nm Py structure grown on a silicon substrate with native oxide.

deposited onto liquid nitrogen cooled substrates. Alq_3 was deposited on this Al strip either at low temperature or at room temperature, yielding similar tunneling results. Half of the junctions were prepared with Co top electrode and the other half with either Fe or Py in the same run. The junction area was 200 x 200 μm^2.

Growth of the Alq_3 films was uniform and continuous, as shown in Fig. A-2 by the cross-sectional high-resolution transmission electron microscope (HRTEM) image of thin Alq_3 between Co and Py. X-ray diffraction of the Alq_3 films >50 nm thick showed the amorphous structure of the film. No change in the chemical structure of Alq_3 is expected during thermal deposition in vacuum [127], and the thickness of one continuous monolayer of Alq_3 is $\sim$1 nm [128]. Alq_3 films at the monolayer level on metal and Al_2O_3 underlayers have been well studied earlier [127–131].

Current-Voltage Characteristics

Junction resistance (R_J) was measured using a four-point probe configuration. The tunneling characteristics were measured for 4 sets of MTJs, with 72 junctions per set, and the results were consistent. In a given junction preparation run with six different Alq_3 thicknesses, R_J scaled exponentially with Alq_3 thickness (shown in the inset of Fig. A-3), which shows that tunneling is occuring through the Alq_3 layer [132]. With this exponential dependence of R_J, combined with TEM data, one can rule out the possibility that the Alq_3 deposition was discontinuous and only acted to reduce the effective junction area for tunneling through the Al_2O_3 layer. If the latter were the case, because $R_J \propto$ (junction area)$^{-1}$, the R_J dependence on Alq_3 thickness would follow the dashed line shown in Fig. A-3 inset. Upon cooling from room temperature down to 4.2 K, R_J rose by a factor of 2 to 3 (see inset of Fig. A-4). Such increase in R_J with decreasing temperature is common for junctions with semiconductor

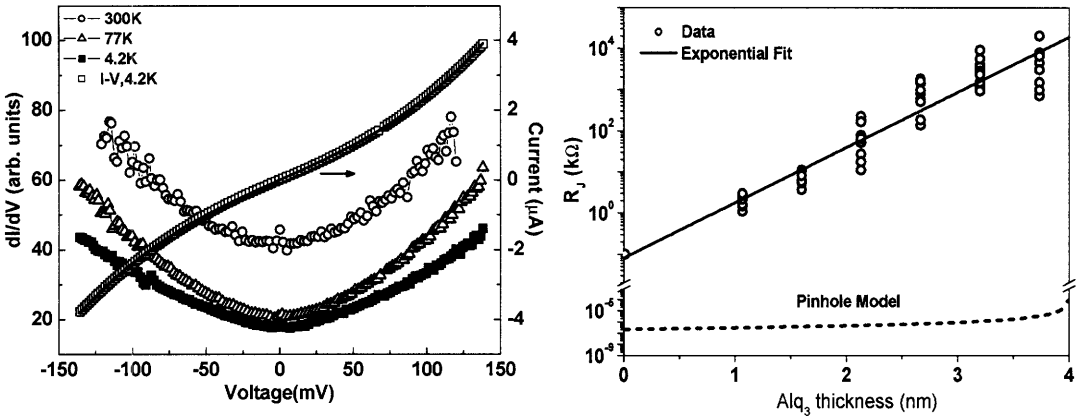

Figure A-3: Left: Current-voltage characteristics for a 8 nm Co/0.6 nm Al_2O_3/1.6 nm Alq_3/10 nm Py junction. The fit of the I-V curve to BDR's equation is also shown, yielding the following values: Φ=0.47 eV, $\Delta\Phi$=0.01 eV, s=3.3 nm. Right: Exponential dependence of R_J on Alq_3 thickness, for a total of 72 junctions made in a single run.

tunnel barriers [32, 33], as opposed to pure, insulating Al_2O_3 barriers which show a R_J increase of ~20% over the same temperature decrease.

The current-voltage (I-V) characteristics for one MTJ are shown in Fig. A-3 and are representative of all MTJs measured. The I-V curve was fit using the model of Brinkman, Dynes, and Rowell (BDR) [11], yielding values of 0.47 eV for tunnel barrier height (Φ), 0.01 eV for barrier asymmetry ($\Delta\Phi$), and 3.3 nm for barrier thickness (s). Given an uncertainty in actual barrier thickness and the large size of the Alq_3 molecule, a value of s=3.3 nm found from the fit is nominal. The Φ value of 0.47 eV is reasonable for Alq_3 which has a band gap of 2.8 eV [133]. As shown in Fig. A-3, the shape of the conductance (dI/dV) versus bias is similar at room temperature and low temperatures, only shifted down due to the higher R_J at lower temperatures. It is necessary to note the absence of a sharp dip at zero bias (known as the zero bias anomaly), especially for lower temperatures. This shows that the barrier and interfaces are free of magnetic inclusions. Presence of such a dip in conductance can be caused by diffusion of magnetic impurities into the barrier, among other possibilities [134, 135]. In the double barrier structure, with Al_2O_3 and Alq_3, the tunnel conductance versus bias at all temperatures is symmetric with no offset present, signifying a rectangular potential barrier [132]. This symmetric barrier is reasonable when considering the low barrier height for ultrathin Al_2O_3 [136] and the amorphous structure of both Al_2O_3 and Alq_3 [32, 33]. The junctions are stable up to an applied bias of $\sim \pm 150$ mV and show properties that are reproducible over time. These properties—the exponential thickness dependence of R_J, strong temperature dependence of R_J, and nonlinear I-V, along with

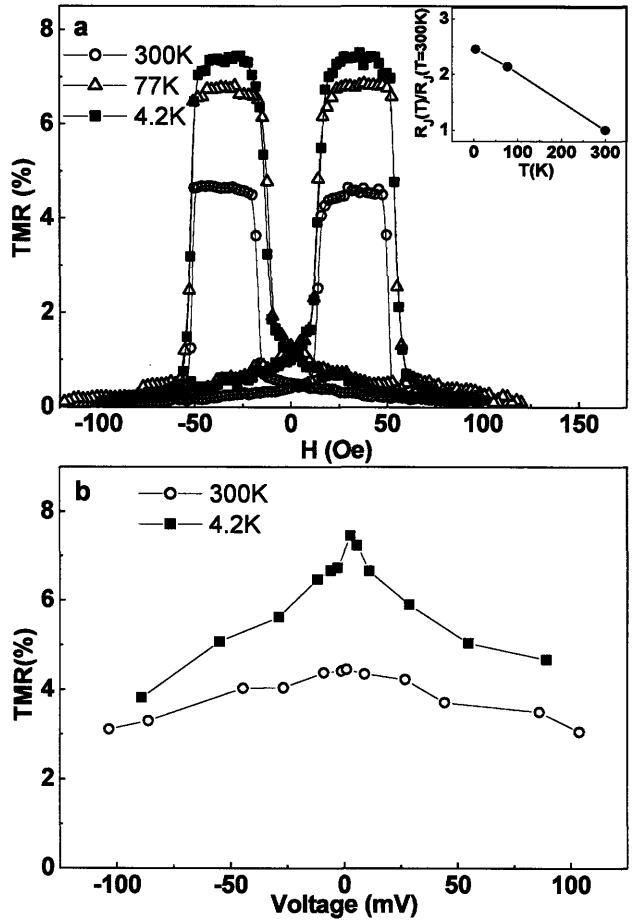

Figure A-4: TMR for a 8 nm Co/0.6 nm Al_2O_3/1.6 nm Alq_3/10 nm Py junction. a) TMR measured with 10 mV bias at 300 K, 77 K and 4.2 K. The top inset shows the temperature dependence of R_J for this junction and the chemical structure of the Alq_3 molecule. b) TMR as a function of bias at 300 K and 4.2 K.

the TEM data—confirm that tunneling is occurring through the Alq_3 layer, rather than singly through pinholes and the Al_2O_3 layer. Thus, these organic barrier MTJs show good tunneling behavior.

Tunnel Magnetoresistance

TMR for a 8 nm Co/0.6 nm Al_2O_3/1.6 nm Alq_3/10 nm Py junction measured with a 10 mV bias is shown in Fig. A-4a, with TMR values of 4.6, 6.8, and 7.8% at 300, 77, and 4.2 K, respectively. Well-separated coercivities of the Co and Py electrodes yield well-defined parallel and antiparallel magnetization alignment, clearly showing the low resistance (R_P) and high resistance (R_{AP}) states, respectively. The small increase in TMR and R_J upon

cooling from 77 K to 4.2 K is another indication of a good quality barrier [9]. Similar TMR values and temperature dependence was observed for all Alq_3 barrier junctions. The highest TMR value at room temperature seen in this study was 6.0%.

The bias dependence of the TMR for the same junction at 300 K and 4.2 K is shown in Fig. A-4b and is symmetric for $\pm$V. Substantial TMR persists even beyond $\pm$100 mV. Decrease of TMR with increasing bias voltage has been observed for even the best quality MTJs with Al_2O_3 barriers, and is attributed to the excitation of magnons, phonons, band effects, etc. at higher voltages [112–114]. In addition, for the present junctions with Alq_3 barrier, one can expect chemistry-induced states in the Alq_3 band gap [130] (discussed below) which would give rise to increased temperature and bias dependence as well as reduced TMR [9].

Direct Polarization Measurement

To directly determine the spin polarization of the tunnel current from Co, Fe, and Py electrodes through the Alq_3 barrier, junctions with an Al counter-electrode were cooled to 0.4 K in a He^3 croystat and dynamic tunnel conductance versus bias voltage was measured. Conductance (dI/dV) of a 3.8 nm Al/Al_2O_3/1.7 nm Alq_3/8 nm Co junction and a 3.7 nm Al/3.7 nm Alq_3/3 nm Co/6 nm Py junction shown in Fig. A-5a and b respectively, displays the characteristic behavior of conduction by tunneling into a superconductor [10]. The Al electrode had a superconducting transition temperature of $\sim$2.9 K. Negligible leakage at V=0 and the sharp peaks at the superconducting gap voltage, seen in the zero field conductance curves, is a confirmation of the high quality of the Alq_3 tunnel barrier without any Co inclusions.

When a magnetic field (H) is applied in the plane of the film, Zeeman splitting of the conductance peaks is observed with magnitude $2\mu_B$H. Asymmetry of the conductance, seen here, is the classic signature for spin polarization of the tunnel current [10]. To extract the polarization value, the dI/dV curve was fit with Maki's theory of the superconducting Al quasiparticle density of states in a field, taking into account orbital depairing and spin-orbit scattering [137]. For the Co electrode and Al_2O_3/Alq_3 barrier, a P value of 27% was determined from the conductance in Fig. A-5a. Similarly, P values of 30% for Fe and 38% for Py were determined. These values may be compared with 42%, 44%, and 50% obtained for Co, Fe, and Py, respectively, with a pure Al_2O_3 tunnel barrier prepared in an ultra-high vacuum chamber [9]. Though P for a Al_2O_3/Alq_3 barrier is slightly less than that obtained for pure Al_2O_3 barriers, this measurement clearly demonstrates spin polarization of the tunnel current from a ferromagnet through an OSC. However, the value of P was down to 6% for

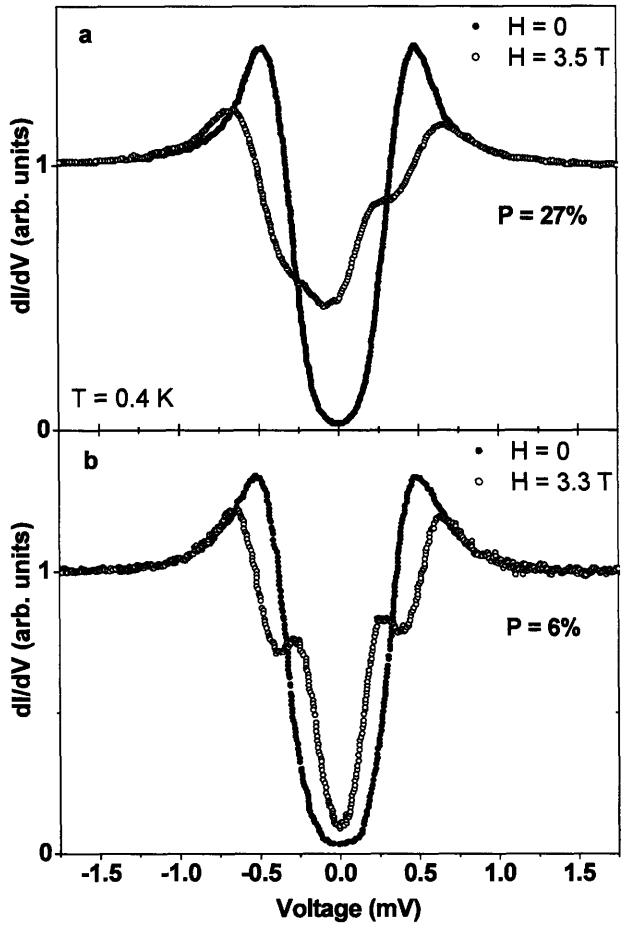

Figure A-5: Direct spin polarization measurement of the tunnel current through Alq_3 barrier. Conductance (dI/dV) of a 3.8 nm Al/Al_2O_3/1.5 nm Alq_3/8 nm Co junction (a) and a 3.7 nm Al/3.7 nm Alq_3/3 nm Co/6 nm Py junction (b) at 0.4 K, with and without an applied magnetic field. Fit to Maki's theory of the dI/dV curves in an applied field yields P=27% and P=6% for the junction with and without Al_2O_3 at the Al/Alq_3 interface, respectively.

the junction without Al_2O_3 at the Al/Alq_3 interface, as shown in Fig. A-5b. BDR fitting of the I-V curve for the junction in Fig. A-5a yielded values of Φ=0.52 eV, $\Delta\Phi \sim 0$, and s=3.1 nm, which are in good agreement with the barrier parameters of the MTJs (Fig. A-3). The corresponding parameters for the junction in Fig. A-5b were Φ=1.8 eV, $\Delta\Phi \sim 0$, and s=1.6 nm.

Discussion

For both junction structures, with and without Al_2O_3 at the Al/Alq_3 interface, we measured a positive value of P for Co, Fe, and Py electrodes, which is in agreement with the positive

TMR we measured. This is in contrast to the inverse GMR observed by Xiong *et al.* in a LSMO/Alq_3/Co spin valve [122]. This discrepancy can be attributed to the different conduction mechanisms responsible for the GMR and TMR effects [138]. Contrary to Xiong *et al.*'s speculation based on tunneling that their inverse GMR is due to the negative spin polarization of the Co *d*-band at the Fermi level, inverse GMR may originate from the opposite spin asymmetry coefficients of Co and LSMO, as shown by Vouille *et al.* [139]. Also, the role of Co inclusions (to a depth of ~100nm in the Alq_3) on the observed inverse MR is unclear. The tunneling behavior observed in our study is similar to that of both amorphous Al_2O_3 and amorphous $SrTiO_3$ tunnel barriers [106], in which positively-polarized, itinerant *sp*-electrons dominate spin transport [107–109].

The high barrier height for the junction in Fig. A-5b can be attributed to a dipole layer formed at the metal-Alq_3 interface. Such a phenomenon has previously been observed in tunnel junctions with a layer of organic material adsorbed at the barrier interface [11, 140]. This dipole barrier is also present at the metal-organic interface in OLEDs [141, 142] and has been attributed to charge transfer, chemical reactions, and changes of molecular configuration, which introduce states into the Alq_3 band gap [130]. These intrinsic gap states are concentrated mainly at the metal-organic interface. Thus, the bulk of the Alq_3 film is a good quality tunnel barrier, producing a conductance measurement with negligible leakage current (Fig. A-5b). Yet the presence of the gap states manifest themselves in the reduced polarization value and more noise in the dI/dV measurement, compared to the junction with an Al_2O_3 interfacial layer. The charge states appear to localize the tunneling spins, thereby reducing spin-conserved tunneling [31]. It is known from OLED studies that a very thin layer (~1 nm) of Al_2O_3 at the cathode-Alq_3 interface suppresses the formation of these gap states and effectively lowers the barrier height to electron injection via tunneling across the interface, resulting in more efficient injection and enhanced EL output [129, 143]. Likewise, the ultrathin Al_2O_3 layer at the electrode-Alq_3 interface of our tunnel junctions results in significantly higher P, lower tunnel barrier height, and less noise in the dI/dV measurement (Fig. A-5a). This result demonstrates the degrading effect of interfacial charge states in spin-conserved tunneling and how minimizing formation of these states greatly improves spin injection efficiency across the ferromagnet/OSC interface. Finally, MTJs prepared with pure Alq_3 barriers up to 20nm thick without the Al_2O_3 layer were unstable and did not show good tunneling behavior, likely caused by the chemical nature of the Co/Alq interface [131], leading to multi-step conduction via these gap states.

Summary

In summary, we have observed TMR at room temperature in magnetic tunnel junctions with an organic semiconductor Alq_3 barrier. Spin polarization of the tunnel current from a ferromagnetic electrode through the organic barrier is directly measured using a superconductor as the spin detector. A much higher value of P is observed when Al_2O_3 is inserted at the Al/Alq_3 interface, than without Al_2O_3, which has been attributed to the minimized formation of intrinsic, interfacial gap states that act to suppress P. This work shows that spin-conserved transport through organic systems is possible, which can lead to the development of spin-based molecular electronics.

Bibliography

[1] J. M. Kikkawa and D. D. Awschalom. Lateral drag of spin coherence in gallium arsenide. *Nature*, 397:139–141, 1999.

[2] Mark Johnson, editor. *Magnetoelectronics.* Elsevier, 2004.

[3] D. D. Awschalom, D. Loss, and N. Samarth, editors. *Semiconductor Spintronics and Quantum Computation.* Springer, 2002.

[4] I. Žutić, J. Fabian, and S. Das Sarma. Spintronics: Fundamentals and applications. *Reviews of Modern Physics*, 76(2):323–410, 2004.

[5] M. Oestreich, M. Bender, J. Hübner, D. Hgele, W. W. Rhle, Th. Hartmann, P. J. Klar, W. Heimbrodt, M. Lampalzer, K. Volz, and W Stolz. Spin injection, spin transport and spin coherence. *Semiconductor Sci. Technol.*, 17:285–297, 2002.

[6] G. Schmidt, D. Ferrand, L. W. Molenkamp, A. T. Filip, and B. J. van Wees. Fundamental obstacle for electrical spin injection into a semiconductor heterostructure. *Physical Review B*, 62(8):R4790, 2000.

[7] E. I. Rashba. Theory of electrical spin injection: Tunnel contacts as a solution of the conductivity mismatch problem. *Physical Review B*, 62(24):R16267, 2000.

[8] A. Fert and H. Jaffrès. Conditions for efficient spin injection from a ferromagnetic metal into a semiconductor. *Physical Review B*, 64:184420, 2001.

[9] J. S. Moodera and G. Mathon. Spin-polarized tunneling in ferromagnetic junctions. *Journal of Magnetism and Magnetic Materials*, 200:248–273, 1999.

[10] R. Meservey and P. M. Tedrow. Spin-polarized electron tunneling. *Physics Reports*, 238(4):173–243, 1994.

[11] W. F. Brinkman, R. C. Dynes, and J. M. Rowell. Tunneling conductance of asymmetrical barriers. *Journal of Applied Physics*, 41(5):1915–1921, 1970.

[12] Walter A. Harrison. Tunneling from an independent-particle point of view. *Physical Review*, 123(1):85–89, 1961.

[13] I. Giaever. Energy gap in superconductors measured by elecgtron tunneling. *Physical Review Letters*, 5:147, 1960.

[14] I. Giaever. Electron tunneling between two superconductors. *Physical Review Letters*, 5:464, 1960.

[15] R. Meservey and P. M. Tedrow. Spin-dependent tunneling in ferromagnetic nickel. *Physical Review Letters*, 26(4):192–195, 1971.

[16] P. M. Tedrow and R. Meservey. Spin polarization of electrons tunneling from films of Fe, Co, Ni, and Gd. *Physical Review B*, 7(1):318–326, 1973.

[17] R. Meservey, D. Paraskevopoulos, and P. M. Tedrow. Tunneling measurements of conduction-electron-spin polarization in heavy rare-earth metals. *Physical Review B*, 22(3):1331–1337, 1980.

[18] M. Julliere. Tunneling between ferromagnetic films. *Physics Letters*, 54A(3):225–226, 1975.

[19] J. S. Moodera, L. R. Kinder, T. M. Wong, and R. Meservey. Large magnetoresistance at room temperature in ferromagnetic thin film tunnel junctions. *Physical Review Letters*, 74(16):3273–3276, 1995.

[20] T. Miyazaki and N. Tezuka. Giant magnetic tunneling effect in $Fe/Al_2O_3/Fe$ junction. *Journal of Magnetism and Magnetic Materials*, 139:L231–L234, 1995.

[21] D. Wang, C. Nordman, J. M. Daughton, Z. Qian, and J. Fink. 70% TMR at room temperature for SDT sandwich junctions with CoFeB as free and reference layers. *IEEE Transactions on Magnetics*, 40(4):2269–2271, 2004.

[22] S. Yuasa, T. Nagahama, A. Fukushima, Y. Suzuki, and K. Ando. Giant room-temperature magnetoresistance in single-crystal Fe/MgO/Fe magnetic tunnel junctions. *Nature Materials*, 3:868–871, 2004.

[23] S. S. P. Parkin, C. Kaiser, A. Panchula, P. M. Rice, B. Hughes, M. Samant, and S.-H. Yang. Giant tunnelling magnetoresistance at room temperature with MgO (100) tunnel barriers. *Nature Materials*, 3:862–867, 2004.

[24] W. H. Butler, X.-G. Zhang, T. C. Schulthess, and J. M. MacLaren. Spin-dependent tunneling conductance of Fe/MgO/Fe sandwiches. *Physical Review B*, 63:054416, 2001.

[25] J. Mathon and A. Umerski. Theory of tunneling magnetoresistance of an epitaxial Fe/MgO/Fe(001) junction. *Physical Review B*, 63:220403(R), 2001.

[26] T. Nagahama and J. S. Moodera. Magnetic tunnel junctions with magnesium oxide barriers. *Journal of Magnetics*, 11(4):170–181, 2006.

[27] J. Hayakawa, S. Ikeda, Y. M. Lee, F. Matsukura, and H. Ohno. Effect of high annealing temperature on giant tunnel magnetoresistance ratio of CoFeB/MgO/CoFeB magnetic tunnel junctions. *Applied Physics Letters*, 89:232510, 2006.

[28] J. S. Moodera, M. E. Taylor, and R. Meservey. Exchange-induced spin polarization of conduction electrons in paramagnetic metals. *Physical Review B*, 40(17):11980, 1989.

[29] P. LeClair, H. J. M. Swagten, J. T. Kohlhepp, and W. J. M. de Jonge. Tunnel conductance as a probe of spin polarization decay in Cu dusted $Co/Al_2O_3/Co$ tunnel junctions. *Applied Physics Letters*, 76(25):3783–3785, 2000.

[30] P. LeClair, J. T. Kohlhepp, H. J. M. Swagten, and W. J. M. de Jonge. Interfacial density of states in magnetic tunnel junctions. *Physical Review Letters*, 86(6):1066–1069, 2001.

[31] R. Jansen and J. S. Moodera. Magnetoresistance in doped magnetic tunnel junctions: Effect of spin scattering and impurity-assisted transport. *Physical Review B*, 61(13):99047–9050, 2000.

[32] R. Meservey, P. M. Tedrow, and J. S. Brooks. Tunneling characteristics of amorphous Si barriers. *Journal of Applied Physics*, 53(3):1563–1570, 1982.

[33] G. A. Gibson and R. Meservey. Properties of amorphous germanium tunnel barriers. *Journal of Applied Physics*, 58(4):1584–1596, 1985.

[34] L. Esaki, P. J. Stiles, and S. von Molnar. Magnetointernal field emission in junctions of magnetic insulators. *Physical Review Letters*, 19:852–854, 1967.

[35] W. A. Thompson, W. A. Holtzberg, T. R. McGuire, and G. Petrich. Tunneling study of EuS magnetization. In Jr. C. D. Graham and J. J. Rhyne, editors, *Proc. of the 17th Annual Conf. on Magnetic and Magnetic Materials*, number 5 in AIP Conf. Proc., pages 827–836, Chicago, 1971. AIP.

[36] J. S. Moodera, T. S. Santos, and T. Nagahama. The phenomena of spin filter tunneling: a review. *Journal of Physics: Condensed Matter*, 19:165202, 2007.

[37] N. Müller, W. Eckstein, W. Heiland, and W. Zinn. Electron spin polarization in field emission for EuS-coated tungsten tips. *Physical Review Letters*, 29:1651–1654, 1972.

[38] E. Kisker, G. Baum, A. H. Mahan, W. Raith, and K. Schröder. Conduction-band tunneling and electron-spin polarization in field emission from magnetically ordered europium sulfide on tungsten. *Physical Review Letters*, 36:982–985, 1976.

[39] G. Baum, E. Kisker, A. H. Mahan, W. Raith, and B. Reihl. Field emission of monoenergetic spin-polarized electrons. *Applied Physics*, 14:149–153, 1977.

[40] E. Kisker, G. Baum, A. H. Mahan, W. Raith, and B. Reihl. Electron field emission from ferromagnetic europium sulfide on tungsten. *Physical Review B*, 18:2256–2275, 1978.

[41] J.S. Moodera, X. Hao, G.A. Gibson, and R. Meservey. Electron-spin polarization in tunnel junctions in zero applied field with ferromagnetic EuS barriers. *Physical Review Letters*, 61(5):637–640, 1988.

[42] X. Hao, J.S. Moodera, and R. Meservey. Spin-filter effect of ferromagnetic europium sulfide tunnel barriers. *Physical Review B*, 42(13):8235–8243, 1990.

[43] J.S. Moodera, R. Meservey, and X. Hao. Variation of the electron-spin polarization in EuSe tunnel junctions from zero to near 100% in a magnetic field. *Physical Review Letters*, 70(6):853–856, 1993.

[44] P. Wachter. Europium chalcogenides: EuO, EuS, EuSe, and EuTe. In K.A. Schneider and L. Eyring, editors, *Handbook on the Physics and Chemistry of Rare Earths*, volume 2, pages 507–574. North-Holland Publishing Co., New York, 1979.

[45] M. Gajek, M. Bibes, A. Barthélémy, K. Bouzehouane, S. Fusil, M. Varela, J. Fontcuberta, and A. Fert. Spin filtering through ferromagnetic $BiMnO_3$. *Physical Review B*, 72:020406(R), 2005.

[46] U. Lüders, M. Bibes, K. Bouzehouane, E. Jacquet, J. P. Contour, S. Fusil, J. F. Bobo, J. Fontcuberta, A. Barthélémy, and A. Fert. Spin filtering through ferrimagnetic $NiFe_2O_4$ tunnel barriers. *Applied Physics Letters*, 88:082505, 2006.

[47] M. G. Chapline and S. X. Wang. Room-temperature spin filtering in a $CoFe_2O_4/MgAl_2O_4/Fe_3O_4$ magnetic tunnel barrier. *Physical Review B*, 74:014418, 2006.

[48] A. Ramos, J. B. Moussy, and M. Gautier-Soyer. *unpublished.*

[49] T. S. Santos and J. S. Moodera. Observation of spin filtering with a ferromagnetic EuO tunnel barrier. *Physical Review B*, 69:241203(R), 2004.

[50] C. Haas. Magnetic semiconductors. *C.R.C. Critical Reviews in Solid State Sciences*, 1:47–98, 1970.

[51] F. Holtzberg, S. von Molnar, and J. M. D. Coey. Rare earth magnetic semiconductors. In S. P. Keller, editor, *Handbook on Semiconductors*, volume 3, pages 803–856. North-Holland Publishing Co., New York, 1980.

[52] A. Mauger and C. Godart. The magnetic, optical, and transport properties of representatives of a class of magnetic semiconductors: the europium chalcogenides. *Physics Reports*, 141:51–176, 1986.

[53] M. R. Oliver, J. A. Kafalas, J. O. Dimmock, and T. B. Reed. Pressure dependence of the electrical resistivity of EuO. *Physical Review Letters*, 24:1064–1067, 1970.

[54] M. R. Oliver, J. O. Dimmock, A. L. McWhorter, and T. B. Reed. Conductivity studies in europium oxide. *Physical Review B*, 5(3):1078–1098, 1972.

[55] Michael Ray Oliver. *Conductivity studies in europium oxide.* ScD dissertation, MIT, Department of Electrical Engineering, 1970.

[56] G. Petrich, S. von Molnár, and T. Penney. Exchange-induced autoionization in Eu-rich EuO. *Physical Review Letters*, 26(15):885–887, 1971. reference for 13 orders of magnitude conductivity drop.

[57] M. W. Shafer and T. R. McGuire. Studies of Curie-point increases in EuO. *Journal of Applied Physics*, 39(2):588–590, 1968.

[58] S. Von Molnar and M. W. Shafer. Transport in Gd-Doped EuO. *Journal of Applied Physics*, 41(3):1093–1094, 1970.

[59] T. Matsumoto, K. Yamaguchi, K. Yamada, and K. Kawaguchi. Preparation and magnetic properties of Gd doped EuO thin films. *Materials Science Forum*, 373-376:369–372, 2001.

[60] H. Ott, S. J. Heise, R. Sutarto, Z. Hu, C. F. Chang, H. H. Hsieh, H.-J. Lin, C. T. Chen, and L. H. Tjeng. Soft x-ray magnetic circular dichroism study on gd-doped euo thin films. *Physical Review B*, 73:094407, 2006.

[61] T. Kasuya and A. Yanase. Anomalous transport phenomena in Eu-chalcogenide alloys. *Reviews of Modern Physics*, 40(4):684, 1968.

[62] J. Schoenes and P. Wachter. Exchange optics in Gd-doped EuO. *Physical Review B*, 9(7):3097–3105, 1974.

[63] P. G. Steeneken, L. H. Tjeng, I. Elfimov, G. A. Sawatzky, G. Ghiringhelli, N. B. Brookes, and D. J. Huang. Exchange splitting and charge carrier spin polarization in EuO. *Physical Review Letters*, 88(4):047201, 2002.

[64] Peter G. Steeneken. *New light on EuO thin films: Preparation, transport, magnetism and spectroscopy of a ferromagnetic semiconductor.* PhD dissertation, University of Groningen, the Netherlands, Solid State Physics Laboratory, October 2002.

[65] J. Lettieri, V. Vaithyanathan, S. K. Eah, J. Stephens, V. Sih, D. D. Awschalom, J. Levy, and D. G. Schlom. Epitaxial growth and magnetic properties of EuO on (001) Si by molecular-beam epitaxy. *Applied Physics Letters*, 83(5):975–977, 2003.

[66] G. Busch, P. Junod, and P. Wachter. Optical absorption of ferro- and anitferromagnetic europium chalcogenides. *Physics Letters*, 12(1):11–12, 1964.

[67] G. Güntherodt, J. Schoenes, and P. Wachter. Optical constants of the Eu chalcogenides above and below the magnetic ordering temperatures. *Journal of Applied Physics*, 41(3):1083–1084, 1970.

[68] *private communication.*

[69] Robert C. O'Handley. *Modern Magnetic Materials: Principles and Applications.* John Wiley & Sons, Inc., New York, 2000.

[70] É. T. Kulatov ad Y. A. Uspenskiĭ and S. V. Khalilov. Electronic structure and magnetooptical properties of europium monochalcogenides EuO and EuS. *Phys. Solid State*, 38:1677, 1996.

[71] M. Horne, P. Strange, W. M. Temmerman, Z. Szotek, A. Svane, and H. Winter. The electronic structure of europium chalcogenides and pnictides. *Journal of Physics: Condensed Matter*, 16:5061–5070, 2004.

[72] D. B. Ghosh, M. De, and S. K. De. Electronic structure and magneto-optical properties of magnetic semiconductors: europium monochalcogenides. *Physical Review B*, 70:115211, 2004.

[73] Ichiro Tsubokawa. On the magnetic properties of a $CrBr_3$ single crystal. *Journal of the Physical Society of Japan*, 15(9):1664–1668, 1960.

[74] B. T. Matthias, R. M. Bozorth, and J. H. Van Vleck. Ferromagnetic interaction in EuO. *Physical Review Letters*, 7(5):160–161, 1961.

[75] T. Kasuya. Exchange mechanisms in europium chalcogenides. *IBM Journal of Research and Development*, pages 214–223, 1970.

[76] John B. Goodenough. *Magnetism and the Chemical Bond*, volume 1 of *Interscience Monographs on Chemistry*. John Wiley & Sons, Inc., New York-London, 1963.

[77] R. Schiller and W. Nolting. Prediction of a surface state and a related surface insulator-metal transition for the (100) surface of stochiometric EuO. *Physical Review Letters*, 86:3847–3850, 2001.

[78] R. Schiller, W. Müller, and W. Nolting. Kondo lattice model: Application to the temperature-dependent electronic structure of EuO(100) films. *Physical Review B*, 64:134409, 2001.

[79] In G. V. Samsonov, editor, *The Oxide Handbook*. IFI/Plenum, New York, second edition, 1982.

[80] Bernard D. Cullity. *Elements of X-ray Diffraction*. Prentice Hall, Upper Saddle River, NJ, 3rd edition, 2001.

[81] Ezana Negusse. *Interface Magnetism and Spin Dependent Tunneling in EuO and MgO Barriers*. PhD dissertation, Montana State University, Physics Department, June 2007.

[82] B. T. Thole, G. van der Laan, J. C. Fuggle, G. A. Sawatzky, R. C. Karnatak, and J. M. Esteva. $3d$ x-ray-absorption lines and the $3d^9 4f^{n+1}$ multiplets of the lanthanides. *Physical Review B*, 32(8):5107, 1985.

[83] J. Stöhr and R. Nakajima. Magnetic properties of transition-metal multilayers studied with x-ray magnetic circular dichroism spectroscopy. *IBM Journal of Research Development*, 42(1):73–88, 1998.

[84] J. W. Freeland, V. Chakarian, K. Bussmann, Y. U. Idzerda, H. Wende, and C.-C. Kao. Exploring magnetic roughness in CeFe thin films. *Journal of Applied Physics*, 83(11):6290–6292, 1998.

[85] J. Stöhr. In D. C. Koningsberger and R. Prins, editors, *X-ray Absorption: Principles, Applications, Techniques of EXAFS, SEXAFS and XANES*, page 443. Wiley, New York, 1988.

[86] R. Meservey, P. M. Tedrow, and P. Fulde. Magnetic field splitting of the quasiparticle states in superconducting aluminum films. *Physical Review Letters*, 25(18):1270–1272, 1970.

[87] David Jiles. *Introduction to Magnetism and Magnetic Materials.* Chapman & Hall, London, 1st edition, 1991.

[88] R. Nakajima, J. Stöhr, and Y. U. Idzerda. Electron-yield saturation effects in l-edge x-ray magnetic circular dichroism spectra of Fe, Co, and Ni. *Physical Review B*, 59(9):6421–6429, 1999.

[89] C. T. Chen, Y. U. Idzerda, H.-J. Lin, N. V. Smith, G. Meigs, E. Chaban, G. H. Ho, E. Pellegrin, and F. Sette. Experimental confirmation of the x-ray magnetic circular dichroism sum rules for iron and cobalt. *Physical Review Letters*, 75(1):152–155, 1995.

[90] P. M. Tedrow, J. E. Tkaczyk, and A. Kumar. Spin-polarized tunneling study of an artificially layered superconductor with internal magnetic field: EuO-Al. *Physical Review Letters*, 56(16):1746–1749, 1986.

[91] X. Hao, J. S. Moodera, and R. Meservey. Thin-film superconductor in an exchange field. *Physical Review Letters*, 67(10):1342–1345, 1991.

[92] G. Sarma. On the influence of a uniform exchange field acting on the spins of the conduction electrons in a superconductor. *J. Phys. Chem. Solids*, 24:1029–1032, 1963.

[93] P. G. de Gennes. Coupling between ferromagnets through a superconducting layer. *Physics Letters*, 23(1):10–11, 1966.

[94] C. W. Miller, Z.-P. Li, I. K. Schuller, R. W. Dave, J. M. Slaughter, and J. Åkerman. Origin of the breakdown of Wentzel-Kramers-Brillouin-based tunneling models. *Physical Review B*, 74:212404, 2006.

[95] R. H. Fowler and L. Nordheim. Electron emission in intense electric fields. In *Proc. of the Royal Society of London, Containing Papers of a Mathematical and Physical Character, Vol 119*, number 781 in A, pages 173–181. The Royal Society, May 1928.

[96] T. Nagahama, T. S. Santos, and J. S. Moodera. Enhanced magneto-transport at high bias in quasi-magnetic tunnel junctions with eus spin-filter barriers. Physical Review Letters, *in press.*

[97] Alireza Saffarzadeh. Spin-filter magnetoresistance in magnetic barrier junctions. *Journal of Magnetism and Magnetic Materials*, 269:327–332, 2004.

[98] M. G. Chapline and S. X. Wang. Spin filter based tunnel junctions. *Journal of Applied Physics*, 100:123909, 2006.

[99] B.-C. Min, K. Motohashi, C. Lodder, and R. Jansen. Tunable spin-tunnel contacts to silicon using low-work-function ferromagnets. *Nature Materials*, 5:817–822, 2006.

[100] P. LeClair, J. K. Ha, H. J. M. Swagten, J. T. Kohlhepp, C. H. van de Vin, and W. J. M. de Jonge. Large magnetoresistance using hybrid spin filter devices. *Applied Physics Letters*, 80(4):625–627, 2002.

[101] Coen J. P. Smits. *EuS based thin film layered systems: magnetoresistance and coupling phenomena.* PhD dissertation, Eindhoven University of Technology, Dept. of Applied Physics, August 2006.

[102] R. M. Moon and W. C. Koehler. Magnetic properties of Gd_2O_3. *Physical Review B*, 11(4):1609–1622, 1975.

[103] J. Nogués and Ivan K. Schuller. Exchange bias. *Journal of Magnetism and Magnetic Materials*, 192:203–232, 1999.

[104] J. M. De Teresa, A. Barthèlèmy, A. Fert, J. P. Contour, R. Lyonnet, F. Montaigne, P. Seneor, and A. Vaurès. Inverse tunnel magnetoresistance in $Co/SrTiO_3/La_{0.7}Sr_{0.3}MnO_3$: new ideas on spin-polarized tunneling. *Physical Review Letters*, 82(21):4288–4291, 1999.

[105] M. Bibes, M. Bowen, A. Barthèlèmy, A. Anane, K. Bouzehouane, C. Carrétéro, E. Jacquet, and J.-P. Contour. Growth and characterization of TiO_2 as a barrier for spin-polarized tunneling. *Applied Physics Letters*, 82(19):3269–3271, 2003.

[106] A. Thomas, J. S. Moodera, and B. Satpati. Evidence for positive spin polarization in Co with $SrTiO_3$ barriers. *Journal of Applied Physics*, 97(10):10C908, 2005.

[107] M. B. Stearns. Simple explanation of tunneling spin-polarization of Fe, Co, Ni and its alloys. *Journal of Magnetism and Magnetic Materials*, 5(2):167–171, 1977.

[108] M. Münzenberg and J. S. Moodera. Superconductor-ferromagnet tunneling measurements indicate *sp*-spin and *d*-spin currents. *Physical Review B*, 70(6):060402(R), 2004.

[109] E. Yu. Tsymbal and D. G. Pettifor. Modelling of spin-polarized electron tunnelling from 3*d* ferromagnets. *Journal of Physics: Condensed Matter*, 9:L411–L417, 1997.

[110] I. I. Oleinik, E. Yu. Tsymbal, and D. G. Pettifor. Structural and electronic properties of $Co/Al_2O_3/Co$ magnetic tunnel junction from first principles. *Physical Review B*, 62(6):3952–3959, 2000.

[111] E. Y. Tsymbal and K. D. Belashchenko. Role of interface bonding in spin-dependent tunneling. *Journal of Applied Physics*, 97:10C910, 2005.

[112] S. Zhang, P. M. Levy, A. C. Marley, and S. S. P. Parkin. Quenching of magnetoresistance by hot electrons in magnetic tunnel junctions. *Physical Review Letters*, 79(19):3744–3747, 1997.

[113] A. M. Bratkovsky. Tunneling of electrons in conventional and half-metallic systems: towards very large magnetoresistance. *Physical Review B*, 56(5):2344–2347, 1997.

[114] J. S. Moodera, J. Nowak, and R. J. M van de Veerdonk. Interface magnetism and spin wave scattering in ferromagnet-insulator-ferromagnet tunnel junctions. *Physical Review Letters*, 80(13):2941–2944, 1998.

[115] S. Sugahara and M. Tanaka. A novel spin transistor based on spin-filtering in ferromagnetic barriers: a spin-filter transistor. *Physica E*, 21:996–1001, 2004.

[116] F. J. Jedema, H. B. Heersche, A. T. Filip, J. J. A. Baselmans, and B. J. van Wees. Electrical detection of spin precession in a metallic mesoscopic spin valve. *Nature*, 416:713–716, 2002.

[117] S. O. Valenzuela and M. Tinkham. Direct electronic measurement of the spin hall effect. *Nature*, 442:176–179, 2006.

[118] X. Lou, C. Adelmann, S. A. Crooker, E. S. Garlid, J. Zhang, K. S. M. Reddy, S. D. Flexner, C. J. Palmstrom, and P. A. Crowell. Electrical detection of spin transport in lateral ferromagnet-semiconductor devices. *Nature Physics*, 3:197–202, 2007.

[119] S. Datta and B. Das. Electronic analog of the electro-optic modulator. *Applied Physics Letters*, 56(7):665–667, 1990.

[120] I. Appelbaum, B. Huang, and D. Monsma. Electronic measurement and control of spin transport in silicon. *unpublished.*

[121] L. S. Hung and C. H. Chen. Recent progress of molecular organic electroluminescent materials and devices. *Materials Science and Engineering R*, 39:143–222, 2002.

[122] Z. H. Xiong, Di Wu, Z. V. Vardeny, and J. Shi. Giant magnetoresistance in organic spin-valves. *Nature (London)*, 427:821–824, 2004.

[123] Ö. Mermer, G. Verraraghavan, T. L. Francis, and M. Wohlgenannt. Large magnetoresistance in nonmagnetic π-conjugated semiconductor thin film devices. *Physical Review B*, 72(20):205202, 2005.

[124] M. Cölle and W. Brütting. Thermal, structural and photophysical properties of the organic semiconductor alq_3. *Phys. Stat. Sol. (a)*, 201(6):1095–1115, 2004.

[125] C. W. Tang and S. A. VanSlyke. Organic electroluminescent diodes. *Applied Physics Letters*, 51(12):913–915, 1987.

[126] C. H. M. Marée, R. A. Weller, L. C. Feldman, K. Pakbaz, and H. W. H. Lee. Accurate thickness/density measurements of organic light-emitting diodes. *Journal of Applied Physics*, 84(7):4013–4016, 1998.

[127] T. Gavrilko, R. Fedorovich, G. Dovbeshko, A. Marchenko, A. Naumovets, V. Nechytaylo, G. Puchkovska, L. Viduta, J. Baran, and H. Ratajczak. FTIR spectroscopic and STM studies of vacuum deposited aluminum (III) 8-hydroxyquinoline thin films. *Journal of Molecular Structure*, 704:163–168, 2004.

[128] X. M. Ding, L. M. Hung, C. S. Lee, and S. T. Lee. Vibrational structure of ultrathin 8-hydroxyquinoline aluminum films studied by high-resolution electron-energy-loss spectroscopy. *Physical Review B*, 60(19):13291–13293, 1999.

[129] K. L. Wang, B. Lai, M. Lu, X. Zhou, L. S. Liao, X. M. Ding, X. Y. Hou, and S. T. Lee. Electronic structure and energy level alignment of $Alq_3/Al_2O_3/Al$ and Alq_3/Al interfaces studied by ultraviolet photoemission spectroscopy. *Thin Solid Films*, 363:178–181, 2000.

[130] C. Shen, A. Kahn, and J. Schwartz. Chemical and electrical properties of interfaces between magnesium and aluminum and *tris*-(8-hydroxy quinoline) aluminum. *Journal of Applied Physics*, 89(1):449–459, 2001.

[131] A. N. Caruso, D. L. Schulz, and P. A. Dowben. Metal hybridization and electronic structure of Tris(8-hydroxyquinolato)aluminum (Alq_3). *Chemical Physics Letters*, 413:321–325, 2005.

[132] J. G. Simmons. Generalized formula for the electric tunnel effect between similar electrodes separated by a thin insulating film. *Journal of Applied Physics*, 34(6):1793–1803, 1963.

[133] Paul K. Hansma, editor. *Tunnel Spectroscopy: Capabilities, Applications, and New Techniques.* Plenum Press: New York, 1982.

[134] J. Appelbaum. $s-d$ exchange model of zero-bias tunneling anomalies. *Physical Review Letters*, 17(2):91–95, 1966.

[135] E. L. Wolf. *Principles of Electron Tunneling Spectroscopy.* Oxford University Press: Oxford, England, 1985.

[136] B. Oliver and J. Nowak. Temperature and bias dependence of dynamic conductance-low resistive magnetic tunnel junctions. *Journal of Applied Physics*, 95(2):546–550, 2004.

[137] K. Maki. Pauli paramagnetism and superconducting state. II. *Progress of Theoretical Physics*, 32(1):29–36, 1964.

[138] Peter M. Levy and Ingrid Mertig. Theory of giant magnetoresistance. In Sadamichi Maekawa and Teruya Shinjo, editors, *Spin Dependent Transport in Magnetic Nanostructures*, Advances in Condensed Matter Science, chapter 2, pages 47–111. Taylor & Francis, London, 2002.

[139] C. Vouille, A. Barthélémy, F. Elokan Mpondo, A. Fert, P. A. Schroeder, S. Y. Hsu, A. Reilly, and R. Loloee. Microscopic mechanisms of giant magnetoresistance. *Physical Review B*, 60(9):6710–6722, 1999.

[140] D. G. Walmsley, R. B. Floyd, and W. E. Timms. Conductance of clean and doped tunnel junctions. *Solid State Communications*, 22:497–499, 1977.

[141] S. T. Lee, X. Y. Hou, M. G. Mason, and C. W. Tang. Energy level alignment at Alq/metal interfaces. *Applied Physics Letters*, 72(13):1593–1595, 1998.

[142] I. G. Hill, A. Rajagopal, A. Kahn, and Y. Hu. Molecular level alignment at organic semiconductor-metal interfaces. *Applied Physics Letters*, 73(5):662–664, 1998.

[143] F. Li, H. Tang, J. Anderegg, and J. Shinar. Fabrication and electroluminescence of double-layered organic light-emitting diodes with the Al_2O_3/Al cathode. *Applied Physics Letters*, 70(10):1233–1235, 1997.

Publications and Presentations

Publications in Refereed Journals

T. Nagahama, T. S. Santos and J. S. Moodera. Enhanced magneto-transport at high bias in quasi-magnetic tunnel junctions with EuS spin-filter barriers, *Physical Review Letters, in press*

G. X. Miao, K. S. Yoon, T. S. Santos, and J. S. Moodera. Influence of spin-polarized current on superconductivity and the realization of large magnetoresistance, submitted to *Physical Review Letters, in press*

J. S. Moodera, T. S. Santos, and T. Nagahama. The phenomena of spin filter tunnelling, *Journal of Physics: Condensed Matter* 19, 165202 (2007).

T. S. Santos, J. S. Lee, P. Migdal, I. Chaitanya, B. Satpati and J. S. Moodera. Room temperature tunnel magnetoresistance and spin-polarized tunneling studies with organic semiconductor barrier, *Physical Review Letters* 98, 016601 (2007).

R. Guerrero, F. G. Aliev, Y. Tserkovnyak, T. Santos and J. S. Moodera. Shot noise in magnetic tunnel junctions: Evidence for sequential tunneling, *Physical Review Letters* 97, 266602 (2006).

E. Negusse, J. Holroyd, M. Liberati, J. Dvorak, Y. Idzerda, T. Santos, J. S. Moodera and E. Arenholz. Effect of electrode and EuO thickness on EuO-electrode interface in tunneling spin filter, *Journal of Applied Physics* 99, 08E507 (2006).

J. Philip, A. Punnoose, B. I. Kim, K. M. Reddy, S. Layne, J. O. Holmes, B. Satpati, P. R. Leclair, T. Santos and J. S. Moodera. Carrier-controlled ferromagnetism in transparent oxide semiconductors, *Nature Materials* 5, 298-304, (2006).

S. H. Song, S. H. Lim, M. H. Jung, T. S. Santos, and J. S. Moodera. Magnetic and transport properties of amorphous Ge-Mn thin films, *Journal of the Korean Physical Society* 49(6), 2386-2396 (2006).

T. S. Santos and J. S. Moodera. Observation of spin filtering with a ferromagnetic EuO tunnel barrier, *Physical Review B* 69, 241203(R), (2004).

Conference Presentations

"Exchange Splitting and 100% Spin Polarization in Monolayer Level EuO Thin Films," (oral presentation) T. S. Santos, J. S. Moodera, E. Negusse, and Y. Idzerda. American Physical Society: March Meeting, Denver, CO, March 2007.

"Near 100% Spin Filtering with EuO Tunnel Barriers," (poster) T. S. Santos and J. S. Moodera. Joint Magnetism and Magnetic Materials/Intermag Conference, Baltimore, MD, January 2007.

"Europium Oxide as a Spin Filtering Tunnel Barrier," (poster) T. S. Santos and J. S. Moodera. Gordon Research Conference on Magnetic Nanostructures, Oxford, England, September 2006.

"Room Temperature TMR and Spin-Polarized Tunneling Studies with Organic Semiconductor Barrier," (oral presentation) T. S. Santos, J. S. Lee, P. Migdal, I. C. Lekshmi, B. Satpati and J. S. Moodera. American Physical Society: March Meeting, Baltimore, MD, March 2006.

"Correlation of Interface Property and Spin-Filter Phenomena in Ultra-thin EuO Film," (oral presentation) T. S. Santos, J. S. Moodera, E. Negusse and Y. Idzerda. Magnetism and Magnetic Materials Conference, San Jose, CA, November 2005.

"Europium Monoxide as a Spin-Filtering Tunnel Barrier," (poster) T. S. Santos and J. S. Moodera. Workshop on Nanomagnetism and Spintronics, Cargèse, Corsica, France, May 2005.

"EuO as a Spin-Filter Material for Spin-Injection," (oral presentation) T. S. Santos and J. S. Moodera. American Physical Society: March Meeting, Montreal, Canada, March 2004.

"Tunneling Characteristics of Magnetic Tunnel Junctions with Boron Barrier," (poster) T. S. Santos and J. S. Moodera. International Conference on Magnetism, Rome, Italy, July 2003.

"Spin-Filter Effect of Europium Chalcogenide Tunnel Barriers," (poster) T. S. Santos and J. S. Moodera. Gordon Research Conference on Magnetic Nanostructures, Barga, Italy, May 2002.

"Europium Chalcogenides as a Spin Filter Material for Efficient Spin Injection into Semiconductors," (oral presentation) T. S. Santos, T. Martin, T. Matsumoto and J. S. Moodera. Magnetism and Magnetic Materials Conference, Seattle, WA, November 2001.

Biographical Note

Education

2002-2007 Ph.D. in Materials Science and Engineering
Massachusetts Institute of Technology, Cambridge, MA
Thesis: *Europium Oxide as a Perfect Electron Spin Filter*
Advisor: Dr. Jagadeesh S. Moodera, Francis Bitter Magnet Laboratory

1998-2002 S.B. in Materials Science and Engineering
Massachusetts Institute of Technology, Cambridge, MA

1994-1998 Valdosta High School, Valdosta, GA, Salutatorian

Awards and Honors

National Science Foundation Graduate Research Fellowship, 2002-2006
Outstanding Senior Thesis, Department of Materials Science and Engineering, MIT, 2002
Association of MIT Alumnae Senior Academic Award, Honorable Mention, 2002
Undergraduate Materials Research Initiative Award, Materials Research Society, 2001